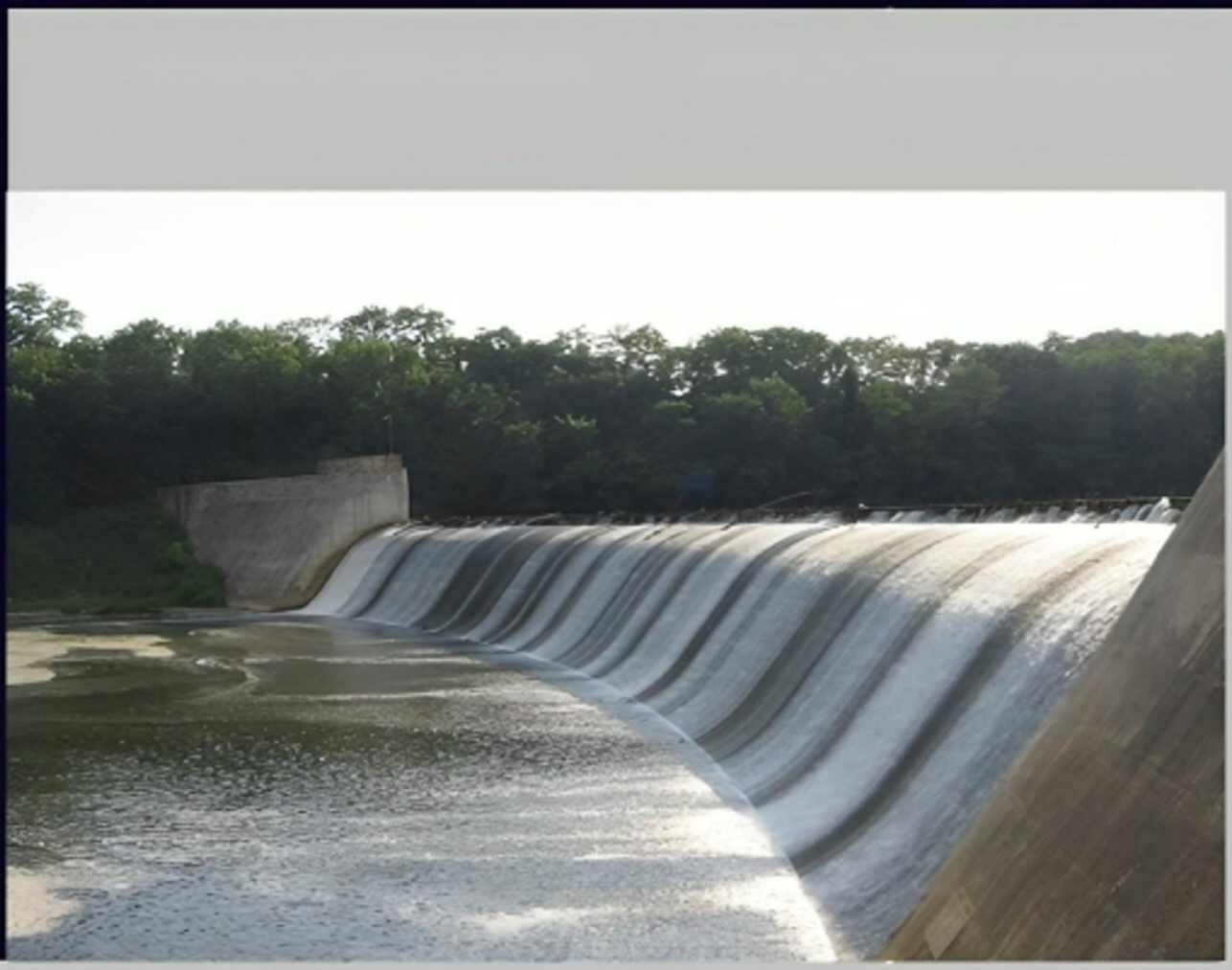
Iranian Hydraulic Association

Shahid Chamran University of Ahvaz

Journal of Hydraulic Structures

Scientific Professional Journal



July 2024
Volume 10, Issue 3

ISSN (Online): 2345-4156
https://jhs.scu.ac.ir/

Aims and Scope

Journal of Hydraulic Structures is an interdisciplinary journal which publishes high-quality peer-reviewed articles addressing the latest developments and applied methods in analysis and design, construction, maintenance, management, and operation policy of Hydraulic Structures.

The Journal aims at providing an efficient route to fast-track publication, within 10-12 weeks after manuscript submission.

The general areas covered by the Journal include:

- Advances in numerical and analytical methods applicable to hydraulic structures
- Hydro informatics and soft computing
- Hydraulic aspects of hydraulic structures
- Applied surface and subsurface hydrology and hydrometeorology
- Forecasting approaches in water resources engineering
- Economic and social aspects of hydraulic structures
- Uncertainty analysis and risk management in hydraulics and water resources engineering
- Application of Nanotechnology in hydraulic structures
- Geotechnics of hydraulic structures
- Damage detection techniques
- Technical and methodological advances in application, design/selection, production, construction materials of hydraulic structures.
- Application of Artificial Intelligence techniques in all aspects of hydraulic structures.

General Information:

Title: Journal of Hydraulic Structures

Publisher: Shahid Chamran University of Ahvaz

ISSN (Print): 2345-413X

ISSN (Online): 2345-4156

Website: https://jhs.scu.ac.ir/

Address: Faculty of Civil Engineering and Architecture, Shahid Chamran University of Ahvaz, Ahvaz, Iran

Email: jhs@scu.ac.ir

Journal of

Hydraulic Structures

Shahid Chamran University of Ahvaz

Director-in-Charge: Prof. Ali Haghighi

Editor-in-Chief: Prof. Hamid R. Ghafouri

Managing Editor: Dr. Amir H. Shafiee

Contents:

01

Investigating the effect of buried walls through rockfill detention structures on the longitudinal water surface profile

Jafar Chabokpour; Omar Minaei

18

Experimental study of contaminant mixing through the buried river junctions

Jafar Chabokpour

34

Feasibility study of fuzzy method in slope stability analysis of earth dams with respect to the uncertainty of geotechnical parameters

Amin Falamaki; Amir Hossein Shafiee; Mahdiye Esfandiyari

51

Application of machine learning methods on investigation the effect of interrupted deflector's height and downstream depth changes on energy dissipation at flip bucket spillways

Arash Adib; Danial Ebrahimzadeh; Mahmood S. Bejestan; Morteza Lotfirad; Masoud Oulapour

72

Hydraulic performance evaluation of head works using FLOW 3D

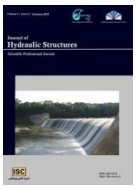
Mukesh Raj Kafle

90

The influence of the submergence ratio of submerged vanes on the slope of the hole around the pier groups in a sharp bend

Neda Safaripour; Mohammad vaghefi; Amin Mahmoudi

Journal of Hydraulic Structures
J. Hydraul. Struct., 2024;10(3):1-17
DOI: 10.22055/jhs.2024.44697.1261



OPEN ACCESS

Investigating the effect of buried walls through rockfill detention structures on the longitudinal water surface profile

Jafar Chabokpour [*1]
Omar Minaei [1]

Abstract

Rockfill structures in river training projects, such as detention dams, gabions, and levees, play a significant role in flood control. One of the common types of these structures is porous flood mitigation dams. This research investigated the surface flow profile by developing an analytical model based on specific energy relationships and Wilkins pore velocity and employing numerical methods based on estimation and correction methods. In order to examine the efficiency of the presented models, experiments were performed both with and without buried inside walls through rockfill media. The results show the accuracy and efficiency of analytical and numerical methods for calculating the water surface profile. The numerical estimation-correction method is used to estimate the passing flow profile through the rockfill media. In order to apply these methods in the experiments including buried curtain, the profile is divided into two parts, and the computations were done by considering two boundary conditions at the outlet and the buried wall position. The flow profile was calculated by the least square curve fitting method, and the c and d coefficients were extracted by taking into account the influencing factors, including the rockfill media diameter, the length of the porous medium, and operated flow rate for a specific diameter. Moreover, the results indicate the appropriate correlation between the laboratory data and analytical and numerical solutions in the experiments, including wall. Quantitatively, the root mean square error (RMSE) ranged from 3 to 5.5 mm, with a relative error between 3 and 9.3%. The relative error increased with higher core heights, particularly downstream of the core due to local flow acceleration and significant flow curvature. At a flow discharge of 0.19 l/s, the relative error was 3%, rising to 8% at higher flow rates. It was also observed that with the increase of the entrance flow discharge, the profile estimation accuracy decreased, and curvature in the water surface profile was observed.

Keywords: Rockfill Dam, Water Surface Profile, Analytical Solution, Numerical Estimation-Correction Method, Vertical and Inclined Curtains.

Received: 02 September 2023; Accepted: 09 April 2024

[*] E-mail: J.chabokpour@maragheh.ac.ir (**Corresponding Author**)
[1] Department of Civil Engineering, University of Maragheh, Maragheh, Iran.

1. Introduction

In large porous media, flow can occur in different ways depending on the characteristics of the medium. In some cases, when the fluid velocity increases or the pore size decreases, the flow behavior can deviate from Darcy flow. This is known as non-Darcy flow and is characterized by inertial, viscous, or turbulent effects, which can result in a non-linear relationship between flow rate and pressure gradient. Understanding and predicting the flow through large porous media is crucial in many fields, including hydrology, geology, environmental science, and petroleum engineering. It helps in determining the movement of contaminants in groundwater, designing efficient drainage systems, optimizing oil and gas recovery, and modeling the transport of pollutants in the subsurface. Rock embankments are used as a crucial part of gravel structures. Unlike the concrete and earth dams built through river reaches, gravel structures have much lower costs compared to them. One of the most important advantages of these structures is their use as flood mitigation structures. These detention structures are usually built in series. By forming small reservoirs through the river, they cause flood storage through the river reaches. The passing flood through large porous media has a high pore velocity and is therefore known as None-Darcy flow. By increasing the flow velocity inside the pore system, the inertial force gradually overcomes the viscous force, and consequently, the turbulent None-Darcy flow occurs [1-3]. Non-Darcy flows can be classified into two categories: parallel flows and radial flows. Parallel flows are commonly observed in scenarios involving gravel dams, gabions, and other similar structures. In these cases, the streamlines are nearly parallel, and the flow can exist in both pressurized and free-surface modes. On the other hand, radial flows are encountered in situations such as wells drilled in coarse-grained alluvial beds. These flows require specialized analysis techniques to understand their behavior and impact on hydraulic structures [4-6].

Buried streams, which are often formed due to mining or roadway operations near rivers, present unique challenges in hydraulic engineering. These streams can alter the flow regime from open channel flow to non-Darcy inner flow, making it essential to accurately predict and simulate the flow patterns. Gradually-varied flow algorithms offer a practical and cost-effective approach to studying the flow in buried streams, providing valuable insights for design and operational considerations [7-9]. The gradually-varied flow theory is a widely used approach in analyzing and simulating flow in non-Darcy porous media. This theory requires less data compared to solving complex equations such as the Parkin equation, making it more practical and cost-effective. By applying the gradually-varied flow theory, researchers have successfully calculated water surface profiles in various scenarios, including radial non-Darcy flow with a free surface [10-13].

In addition to experimental approaches, numerical methods have also been employed to estimate water surface profiles in buried streams. Researchers have utilized techniques such as finite differences, finite elements, and finite volumes to solve the equations governing radial non-Darcy flow. These numerical methods require extensive data and computational resources, but they provide valuable insights into the behavior of flow in porous media [14].

One-dimensional analysis using the gradually-varied flow theory and two-dimensional analysis using the Parkin equation have been extensively used in studying non-Darcy flows. However, the gradually-varied flow theory offers advantages in terms of data requirements and computational complexity. The water surface profile obtained from the gradually-varied flow theory can serve as a crucial boundary condition for solving the Parkin equation, simplifying the overall analysis process [15, 16].

The equations that relate the velocity and hydraulic gradient to each other are in two general forms: quadratic and power. In order to more successfully model the turbulence in the pore system, Forchheimer added a quadratic term to Darcy's Equation to model both turbulent and viscous flow efficiently. In other words, if any of these two mechanisms are powerful, the corresponding coefficients would be more prominent. The equation's general form is according to Eq. 1 [10].

$$i = a.V + b.V^2 \quad (1)$$

In which $i$is hydraulic gradient, $V$is flow velocity and a, $b$are equation parameters.

Eq. 1 has two coefficients, and Eqs. 2 and 3 are presented for its parameters using dimensional analysis for one-dimensional [17, 18].

$$a = \frac{\mu}{\rho g k} \quad (2)$$

$$b = \frac{1}{g\sqrt{ck}} \quad (3)$$

As a result, if Forchheimer's Equation is rewritten using mentioned coefficients, the following relation can be obtained.

$$i = \frac{\mu}{\rho g k}V + \frac{1}{g\sqrt{ck}}V^2 = \frac{\mu}{\rho g}[\frac{1}{k} + \frac{\rho}{\mu\sqrt{ck}}V]V \quad (4)$$

In which μ is the dynamic viscosity, g is the acceleration of gravity, k is the intrinsic permeability, V is the apparent velocity, ρ is the fluid density, and c is the experimental constant coefficient.

In previous studies, it is typical to use the actual pore velocity instead of the average velocity. Therefore, by using it and defining the j function as Eq. 5, Eq. 6 can be extracted.

$$j = \frac{1}{\frac{1}{k} + \frac{\rho V_a}{\mu\sqrt{c'k'}}} \quad (5)$$

$$i = i_t = \frac{\mu}{\rho g j}V_a \quad (6)$$

In Eqs.5 and 6, c' and k' are similar parameters to c and k, and they can be obtained better by applying the actual velocity (V_a) instead of the average velocity (V). However, in the Darcy flow, the equality $j = k$ is valid [19-21].

The next group of equations that relate the hydraulic gradient to the pore flow velocity are power-form equations, and one of the most widely used equations is presented by Wilkins (1956) [20] as Eq. 7.

$$V_V = C\mu^a m^b i^\omega \quad (7)$$

Where: V_V is passing pore velocity, C is an experimental constant that can be determined according to the shape of the particles, μ is the dynamic viscosity of water, and a, b are coefficients that are determined experimentally and using laboratory data.

Wilkins calibrated and validated the general form of Eq. 7 by conducting experiments on coarse-grained materials, and consequently, Eq. 8 is obtained.

$$V_v = Wm^{0.5} i^{0.54}, \qquad i = Cv_v^d \tag{8}$$

$Wm^{0.5}$ is assumed as the hydraulic conductivity of the porous media and the value of 0.54 was estimated as the power of the hydraulic gradient because of turbulent flow conditions [22].

Heydari et al., [23] discussed the longitudinal profile of the non-Darcy flow using the finite element numerical method and presented an equation for the flow rate. Using experimental data and their analysis, Sedeghi Asal et al., [22] indicated that in horizontal and gentle slopes, the passing flow through large porous media follows the gradually varied flow theory. In contrast, in the steep slopes, The gravity force in the flow direction is higher; consequently, uniform flow forms. Salahi et al., [24] based on a laboratory study on different types of crushed and angular rock materials in a wide range of Reynolds numbers, presented values for the power of the Wilkins equation. The results of their research showed that the velocity power in the Wilkins relation fluctuates in the range of 1.6 to 1.8 depending on the grain size characteristics. Asiban et al., [25] calculated the longitudinal profile of the flow using the direct step-by-step method, mostly used in subcritical flows. As a result, the relative error percentage for profile estimation was calculated as 17.6%.

Sarvarian et al., [26] in their study optimized the location and arrangement of rockfill dams in Taleghan basin using both economic and hydraulic criteria. The study employed the "BRM" model (Basin Routing Model, a program developed in Matlab to calculate flow through rockfill dams and estimate the outlet hydrograph of a basin) and the NSGAII method (Non-dominated Sorting Genetic Algorithm II, a multi-objective optimization algorithm used in the study) for optimization. Results showed a 74.4% cost reduction and a 64.9% peak discharge reduction compared to alternative scenarios. Most dams were placed upstream and on the main river to enhance flood control efficiency [26].

Zhang et al., [27] discussed the analytical treatment of non-Darcian flow near a non-uniform flux well face, highlighting limitations in the linearization method for turbulent flow. Their study emphasized no direct analysis of datasets.

Chabakpour and Amiri [3] investigated the application of the GVF flow equation for profile estimation of passing flow through the porous media using direct numerical methods. For this purpose, numerical methods of Euler, modified Euler, and 4th-order Range-Kutta were used, and the results were compared with the experimental data. It was concluded that the Euler method has low accuracy and is unsuitable for flow profile calculation. Also, the 4th-order Range-Kutta method is more accurate than the modified Euler method. Furthermore, the c and d coefficients were considered equal to 22.5 and 2, respectively, indicating a completely turbulent flow.

Considering previous studies, it can be seen that the hydraulic investigations of passing flows through large porous media have been of interest to many previous researchers, and the operated numerical methods have had favorable results. However, due to the nature of gravel dams (for flood mitigation), they differ somewhat from the investigated cases. In order to increase their applicability, concrete or clay, buried curtains are placed inside their body. These walls, whether vertical or inclined, affect the profile of the upstream return flow and practically divide the longitudinal profile into two different parts. For this reason, this research attempted to

investigate the issue in more detail by building a laboratory model, extracting analytical relationships, and using numerical methods. The analysis can also include comparing the performance of detention structures with and without buried walls in term of water surface profiles. Additionally, physical or laboratory experiments can be conducted to investigate the effect of buried walls on the water surface profile. These experiments can involve constructing scaled-down models of the detention structure, including the buried walls, and measuring the resulting water surface profiles under controlled flow conditions. Overall, investigating the effect of buried walls through rockfill detention structures on the longitudinal water surface profile requires a combination of hydraulic modeling, empirical analysis, and physical experiments.

2. Materials and methods

2.1. Laboratory apparatus

The current study used a laboratory flume with a length of 180 cm, width of 20 cm, and height of 70 cm (Fig.1). The flume has a horizontal bed, and different hydraulic gradients were created by flow variation at the porous media entrance. For this purpose, the flow profiles inside the porous medium were determined by operating three entrance discharges of 0.19, 0.26, and 0.37 (l/s). Glass sheets with heights of 10, 20, 30, 40, and 50 cm were used to create an impermeable core. The sheets with a height of 10, 20, and 30 cm were operated as vertical cores at distances of 45, 68, and 90 cm (from the media entrance). On the other hand, the sheets with heights of 40 and 50 cm were operated as inclined cores with slopes of 1:3, 1:2, and 1:1. It should be noted that each of the mentioned cores with heights of 10, 20, and 30 cm (shown with the letters S1, S2, and S3) can be positioned at places of 1, 2, and 3 (which are displayed with the letters P1, P2, and P3). Also, S4 and S5 cores were installed in P4 and P5 positions (Fig. 1). Rockfill materials with an average diameter of 1.8 cm and a uniformity coefficient of 1.4 were used to operate the experiments. In Table 1, the different characteristics of experiments are presented at a flow discharge of 0.26 l/s.

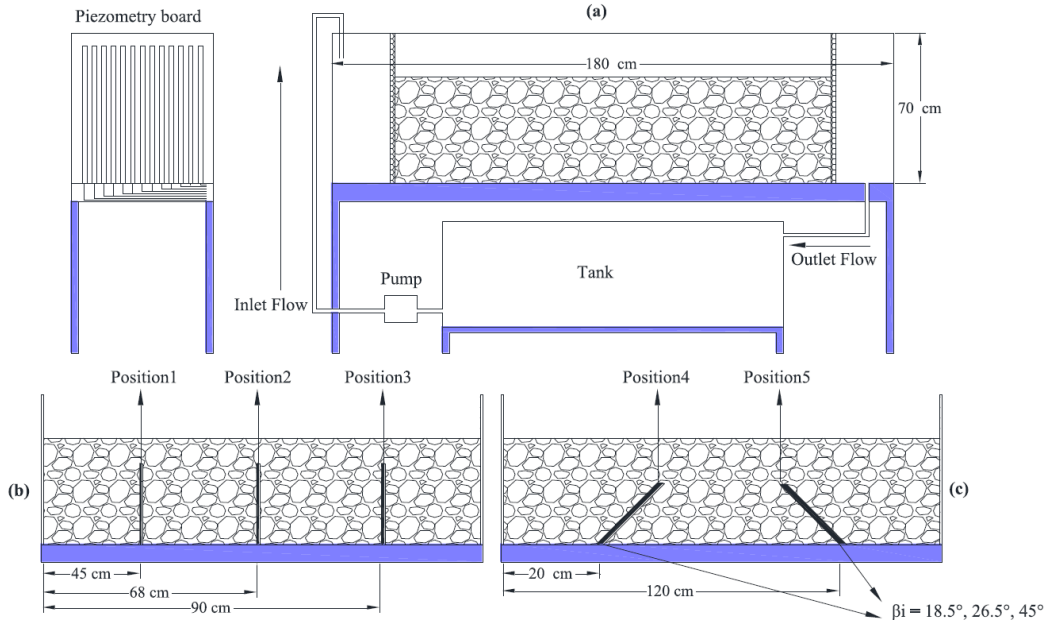


Figure 1. General schematic of the laboratory flume and the placement of glass plates through rockfill media, a) Laboratory flume, b) Position of S1, S2, and S3 as vertical cores, c) Position of S4 and S5 as inclined cores

Table. 1. General characteristics of the conducted experiments at a flow rate of 0.26 l/s

Downstream flow depth (cm)	Upstream flow depth (cm)	Core angle (degree)	Core position	Core height (cm)	Core	Experiment NO.
1	11.9	90	P1	10	S1	1
1.1	12.4	90	P2	10	S1	2
1.4	13.1	90	P3	10	S1	3
1.5	21.7	90	P1	20	S2	4
2.2	22.1	90	P2	20	S2	5
1.1	22	90	P3	20	S2	6
1.8	31.6	90	P1	30	S3	7
1.1	31.4	90	P2	30	S3	8
1.1	31.5	90	P3	30	S3	9
1.8	17.8	18.5	P4	40	S4	10
2	21.4	26.5	P4	40	S4	11
2.2	31.8	45	P4	40	S4	12
3	16.9	18.5	P5	40	S4	13
3.2	21.5	26.5	P5	40	S4	14
2.8	30.9	45	P5	40	S4	15
2.1	20.5	18.5	P4	50	S5	16
2	25.5	26.5	P4	50	S5	17
2.6	38.4	45	P4	50	S5	18
3.2	19.3	18.5	P5	50	S5	19
3	24.6	26.5	P5	50	S5	20
2.8	34.6	45	P5	50	S5	21

2.2. Analytical solution extraction

In large porous media, the flow behavior can vary depending on factors such as the size and connectivity of the pores, the fluid viscosity, and the presence of any obstructions or impurities within the media. Generally, the flow tends to be slower in larger pores with higher permeability, while smaller pores or obstructions can hinder the flow or lead to channeling effects. The gradually varied flow equation in rockfill media is an equation that is used to calculate the variation of water depth and velocity in open channel flow through a rockfill material. It takes into account the hydraulic resistance and roughness characteristics of the rockfill material. This equation is based on the principles of conservation of mass and momentum in open channel flow and is used to analyze and design rockfill channels, such as those found in dams or spillways. It allows engineers to determine the water depth and velocity under different flow conditions, which is important for ensuring proper functioning and stability of the rockfill media. It is possible to use fractional and power equations, especially the Wilkins pore velocity relation. Using power form equations simplifies the integration and is more acceptable in practice. Assuming uniform flow formation, the specific energy equation can be written as Eq. 9 [28].

$$E = y + \frac{V^2}{2g} = y + \frac{q^2}{2gn^2y^2} \tag{9}$$

Where E is the specific energy, y is the flow depth, n is the porous media porosity, and q is the flow rate per unit width. By differentiating both sides of Eq. 9, Eq. 10 can be obtained.

$$\frac{dE}{dx} = \frac{dy}{dx}\left(1 - \frac{q^2}{gn^2y^3}\right) \quad (10)$$

The power form of hydraulic velocity and gradient in non-Darcy flows is also according to Eq. 11, and Eq. 12 is obtained by taking the derivative of specific energy with respect to longitudinal distance.

$$i = a(\frac{q}{ny})^b \quad (11)$$

$$\frac{dE}{dx} = i = a(\frac{q}{ny})^b \quad (12)$$

Also, Eq. 13 can be achieved by integrating Eq. 12.

$$\int_{y1}^{y}\left(y^b - \frac{q^2}{gn^2y^{3-b}}\right)dy = \int_{x1}^{x} a(\frac{q}{n})^b dx \quad (13)$$

Finally, the result of integration can be shown as Eqs. 14 and 15.

$$\frac{y^{1+b}-y_1^{1+b}}{1+b} - \frac{q^2}{gn^2(b-2)}(y^{b-2} - y_1^{b-2}) = a\left(\frac{q}{n}\right)^b (x - x_1) \quad (14)$$

$$\frac{y^{1+b}}{1+b} + \frac{q^2}{gn^2(b-2)}(y^{b-2}) = a\left(\frac{q}{n}\right)^b (x - x_1) + \frac{q^2}{gn^2(b-2)}y_1^{b-2} + \frac{y_1^{1+b}}{1+b} \quad (15)$$

If the values of a, b, n, and q are known, the water surface profile can be calculated using Eq. 15 by applying exit flow depth from the porous media as downstream boundary conditions. Eq. 15 can be operated as the method of calculating distance in terms of depth or depth in terms of distance. For turbulent flow, which is typical to large porous media, by assuming b coefficient equal to 2 in the Wilkins equation, Eq. 15 is rewritten to the simplified form of Eq. 16.

$$\mathrm{y} = \left(y_1^3 + 3a\left(\frac{q}{n}\right)^2 (x - x_1)\right)^{\frac{1}{3}} \quad (16)$$

2.3. Operated Numerical Solution

The gradually varied flow is dominant for passing through large porous media Eq. 17.

$$\frac{dy}{dx} = f(x,y) = \frac{S_0 - S_f}{1 - (\frac{\alpha BQ^2}{gA^3})} = \frac{S_0 - S_f}{1 - Fr^2} \quad (17)$$

Where $\frac{dy}{dx}$ shows the depth variation rate in the flow direction, S_0 is the longitudinal slope, S_f energy line slope, α is the velocity correction factor, Q is the flow discharge, B is the flow width, A is the cross-sectional flow area, and g is the gravity acceleration.

In Eq. 17, due to the horizontality of the channel bed, the value of $S_0$is equal to zero, and the value of $S_f$is equal to the value of the hydraulic gradient (i). Also, the i value was extracted using Eq. 8. Advanced numerical methods are classified into two categories: single-step methods and estimation-correction methods.

The current study used the estimation-correction method to estimate the passing flow profile through the rockfill media. In the estimation-correction methods, an uncertain depth is first estimated using one-step methods and then corrected to reach the desired accuracy. Then, based on the resulting corrected depth, the next depth is estimated and then corrected [29]. In the estimation part, one-step methods can be used. In the present study, Euler's method was used for this stage as Eqs. 18.

$$y_{i+1}^{(0)} = y_i + f(x_i, y_i)\Delta x \tag{18}$$

$$f(x_i, y_i) = \frac{-S_{fi}}{1 - (\frac{B_i \times Q^2}{g \times A_i^3})} = \frac{-S_{fi}}{1 - Fr_i^2} \tag{19}$$

$$\Delta x = x_{i+1} - x_i \tag{20}$$

Using Eq. 18, the first flow depth is estimated. Other parameters of Eq. 18 are also estimated from Eq. 19 and Eq.20. The zero power on the left side of the equation represents the first estimate. Yi is the boundary condition, and laboratory data obtain its value. Considering that the boundary condition of subcritical flows is downstream, yi in the first estimate was considered the exit depth from rockfill media. The first estimate is corrected in the next step according to Eq. 21.

$$\boldsymbol{y_{i+1}^{(1)} = y_i + \frac{1}{2}\left[f(x_i, y_i) + f\left(x_{i+1}, y_{i+1}^{(0)}\right)\right]\Delta x} \tag{21}$$

The depth modification continues such that the jth modification is according to Eq. 22.

$$\boldsymbol{y_{i+1}^{(j)} = y_i + \frac{1}{2}\left[f(x_i, y_i) + f\left(x_{i+1}, y_{i+1}^{(j-1)}\right)\right]\Delta x} \tag{22}$$

The depth correction continues until the calculated depth difference in correction j and j-1 is negligible. The flow depth at point xi+2 is calculated and corrected in the next step according to the above-mentioned method.

2.4. Statistical criteria for validity checking of the employed methods

To compare the experimental and numerical results, statistical methods of root mean square error (RMSE), mean absolute error (MAE), relative error (RE), and coefficient of determination (R^2) were operated according to Eqs. (23-26).

$$RMSE = \sqrt{\frac{\sum_{i=1}^{n}(X - Y)^2}{n}} \tag{23}$$

$$MAE = \frac{1}{n}\sum_{i=1}^{n}|X - Y| \tag{24}$$

$$MAPE = \frac{100}{n}\sum_{i=1}^{n}\left|\frac{X - Y}{X}\right| \tag{25}$$

$$R^2 = \left[\frac{\sum_{i=1}^{n}(X_i - \overline{X}) \cdot (Y_i - \overline{Y})}{\sqrt{\sum_{i=1}^{n}(X_i - \overline{X})^2 \cdot \sum_{i=1}^{n}(Y_i - \overline{Y})^2}} \right]^2 \quad (26)$$

In the above Eqs, n is the data number, X is the laboratory data, Y is the calculated data, $\bar{X}$ is the average of the observed data, and $\bar{Y}$ is the average of the calculated data.

3. Results and discussion

3.1. Flow profile in non-core states

In order to check the flow profiles by the estimation-correction method and estimate the appropriate value for c and d coefficients in Eq.8, first, the flow passing inside porous media without core was investigated. According to the provided range by previous researchers and using the trial and error method, the values of c and d coefficients were considered equal to 22.5 and 1.62, respectively. The experimental and numerical data comparison is shown in Fig. 2 at flow rates of 0.26 and 0.37 l/s, and the error criteria can be seen in each figure.

As shown in Fig. 2, the error values are acceptable, and the calculated results are close to the laboratory data. The RMSE value was calculated between 0.5 and 0.7 cm. Also, the average value of the relative error for all four tests was calculated to be approximately 7.5%. Fig. 3 shows measured depths versus calculated depths by the estimation-correction method.

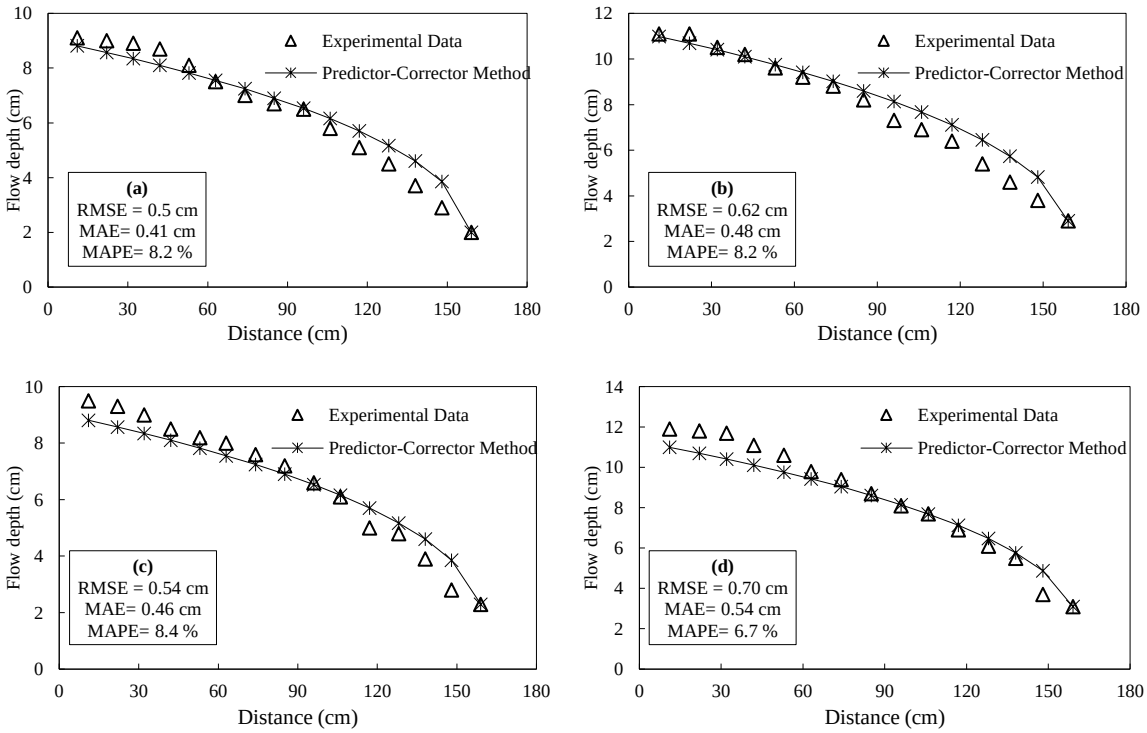


Figure 2. Passing flow profile through the without core rockfill media, a) flow rate 0.26 l/s, d50 = 1.8 cm, b) flow rate 0.37 l/s, d50 = 1.8 cm, c) flow rate 0.26 l/s, d50 = 1.1 cm, d) flow rate 0.37 l/s, d50 = 1.1 cm

The coefficient of determination (R-square), which indicates the correlation between the experimental and numerical data, is equal to 0.98 on average. It can be concluded that the estimation-modification method computes the overall shape of the flow profile very well. From the results of the preliminary tests, it can be concluded that the numerical estimation-modification method is suitable for the flow profile computation. Therefore, it has been used in cases including impermeable cores inside the aggregate medium.

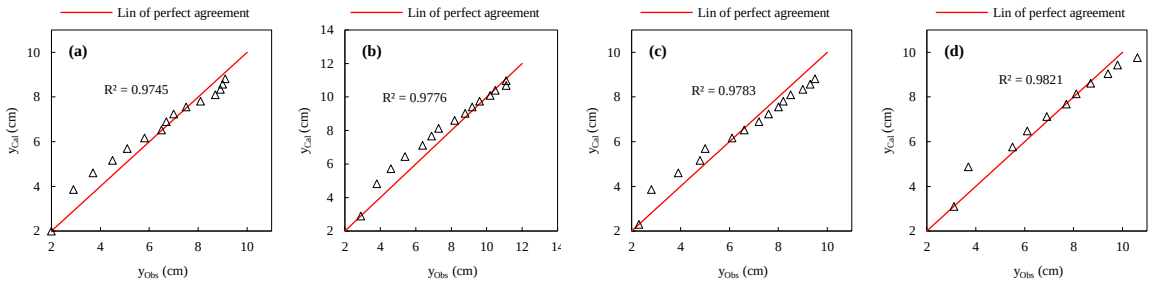


Figure 3. Comparison of observed data and calculation data, a) flow rate 0.26 l/s, d50 = 1.8 cm, b) flow rate 0.37 l/s, d50 = 1.8 cm, c) flow rate 0.26 l/s, d50 = 1.1 cm, d) flow rate 0.37 l/s, d50 = 1.1 cm.

3.2. Flow profile in the presence of an impermeable core

If impermeable cores are inside the rockfill media, the flow profile should be divided into two upstream and downstream parts. In both cases, the gradually varied flow regime is dominant, and only near the core edge, the current overflows from the core, and the curvature of the current is high. Because these two profiles are individual, the boundary conditions should be appropriately considered for each. The boundary condition is adopted in the downstream of each profile. For the downstream profile of the core, the adopted boundary condition is exit flow depth. On the other hand, for the upstream profile, the boundary condition is set to the edge of the core. In the following, the flow profiles in different situations have been calculated.

3.2.1. Flow profile in positions P1, P2 and P3

The cores were installed vertically in positions P1, P2, and P3. S1, S2, and S3 cores were installed separately in each position. In Figs. 4, 5, and 6, flow profiles are shown in positions P1, P2, and P3, respectively.

The calculated errors show an excellent correlation between the experimental data and the calculated profiles by the estimate correction method. Also, the root mean square error (RMSE) for the S1 and S3 cores is calculated as 4.3 and 4.9 mm, respectively, which is acceptable.

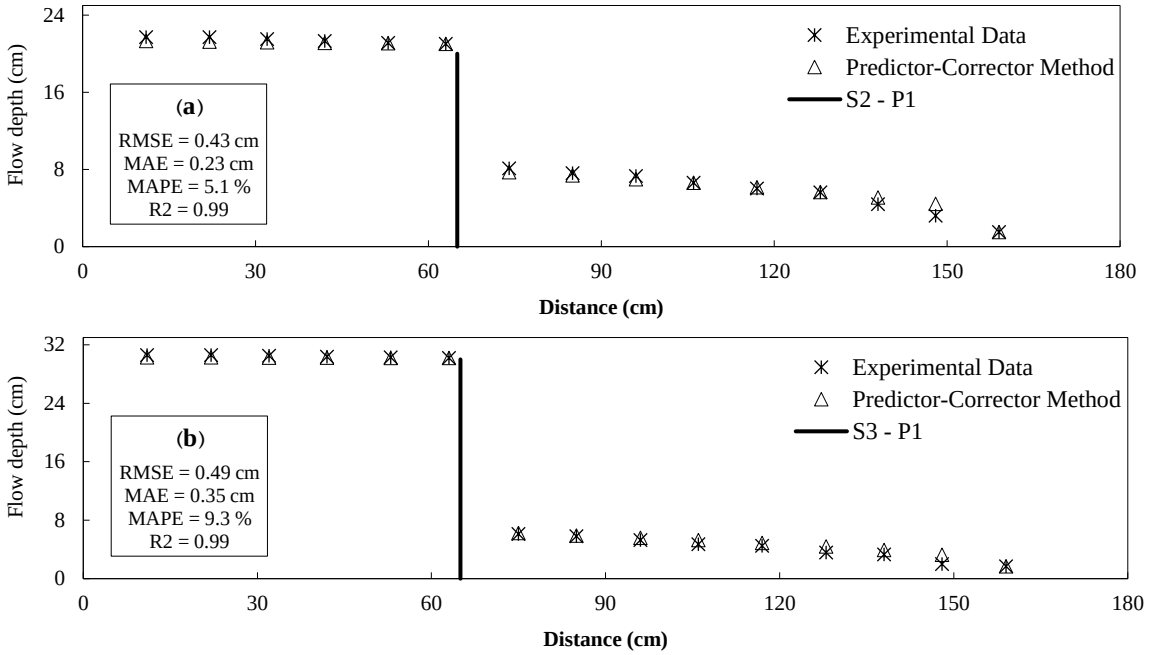


Figure 4. Depiction of water surface profile using experimental data and numerical estimation-correction method in the case of vertical core in position (P1), a) flow discharge 0.26 l/s, b) flow discharge 0.19 l/s

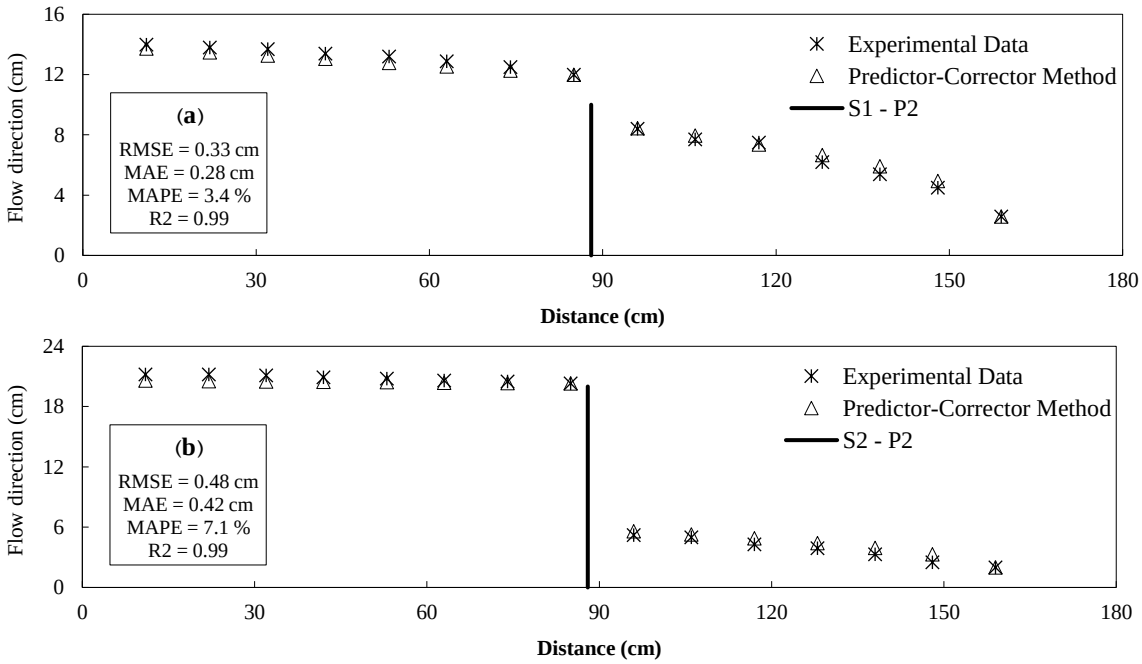


Figure 5. Comparison of depicted water surface profile using laboratory data and estimation-correction numerical method in a vertical core state in position (P2), a) flow rate 0.37 l/s, b) flow rate 0.19 l/s

As is shown in Figs. 4, 5, and 6, the numerical estimation-correction method calculates the surface profile satisfactorily in the presence of vertical cores inside the gravel dam. The root mean square error (RMSE) ranged from 3 to 5.5 mm, and the relative error was calculated between 3 and 9.3 %. Also, the error comparison shows that with the increase in the core height, the error values also increase. This growth is more noticeable downstream of the core. This is because in the vicinity of the core, the flow has local acceleration, and the curvature of the flow is more significant.

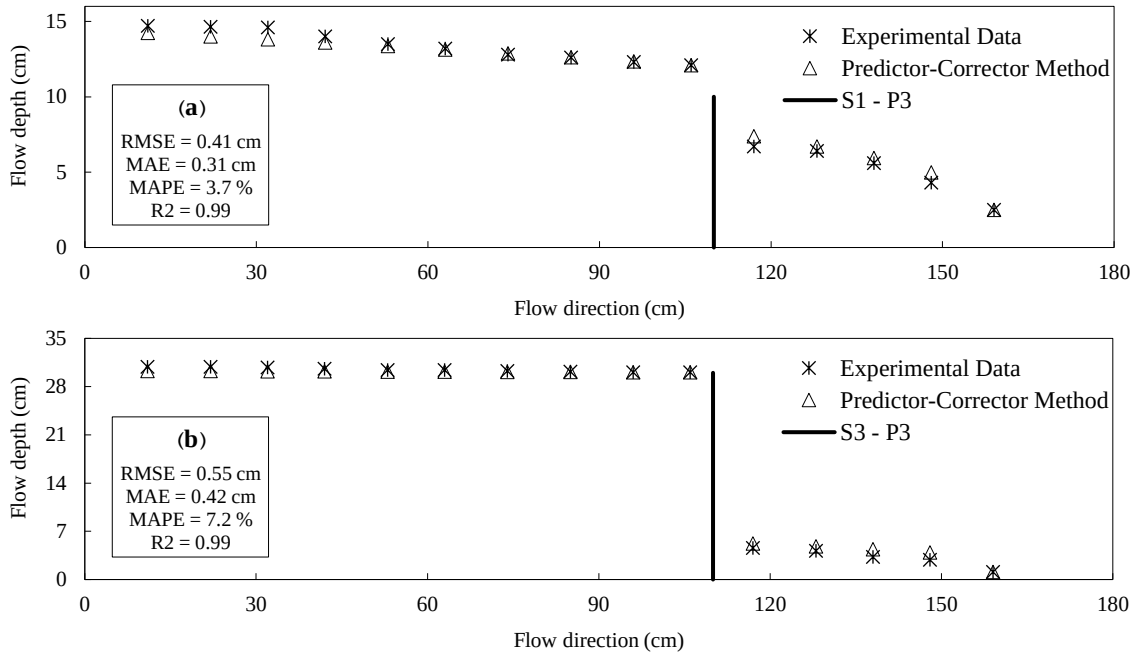


Figure 6. Depiction of water surface profile using laboratory data and estimation-correction numerical method in a vertical core state in position (P2), a) flow rate 0.37 l/s, b) flow rate 0.19 l/s

3.2.2. Flow profile at position P4

In this case, the core encounters the flow and forms an acute angle with the horizon surface. Due to the slope's existence, the current's movement mechanism differs from the vertical core case. If the flow rate is low, the flow slips slowly with contact with the downstream surface of the core. However, the flow falls vertically to the downstream profile for higher flow rates. In Fig. 7, three examples of comparing experimental and numerical results with different flow rates and geometries can be seen in P4.

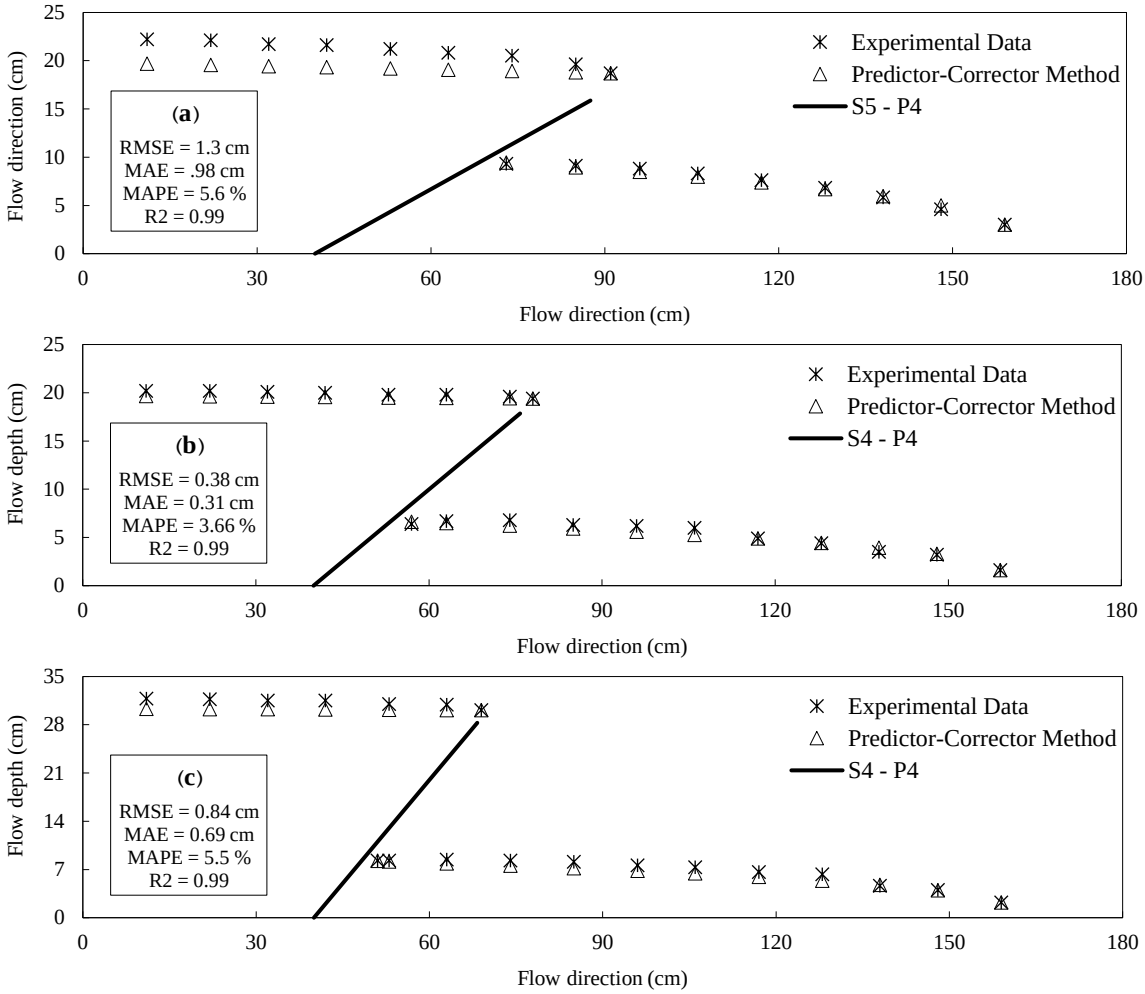


Figure 7. Depiction of flow water surface profile for laboratory data and estimation-correction numerical method in the vertical core state in position (P4).a) flow rate 0.37 l/s, the angle relative to the horizon 18.5 degrees, b) flow rate 0.19 l/s, the angle relative to the horizon 26.5 degrees, c) flow rate 0.26 l/s, the angle to the horizon is 45 degrees.

Error analysis reveals that in the case of an inclined core, the estimation-correction method is less accurate, and the error rate increases with the increase in entrance discharge. It was found that an increase in flow rate increases the flow velocity and local acceleration, especially at the separation point of two profiles, where the curvature of the surface profile is seen. Consequently, the accuracy of the profile computation decreases.

3.2.3. Flow profile at position P5

The inclined core faces the flow at position 5 and forms an acute angle with the horizon in the counterclockwise direction (Fig. 8). In this case, the geometry of the core does not have a considerable effect on the upstream flow, but in downstream it has a significant effect on flow motion pattern inside the rockfill body. This effect is more noticeable at higher flow rates (Fig. 8).

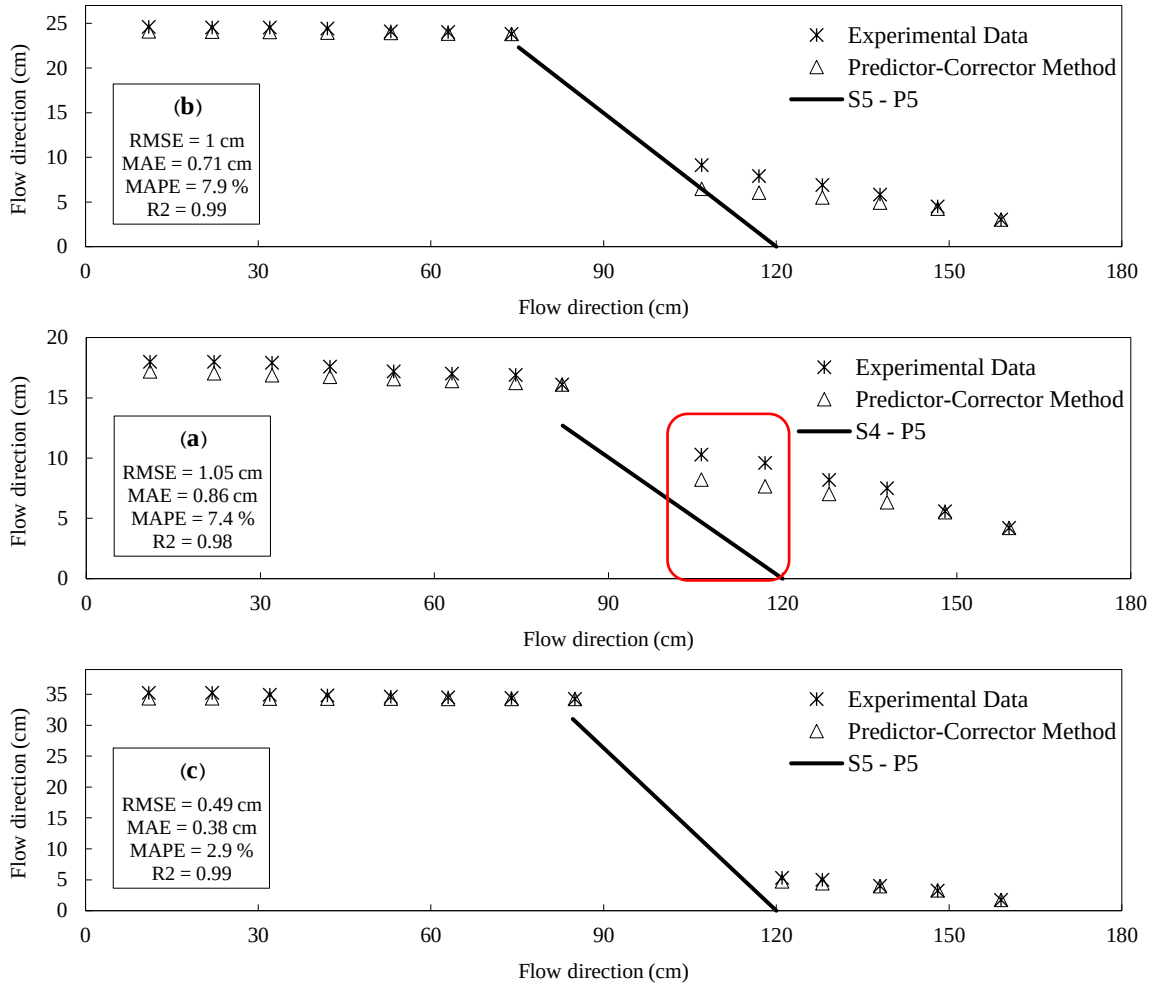


Figure 8. Depiction of water surface profile for laboratory data and numerical estimation-correction method in vertical core mode in position (P5), a) flow rate 0.37 l/s, angle to horizon 18.5 degrees, b) flow rate 0.26 l/s, angle to the horizon 26.5 degrees, c) flow rate 0.19 l/s, angle to the horizon 45 degrees

Fig. 8 shows that at a flow discharge of 0.19 l/s, the relative error is 3%. However, at higher flow rates, this value reaches 8%. Also, the mean square error in the flow rate of 0.37 l/s is 1.1 cm, and for the flow rate of 0.19 l/s, this value is about 0.5 cm. The experimental and the computed profiles using the numerical method of estimation correction are compared by calculating statistical error parameters for all tests (number of tests 63). The detailed results are illustrated in Table 2. Because the number of tests is large and it is not possible to include all of them in the table, the average error parameters for different discharge has been computed. For example, in position 1, the average error of three discharges and three types of core installation (S1, S2, and S3) is averaged and introduced as the error value in position P1.

Table 2. Error values for comparison of laboratory data and numerical solution using estimate-correction method

	Core position				
	P1	**P2**	**P3**	**P4**	**P5**
RMSE (cm)	0.51	0.41	0.48	0.9	0.85
R^2	0.99	0.99	0.99	0.99	0.99
MAPE %	6.4	6.1	6.2	6.6	7.1
MAE (cm)	0.43	0.3	0.32	0.61	0.58

Furthermore, in the extracted analytical relation (Eq. 16), to determine the value of a coefficient to use in the longitudinal profile calculations, it is necessary to use the laboratory results to calibrate it and then evaluate its efficiency. For this purpose, its value is extracted using the least square curve fitting method by taking into account the influencing factors, including the rockfill media diameter, the length of the porous medium, and the operated flow rate for a specific diameter. In the next step, other profiles are calculated and compared with the observed profiles to verify the relationship and obtained value. The comparison results showed that the value of this coefficient does not change by changing the medium's length or the inlet flow rate. Besides, its value for the medium with a rock diameter of 1.8 cm equals 26.5. According to the differences in the flow depth on the porous media, the Reynolds number values ($Re = \frac{uR}{\vartheta}$) would also be variable. As a result, it is necessary to pay attention to the formation or non-Darcy turbulent flow along the entire length of the porous media. The range of calculated Reynolds numbers through longitudinal water surface profiles is 3100 to 11000. It is evident that all are within the range of turbulent flows, and the assumption of the formation of non-Darcy flow is correct. It was also observed that the Reynolds numbers become higher with the increase in discharge and decrease in the porous media length.

4. Conclusion

The application of gradually-varied flow algorithms in simulating buried streams has proven to be an effective and practical approach. By utilizing experimental data and applying the gradually-varied flow theory, water surface profiles have successfully been calculated in various scenarios of non-Darcy flow. In this research, the longitudinal profiles of the water surface were taken in different conditions by conducting a series of experiments in a laboratory flume. Furthermore, a new relationship was presented by analyzing the existing relationships to calculate the flow depth at different longitudinal distances. Coefficients of the presented relationship were calibrated using part of the acquired experimental data. Then, they were used for depth calculation for other laboratory conditions. It was found that in addition to the simplicity of the new relationship, it can be used with acceptable accuracy for predicting the flow profile. Additionally, the flow profile through the porous medium in the presence of inclined and vertical impermeable cores was investigated. The laboratory results were compared with the numerical results, and the error values were calculated. The results showed that the estimated profile by the numerical estimation-correction method has a very high correlation (0.99) with the laboratory data. Also, the average calculated errors indicate the high accuracy of the methods. The computed values for statically RMSE, MAPE, and MAE parameters were calculated as 6.3 mm, 6.5%, and 4.5 mm, respectively. Moreover, it was found that at higher flow rates and in the vicinity of the core edge (the point of profile separation), the flow curvature

was higher, and consequently, the estimation error was higher. In conclusion, the application of gradually-varied flow algorithms in simulating buried streams offers a practical and cost-effective solution for analyzing the behavior of flow in non-Darcy porous media. By combining experimental data, numerical methods, and the gradually-varied flow theory, significant advancements in understanding the complex dynamics of buried streams would be made. This knowledge can be applied to various engineering projects, ensuring the optimal design and operation of hydraulic structures. These findings have significant implications for hydraulic engineering and the design of structures involving buried streams. The ability to accurately predict and simulate the behavior of flow in porous media is crucial for ensuring the safety and efficiency of hydraulic structures.

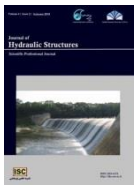
References

1. Mousavi, S., E. Amiri-Tokaldany, and M. Davoudi, A Relationships to Determine the Critical Hydraulic Gradient and Noncohesive Sediment Transport Discharge in Rockfill Dams. Research journal of Environmental sciences, 2011. 5(5): p. 399.
2. Mohamadiha, A., et al., Numerical and Experimental Study of the Unsteady Flow with Different Distance Steps in Body of Rockfill Dam. Iranian Journal of Irrigation & Drainage, 2018. 11(6): p. 1152-1161.
3. Chabokpour, J. and E. Amiri Tokaldany, Experimental-numerical simulation of longitudinal water surface profile through large porous media. Iranian Water Researches Journal, 2017. 11(3): p. 81-90.
4. Acharya, R.C., S.E. van der Zee, and A. Leijnse, Porosity–permeability properties generated with a new 2-parameter 3D hydraulic pore-network model for consolidated and unconsolidated porous media. Advances in water resources, 2004. 27(7): p. 707-723.
5. Constantinides, G.N. and A.C. Payatakes, Network simulation of steady-state two-phase flow in consolidated porous media. AIChE Journal, 1996. 42(2): p. 369-382.
6. Fischer, U. and M.A. Celia, Prediction of relative and absolute permeabilities for gas and water from soil water retention curves using a pore-scale network model. Water Resources Research, 1999. 35(4): p. 1089-1100.
7. Held, R.J. and M.A. Celia, Pore-scale modeling extension of constitutive relationships in the range of residual saturations. 2001, Wiley Online Library.
8. Herrera, N. and G. Felton, Hydraulics of flow through a rockhll dam using sediment-free water. Transactions of the ASAE, 1991. 34(3): p. 871-0875.
9. Hosseini, S.M. and D. Joy, Development of an unsteady model for flow through coarse heterogeneous porous media applicable to valley fills. International Journal of River Basin Management, 2007. 5(4): p. 253-265.
10. Hansen, D., V.K. Garga, and D.R. Townsend, Selection and application of a one-dimensional non-Darcy flow equation for two-dimensional flow through rockfill embankments. Canadian Geotechnical Journal, 1995. 32(2): p. 223-232.
11. Jeannin, P.Y., Modeling flow in phreatic and epiphreatic karst conduits in the Hölloch cave (Muotatal, Switzerland). Water Resources Research, 2001. 37(2): p. 191-200.
12. Li, B., V.K. Garga, and M.H. Davies, Relationships for non-Darcy flow in rockfill. Journal of hydraulic Engineering, 1998. 124(2): p. 206-212.

13. Stephenson, D., Rockfill in hydraulic engineering. 1979: Elsevier.
14. Chabokpour, J., Application of hybrid cells in series model in the pollution transport through layered material. Pollution, 2019. 5(3): p. 473-486.
15. Thauvin, F. and K. Mohanty, Network modeling of non-Darcy flow through porous media. Transport in Porous Media, 1998. 31(1): p. 19-37.
16. Wang, X., F. Thauvin, and K. Mohanty, Non-Darcy flow through anisotropic porous media. Chemical Engineering Science, 1999. 54(12): p. 1859-1869.
17. Wu, Y.S., An approximate analytical solution for non-Darcy flow toward a well in fractured media. Water Resources Research, 2002. 38(3): p. 5-1-5-7.
18. Chabokpour, J., O. Minaei, and M. Dasineh, Derivation of new analytical solution for pollution transport through large porous media. International Journal of Environmental Science & Technology (IJEST), 2020. 17(12).
19. Bazargan, J., et al., Determination of discharge coefficient of inbuilt spillway in rock-fill dams. 2011.
20. Wilkins, J., Flow of water through rock fill and its application to the design of dams. New Zealand Engineering, 1955. 10(11): p. 382-387.
21. Norouzi, H., et al., Estimating output flow depth from Rockfill Porous media. Water Supply, 2021.
22. Sedghi-Asl, M. and I. Ansari, Adoption of extended Dupuit–Forchheimer assumptions to non-Darcy flow problems. Transport in Porous Media, 2016. 113(3): p. 457-469.
23. Heydari, M. and Z. Khodakaramian, One-Dimensional Discharge-Stage Theory Relationship Modifying in non-Core Rock fill Dams Using Laboratory Model. Advanced Technologies in Water Efficiency, 2022. 1(1): p. 108-120.
24. Salahi, M.-B., M. Sedghi-Asl, and M. Parvizi, Nonlinear flow through a packed-column experiment. Journal of Hydrologic Engineering, 2015. 20(9): p. 04015003.
25. Asiaban, P., E. Amiri Tokaldany, and M. Tahmasebi Nasab, Simulation of water surface profile in vertically stratified rockfill dams. International Journal Of Environmental Research, 2015. 9(4): p. 1193-1200.
26. Sarvarian, J., J.M.V. Samani, and H.M.V. Samani, Two-objective Optimization of Location and Geometric Characteristics of Rockfill Dams at the Taleghan Basin by NSGA-II. Environmental Energy and Economic Research, 2018. 2(4): p. 281-296.
27. Zhang, W., et al., A Critical Review of Non-Darcian Flow and Future Challenges. Earth and Space Science Open Archive ESSOAr, 2020.
28. Reddy, H.P., M.H. Chaudhry, and J. Imran, Computation of gradually varied flow in compound open channel networks. Sadhana, 2014. 39: p. 1523-1545.
29. Chaudhry, M.H., Open-channel flow. Vol. 523. 2008: Springer.

© 2024 by the authors. Licensee SCU, Ahvaz, Iran. This article is an open access article distributed under the terms and conditions of the Creative Commons Attribution 4.0 International (CC BY 4.0 license) (http://creativecommons.org/licenses/by/4.0/).

Journal of Hydraulic Structures
J. Hydraul. Struct., 2024; 10(3): 18-33
DOI: 10.22055/jhs.2024.44714.1263



OPEN ACCESS

Experimental study of contaminant mixing through the buried river junctions

Jafar Chabokpour[1]

Abstract

Rivers, as water resources, are considered an origin of supply for many requirements of urban communities. River networks consist of many branches that connect at river confluences. Because pollutants usually enter the river in different situations from the upstream branches of river intersections, it is essential to investigate the mixing process through the river network. For this purpose, precise analytical and numerical models should be used to evaluate this phenomenon quantitatively. Based on the cell concept and separation of advection and dispersion operations, this study developed a new analytical relationship through the confluences of rivers. A physical model of the Y-shaped junction was created in the laboratory, and four inlet flow discharges 25, 21, 12, and 9 l/s and three initial concentrations of sodium chloride solution 80, 160, and 200 g/L were selected as study parameters. Then, the concentration-time curves along the sub-branches, the intersection, and the downstream of the river's main channel were taken at 2-second intervals. In order to evaluate the efficiency of the analytical model, the parameters of the model were first calculated by coding based on its framework and using the least squares method. Then the analytical curves were outlined versus the experimental results. It was observed that the presented model could produce double-peaked curves and also cover experimental data series precisely. The dispersion coefficients and the related time parameter in the presented model (T) were found to increase by moving downstream of the river junction. It was also observed that the Peclet numbers ($P_e = \frac{xu}{D}$) are increased like dispersion coefficients by increasing the distance downstream of the confluence. In addition, the research results showed that increasing the residence time parameter in dispersion cells (T) causes growth in the dispersion coefficient, despite increasing the residence time in advection cells (β), compelling the movement of the pollutant breakthrough curves.

Keywords: Pollutant, river junction, breakthrough curve, mixing, analytical model.

Received: 04 September 2023; Accepted: 31 March 2024

1. Introduction

The importance of solute transport in streams extends beyond aquatic ecosystems. Streams are a significant source of freshwater for human consumption, agriculture, and industry. Therefore, understanding how solutes move through stream networks is crucial for water resource

[1] civil engineering department, University of Maragheh, Maragheh, Iran, Email: J.chabokpour@maragheh.ac.ir **(Corresponding author)**

CC BY

management. Monitoring the quality and concentration of solutes, particularly those related to human activities, can help ensure the safety and sustainability of our water supply [1, 2].

River networks are one of the types of aquatic ecosystems. In these networks, different river branches are connected through river junctions. Exploration regarding hydraulics and flow structure in different types of river intersections has been discussed for a long time. The current patterns through the confluences cause morphological changes and affect the pollution-spreading processes in rivers. The flow ratios of different branches, the angle of river branches concerning each other, and the characteristics of river bed materials are essential and influential parameters in the mixing mechanism [3-6]. Previous studies have focused more on the flow structure and the factors affecting it. Best has done the most fundamental investigation in this field. In his study, six general flow structures were identified in river junctions. Also, the discharge ratio and the angle of the branches introduced essential parameters affecting the flow pattern [3-7].

Solute transport in streams is a complex process influenced by several factors, including hydrological conditions, geological features, and human activities. One of the primary mechanisms of solute transport in streams is advection. Advection refers to the physical movement of solutes with the flowing water. As water travels downstream, solutes dissolved in it move along, creating a downstream gradient. The rate of advection depends on the velocity of the water, and different solutes may have varying speeds of transport. Another important mechanism is hydrodynamic dispersion, which is sum of mechanical dispersion (due to turbulence and mixing) and molecular dispersion and involves the spreading of solutes in the water due to turbulence and mixing. This process occurs because the velocity of water is not uniform across a stream cross-section. Dispersion helps distribute solutes evenly, preventing localized spikes in concentration. Consequently, it supports a more stable and balanced aquatic ecosystem. Additionally, biochemical processes occurring in the stream can influence solute transport. For example, biological uptake involves the absorption of solutes by stream organisms such as algae, bacteria, and other plants. The uptake of nutrients like phosphates or nitrates is beneficial, as it helps regulate their concentration. However, excessive nutrient uptake could lead to imbalances and negatively affect aquatic life [8, 9].

Best & Reid [7] found that with the increase in the discharge ratios, the length and width of the separation zone in river junctions improved, but its shape index (the ratio of maximum width to length) remained constant. Qing-Yuan et al. [10] found that the isoline method, in which the boundary of the separation zone is determined using the zero longitudinal velocity line, is more accurate than the streamline method. In addition to the mentioned cases, transverse eddies and their advection downstream have been proven at the river junction. The presence of these vortices increases the stress and, as a result, erosion at the intersection, which ultimately causes morphological changes in the intersection [4, 11].

Through high-frequency velocimeter devices, Biron et al. [12] and Rhoads & Sukhodolov [13] acquired the velocity data through the natural river junctions and studied the shear layer in the intersection. Shakibainia et al. [14] reported the existence of three types of swirling currents in the main channel, the branch, and the separation zone. They claimed that the eddy currents in the separation zone are the primary causality for forming the separation zone. They also claimed that this type of swirling currents did not exist at the intersections of natural rivers due to sedimentation, while the swirling currents formed by the sub-branches were due to the deviation of the general flow path. Through the junction, it is the most vital type of swirling current, and the interference with the swirling flow of the branch also causes the swirling flow related to the main channel. The swirling currents related to the main river channel also become more assertive and

more dominant with the increase in the angle of the sub-channel and the ratio of discharges [14, 15].

Many researchers have widely studied the effect of the 3D structure of river junctions' location on the intersection's hydrodynamics. The flow deviation in the river's main channel may not exist due to the three-dimensional conditions of the bed at the intersection, and as a result, the separation zone is diverted to zones with lower depths. In this case, the separation region is apparent at the surface of the flow, but this zone will not exist at the lower flow depths [16-19].

Many studies on hydrodynamic characteristics through the river junctions have been done; however, sufficient studies have not been conducted on the mixing of pollution through the river confluences. The operated investigations are mainly based on the mixing rate. Based on the research done by [20] , deep mixing is achieved in length equal to several tens of times the average flow depth, but completing transverse mixing requires a much longer length. They claimed that for a wide river, the required length for complete transverse mixing is 100-1000 times the main channel width. However, other researchers such as Gaudet & Roy [21] reported this mixing much faster and claimed that this mixing is completed at a distance equal to 25 times the river channel width. Both previous experimental and numerical studies have increased our knowledge about the flow structure and the mixing process, but most of the experimental data, due to the limitations of the measurement tools, are not accurate for predicting the complex mechanism of mixing through the confluences. For this reason, numerical modeling has been used as a complementary tool to experimental analysis. Mignot et al. [22] used the turbulence (k-ϵ) model to simulate the applied lateral flow.

Also, many previous studies have been done on irregular junction shapes, which causes an uncertainty in results. There are also regular types of river intersections, named Y-shaped confluence, in which their analysis results are more comprehensive.

Weidong et al.; Weidong & Yue [23, 24] studied the flow patterns using the ADV velocimeter data collected through the river confluence. Several zones, named stagnant zone, flow deviation zone, flow separation zone, and acceleration zone, have been observed through the confluences. Also, the circular flow pattern downstream of the junction was observed. Furthermore, with the increase in the flow ratio of the branches, the strength of the rotating current downstream of the junction decreases. Rhoads & Sukhodolov [25] found that the rotational flow downstream of the conjunction increases the mixing rate of passing pollutants. Also, they claimed that in regular geometric confluences, the mixing is more evident, but in irregular geometric intersections, it is not apparent with the precision of the previous state. Similarly, Geberemariam [26] concluded that in T and Y shape junctions, the discharge ratio and the area of the separation zone, due to the presence of rotating currents, are inversely related. Generally, it can be said that based on previous studies, various models have been developed and used for pollution transport modeling. Some investigators have simulated the concentration breakthrough curves using statistical distribution models. Another number of them have tried to simulate the mass exchange between the mainstream and the dead zone areas inside the rivers.

Biron et al. conducted numerical simulations of pollutant mixing in an open channel and found that the mixing process was faster when there were inconsistencies in riverbed depths between the main channel and tributaries [6]. The concentration of pollutants in different cross-sectional areas was found to be influenced by the distance from the junction point and the discharge ratio [8].

The flow structure and turbulence at river confluences also play a crucial role in pollutant transport. The shear layer and counter-rotating helical cells in the flow field control the distribution of contaminant concentrations. The turbulent kinetic energy, Reynolds shear stress, and turbulence spectrum are important parameters that affect the turbulent flow structure and the dispersion of

contaminants. The pressure gradient and convective acceleration are key factors in triggering velocity redistribution and influencing the transport of pollutants. However, most of these studies have focused on asymmetrical river confluences, and there is limited research on the transport of contaminants at Y-shaped confluences [27].

Some researchers have also investigated the effect of bedforms on contaminant advection and dispersion [28-31]. Radu et al. [32], using a physical model of a river junction similar to the Danube River, investigated the mixing of pollutants entering the different branches of this river based on a two-dimensional model. In some investigations, including the Tantemsapya et al. [33], an attempt was made to remove or reduce the concentration of pollutants in the river by adding some chemical compounds to the stream. Using a two-dimensional model, Park & Seo [34], investigated contaminant transport through the streams on non-Fickian conditions.

Also, Pengpom et al. [35] performed a two-dimensional numerical finite element simulation through one of Thailand's river confluences. In this research, the impact of flow velocity in the upstream branches and the main channel, as well as the contaminant concentration, were studied. It was concluded that the increasing flow velocity through the upstream branches causes the intense mixing of pollutants and reduced contaminant concentration at the junction.

Lyubimova et al. [36] explored the causes for the weakening of transverse mixing mechanisms through the junctions and claimed that by weakening flow turbulence through the junctions, secondary currents would not appear in this part of the river and consequently, complete mixing flows with different density may not occur even at very long lengths.

Cheng et al. [37] claimed that river confluences significantly impact flow hydraulics, sediment transport, and the size of the riverbed storage area, where a percentage of the pollution mass is temporally trapped. However, it was stated that due to the morphological complexities of river junctions, it is not easy to calculate the contaminant mass trapping rate in the storage area.

From the summary of previous studies, it can be found that many studies have been conducted in the domain of mixing and pollution transport in rivers; however, except for a few cases, many studies have not been done in the area of contaminant mixing through the river junctions. In addition, using two-pulse contaminants injection in the upstream branches will also define more issues of the mixing process through the junction region. Generally, it can be said that a few numbers of analytical equations have been developed regarding the mixing mechanism through the river confluences. For this purpose, the present study was designed to explore more junction zone transport characteristics.

2. Materials and methods

2.1. Experimental data

In order to carry out the present study, a wide laboratory flume was used, and inside it, a Y-shaped junction with different branch widths was created. The laboratory flume had the dimensions of (14x1.2x1) meters in length, width, and height, respectively. The 1.2-meter-wide laboratory flume was divided into two branches with 25 and 45-cm dimensions, intersecting at a 45-degree angle.

The junction was filled with rockfill material with depth of 50 cm to present buried stream junction. A transverse contaminant injector was installed upstream of both branches and was used to employ the mass conservative sodium chloride contaminant solution. The schematic of different parts of the laboratory model of the river junction is depicted in Fig. 1. Four flow discharges of 9, 12, 21, and 25 l/s were employed as flow variables in the experiments, and three initial concentrations of 80, 160, and 200 gr/l were selected and applied as concentration parameters to the upstream branches. Electrical conductivity sensors are installed and connected to the data

logger as depicted in Fig.2. The electrical conductivity recording process started in 2-second intervals. In Fig.2, these sensors' distances and installation conditions are shown in detail through different parts of the experimental model. Sensors No. 1 and 2 were installed in the branch with a width of 45 cm, and sensors No. 3 and 4 were installed in the branch with a width of 25 cm. Sensor No. 5 was used to monitor electrical conductivity variation through the confluence, and finally, sensors No. 6 to 8 were placed downstream of the junction at regular intervals. The experiments were started after stabilizing the flow discharge through the laboratory flume, simultaneously with the injection of the pulse of the pollutant (sodium chloride solution) in both branches. The data recording was also started, and then, by a delay of 15 seconds, the second pulse of the pollutant was injected using a transverse feeder. The sensors recorded the overlap of entrance breakthrough curves. The duration of data collection was controlled through the graphical interface of the data collection system and continued until the concentration recovered to the flume flow's primary concentration.

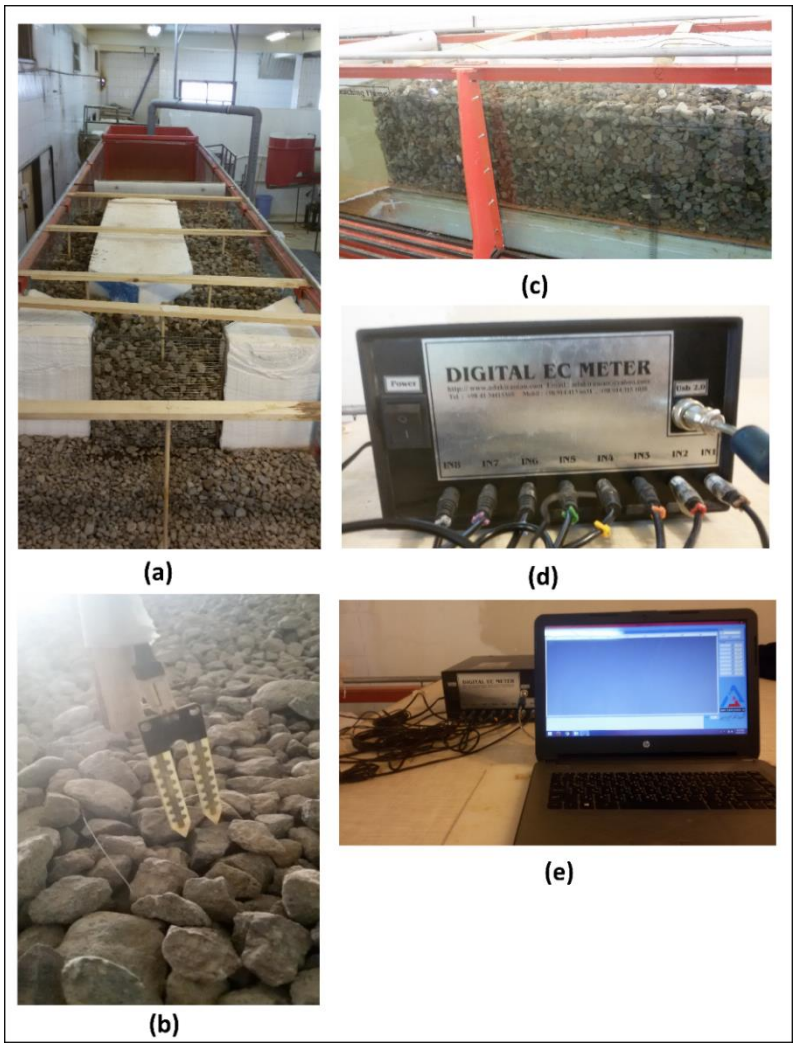


Figure 1. (a) The plan of river laboratory river branches and their junction, (b) installed electrical conductivity sensors (c), filling the area of the river junction to a height of 50 cm (d), data logger of electrical conductivity sensors (e), user interface of data collection software

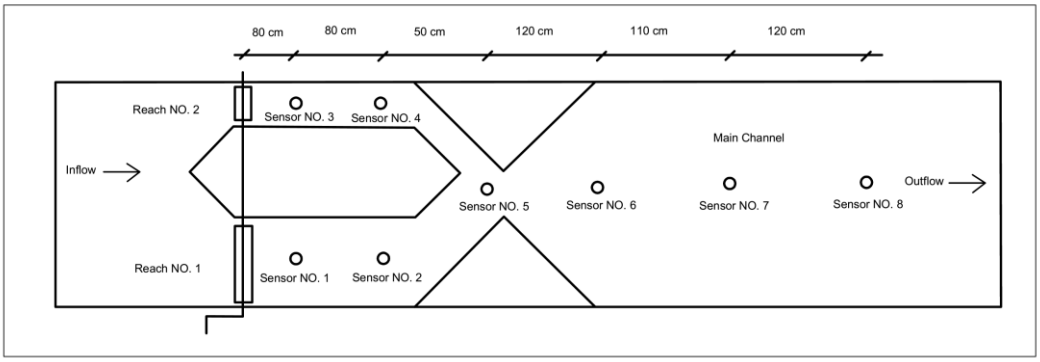


Figure 2. Location of the sensors and their installation distances in the laboratory flume

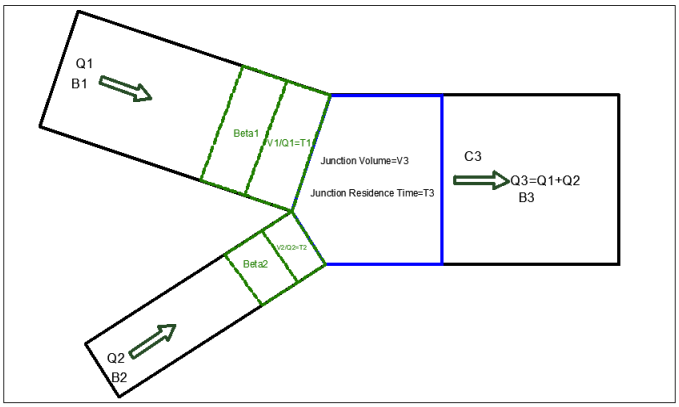
2.2. Extraction of analytical relationship based on the schematic of pollutant entrance from two upstream branches through the river junction

This research tried to develop a new analytical relationship based on the conceptual model of contaminant entrance from the two upstream branches through the junction by creating a conceptual model and applying the mass conservation relationship. The general method used in extracting this relationship was derived based on the hybrid cell model previously introduced by Ghosh et al. [32]. The general schematic designed cell system for upstream branches and river confluence is shown in Fig. 3. As indicated, the area of the junction is divided into three cells: the first cell represents branch No.1 from the upstream, the second cell represents the branch No. 2 from the upstream, and finally the third cell represents the main river area junction. It also mentions that this relationship is based on completing transverse mixing through the confluence. In other words, the size of this cell is assumed to be large enough so that the complete transverse mixing occurs or the pollution concentration is equal in all parts of this cell. The initial conditions upstream of both cells are expressed as Eqs. 1 and 2.

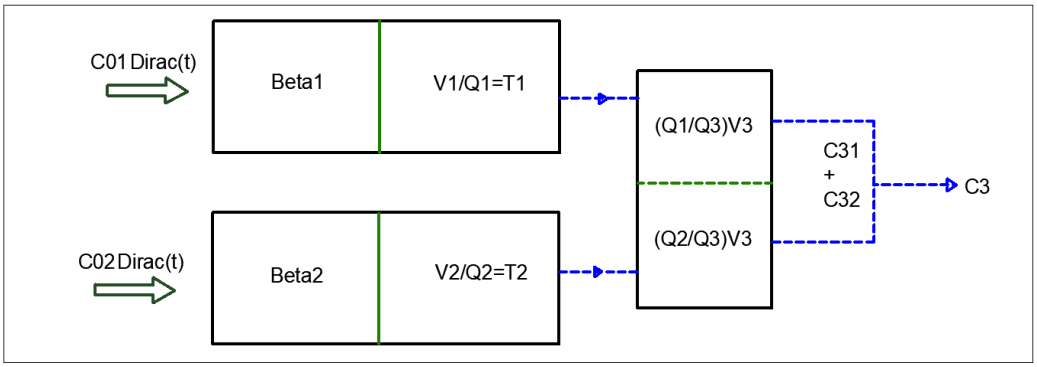
$$C_1(0) = C_{01}\text{Dirac}(t) \quad (1)$$

$$C_2(0) = C_{02}\text{Dirac}(t) \quad (2)$$

In the above equations, the Dirac(t) function has zero value at all points and infinity at t=0.



(a)



(b)

Figure 3. (a) Cell connections through the river confluence, (b) Schematic of conceptual cells for extracting the analytical relationship

As shown in Fig. 3, the cells of the upstream branches are divided into two separate cells. One is for advection modeling, and the other is for dispersion process modeling of pollutants. The output flow concentration is obtained by applying the upstream initial conditions in the advection cells as Eqs. 4 and 5.

$$C_1(0) = C_{01}\text{Dirac}(t-\beta_1) \quad (3)$$

$$C_2(0) = C_{02}\text{Dirac}(t-\beta_2) \quad (4)$$

The above relationships of β_1 and $\beta_2$equal the residence time of advection cells in the first and second branches upstream of the river junction. Mass conservation equations were written for each cell as the pollutant entered the dispersion cells. The extracted differential equations for the upstream branches of the junction are according to Eqs. 5 and 6.

$$\frac{dC_1(t)}{dt} + C_1(t)\left(\frac{1}{T_1}\right) = \frac{C_{01}\text{Dirac}(t-\beta_1)}{T_1} \quad (5)$$

$$\frac{dC_2(t)}{dt} + C_2(t)\left(\frac{1}{T_2}\right) = \frac{C_{02}\text{Dirac}(t-\beta_2)}{T_2} \quad (6)$$

In the above relationships, T_1 and T_2 are the pollutant residence time through the dispersion cells and are obtained by dividing the cell volume by the flow discharge. For example, $T_1 = \frac{V_1}{Q_1}$, in which V_1 is cell volume, and Q is the passing flow through branch number 1. By assuming the injected pollutant concentration at the beginning of the experiment is equal to C_i, it can be said that the initial condition in the mentioned cells is equal to $C_1(\beta_1) = C_1(\beta_2) = C_i$. Therefore, Eqs. 7 and 8 would be obtained by applying these boundary conditions and solving the above differential equations.

$$C_1(t) = \left(\frac{C_{01}\text{Heaviside}(t-\beta_1)\times\exp\left(\frac{\beta_1}{T_1}\right)}{T_1} + \frac{C_i}{\exp\left(-\frac{\beta_1}{T_1}\right)}\right) \times \exp\left(-\frac{t}{T_1}\right) \quad (7)$$

$$C_2(t) = \left(\frac{C_{02}\text{Heaviside}(t-\beta_2)\times\exp\left(\frac{\beta_2}{T_2}\right)}{T_2} + \frac{C_i}{\exp\left(-\frac{\beta_2}{T_2}\right)}\right) \times \exp\left(-\frac{t}{T_2}\right) \quad (8)$$

In which Heaviside is step function.

By precision in Fig. 3, it is evident that the exiting pollutant from both upstream branches jointly enter a new cell, in which a hypothetical buffer curtain is included. The pollution from upstream branches enters the junction cell. The volume of the junction cell is not divided equally for the entering pollutants from the upstream branches. It was related to the flow rate of each branch. The volume of the mentioned cell is assumed to be equal to V_3, and $Q_3 = Q_1 + Q_2$ is equal to the total discharge of the river main channel, which comes by adding branch discharges. The share of the first branch from the confluence cell is equal to $(\frac{Q_1}{Q_3}) \times V_3$, and similarly the share of the second branch is equal to $(\frac{Q_2}{Q_3}) \times V_3$. Then, the mass conservation equations are written along the confluence cell, and consequently, Eqs. 9 and 10 are obtained.

$$\frac{dC_{31}(t)}{dt} + C_{31}(t)\left(\frac{1}{T_3}\right) = \frac{\left(\frac{C_{01}\text{Heaviside}(t-\beta_1)\times\exp\left(\frac{\beta_1}{T_1}\right)}{T_1} + \frac{C_i}{\exp\left(-\frac{\beta_1}{T_1}\right)}\right)\times\exp\left(-\frac{t}{T_1}\right)}{T_3} \quad (9)$$

$$\frac{dC_{32}(t)}{dt} + C_{32}(t)\left(\frac{1}{T_3}\right) = \frac{\left(\frac{C_{02}\text{Heaviside}(t-\beta_2)\times\exp\left(\frac{\beta_2}{T_2}\right)}{T_2} + \frac{C_i}{\exp\left(-\frac{\beta_2}{T_2}\right)}\right)\times\exp\left(-\frac{t}{T_2}\right)}{T_3} \quad (10)$$

They are solved by applying the initial conditions in the above differential equations as $C_{31}(\beta_1) = C_{32}(\beta_2) = C_i$. The two obtained equations are added together according to the depicted conceptual schematic. In order to further simplify, it is assumed that the initial concentration of the pollutant through the river branches is equal to zero ($C_i = 0$). Ultimately, Eq. 11 is obtained for output contaminant concentration through the confluence.

$$\begin{aligned} C_3(t) = -\frac{1}{(T_1-T_3)(T_2-T_3)}\big((-C_{01}\text{Heaviside}(t-\beta_1)(T_2-T_3)\times \\ \exp\left(\frac{(\beta_1-t)T_3+tT_1}{T_1T_3}\right) - C_{02}\text{Heaviside}(t-\beta_2)(T_1-T_3)\times \\ \exp\left(\frac{(\beta_2-t)T_3+tT_2}{T_2T_3}\right) + C_{01}\text{Heaviside}(t-\beta_1)(T_2-T_3)\times \\ \exp\left(\frac{\beta_1}{T_3}\right) + C_{02}\text{Heaviside}(t-\beta_2)(T_1-T_3)\times\exp\left(\frac{\beta_2}{T_3}\right))\times\exp\left(-\frac{t}{T_3}\right)) \end{aligned} \quad (11)$$

3. Results

3.1. Examining the parameters of the presented analytical model

Pollutant transport in river confluences is influenced by the hydrodynamic characteristics of the flow, including flow velocity, turbulence intensity, and residence time. Experimental modeling helps to understand how these factors affect the movement and spread of pollutants. Studies using experimental modeling have shown that pollutants introduced into the upstream river can be transported along different paths within the confluence zone. Some pollutants are rapidly transported downstream, while others may be trapped within the confluence due to eddies and flow patterns. Additionally, the concentration and distribution of pollutants can vary significantly within the confluence, indicating the complexities of pollutant transport in this dynamic environment.

Considering that the obtained model comes from the combination of inlet breakthrough curves from two upstream branches, it must be capable of reconstructing the double-peak breakthrough curves. Therefore, in the first step, it was tried to investigate this possibility by considering the

numerical values for the model parameters. Fig. 4 is an example of the obtained curves using this model, in which we can see the model's capability.

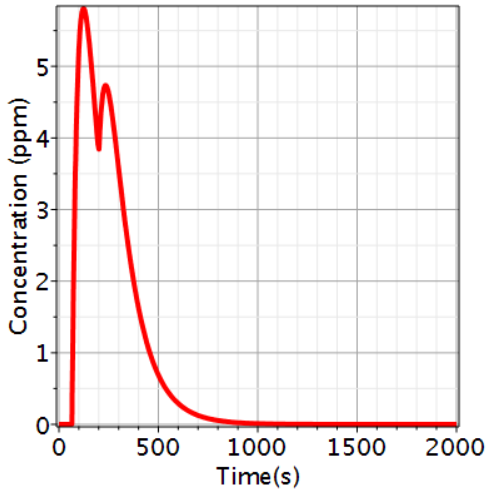


Figure 4. Reconstructing the BC curves by the presented analytical model

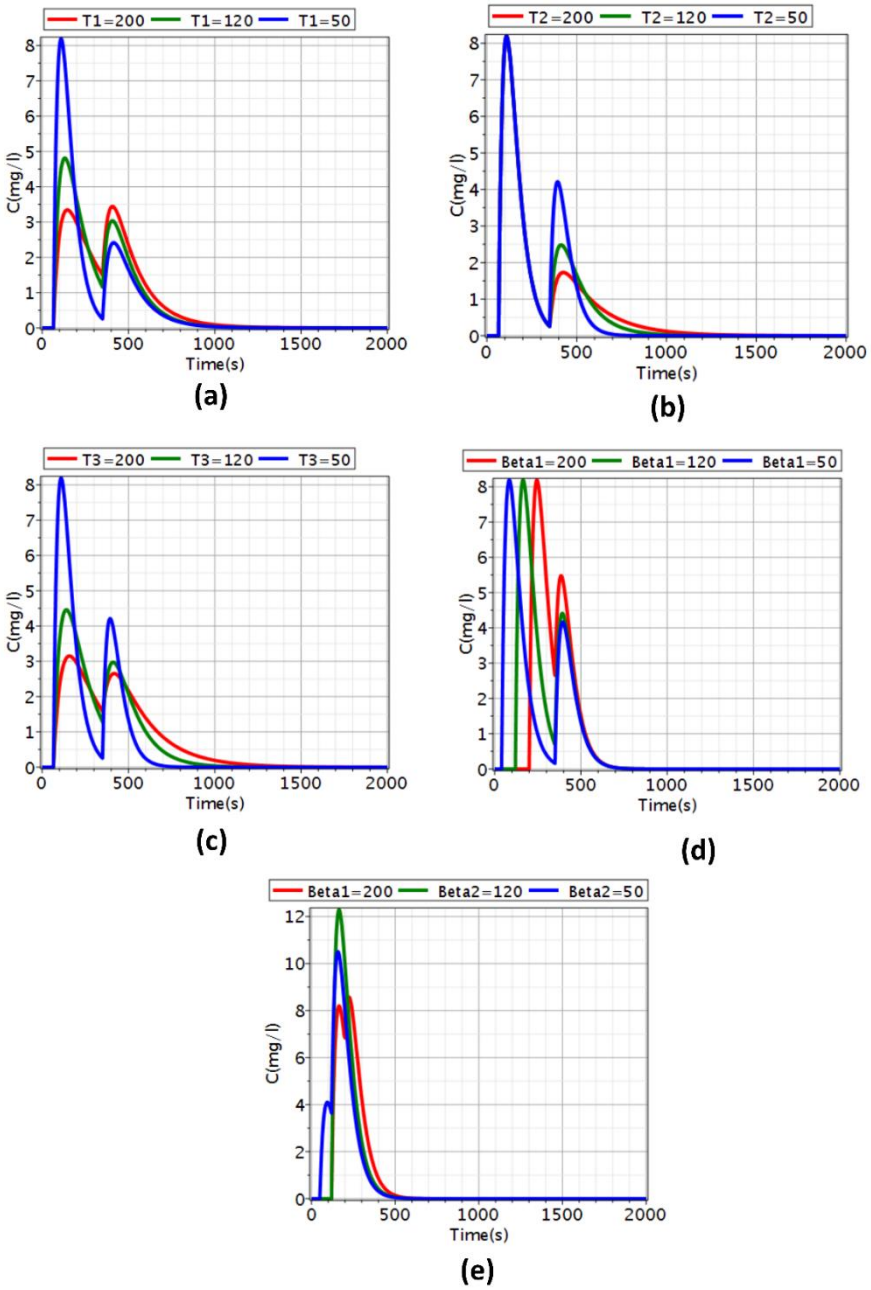
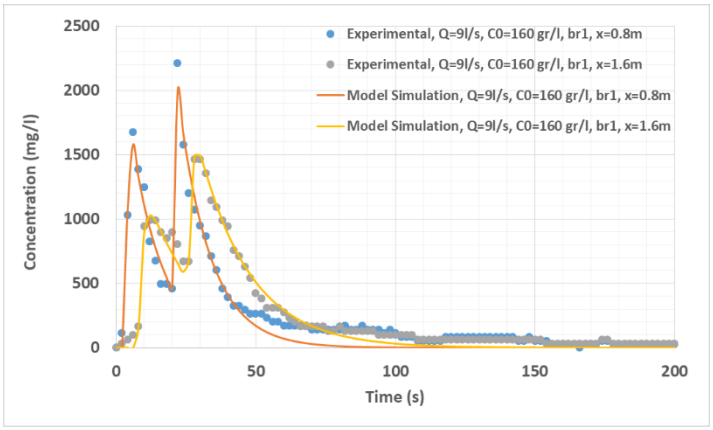


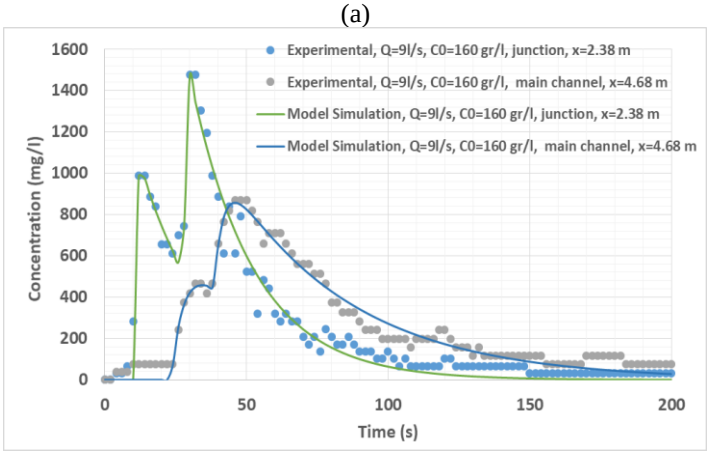
Figure 5. The effect of variation in the model parameters on the shape of the extracted BC curves, (a) the effect of variation in the T_1parameter, (b) the effect of variation in the T_2parameter, (c) the effect of variation in the T_3 parameter, d) the effect of variation in the β_1 parameter, (e) the effect of variation in the β_2 parameter

Then, it was tried to investigate the effect of variation of each parameter in the figure of concentration-time curves. For this purpose, three values of 40, 120, and 200 seconds were used for the model's five temporal parameters, and their effect on the shapes of breakthrough curves was observed. In the first step, by examining the T_1 parameter, it was observed that the increase

of this parameter causes an increase in the spreading power in the first pulse of the breakthrough curve, while in the second pulse, it shows the contrasting effect (Fig. 5, a). The T_2 parameter only affects the second pulse and does not affect the shape of the concentration-time curve in the first pulse (Fig. 5, b). It is worth mentioning that the effect of improving this parameter in the second pulse of the breakthrough curve is similar to T_1 and causes a growth in the pollution spread of the second pulse. The effect of the T_3 parameter is familiar in both pulses of the concentration-time curve, such that with its increase, the dispersion effect is observed in both pulses of the BC curve, and conversely, with its decrease, the maximum concentration values of the curve pulses increase (Figure 5, c). Generally, it can be concluded that the model's temporal parameters are directly related to the dispersion coefficient of the classical advection-dispersion model. However, the effect of these time parameters in the first and second pulses is not the same. Regarding the model's advection time parameters (β_1, β_2), it can be concluded that the β_1 parameter in the first pulse of the curve only has the convection effect, so increasing its value causes shifting of the BC curve toward the right side. However, in the second pulse of the curve, an increase in the maximum concentration is also observed (Fig. 5, d). Otherwise, concerning the β_2 parameter, it can be said that reducing its value causes the second pulse of the curve to merge into the first pulse so that the BC curve's shape transforms from a double peak to a single one (Fig. 5, e).



(a)



(b)

Figure 6. (a) Observed and simulated BC curves through the upstream branch, (b) Observed and simulated BC curves at the river junction and downstream of the river confluence.

The main issue with the presented analytical model is to examine its simulation capability. For this purpose, the analytical curves were reconstructed and depicted by coding in MATLAB software and extracting the model parameters. Two examples of these simulations are shown in Fig. 6. The first part of this figure is associated with one of the upstream branches, and the second part is related to the junction point and downstream. The general trend shows a good match between the simulated curves and the experimental data. In order to quantitatively evaluate this match, the statistical parameters of root mean square error (RMSE), mean maximum error (MAE), and Nash-Sutcliffe index (DC) were used, and their values were calculated for all the experimental data as 0.1, 72 (ppm) and 0.83, respectively. The Nash-Sutcliffe Efficiency is calculated as one less the error variability of a modeled time series divided by the observed time series variation. Since model errors may have a normal distribution rather than a uniform distribution, RMSE is a good metric for this type of data. In addition, the average absolute error (MAE) measures the average absolute difference between a prediction value and a real value. All errors are given the same weight and are less sensitive to deviations. MAE is useful when it is aimed at minimizing overall errors in the model and avoiding large errors. Computed values also indicate the good performance of the proposed analytical model. It was also observed that by increasing the length and moving downstream of the river confluence, the curves transformed from a two-peaked state to a single-peaked one because of the longitudinal diffusion process.

Further, in order to better understand the advection and dispersion of pollutants in the upstream branches, the junction and the main channel, the process was discussed and investigated using the calculation of the common advection-dispersion parameters. For this purpose, the classical ADE model (Eq. 12) was also used to perform the physical interpretation of this process using ADE model parameters.

$$C(x,t) = \frac{M}{A\sqrt{4\pi Dt}} \exp\left(-\frac{(x-ut)^2}{4Dt}\right) \quad (12)$$

Where M is the injected pollutant mass, A cross section area, D is the longitudinal diffusion coefficient, x is the length parameter, t is the time parameter, and u is the average flow velocity.

For this purpose, after applying the common spatial basis to all the extracted curves, model parameters were also extracted and after depicting them against each other (Fig. 7), their variations were explored. In part (a) of Fig. 7, the longitudinal dispersion coefficient values are plotted versus the distance from the injection site. As is shown, the dispersion coefficient has risen with the increase of the distance parameter, while the scattering of its values has also increased. In part (b), the values of the average velocity are plotted versus the longitudinal dispersion coefficient. It is clear that with the increase of the flow velocity, the dispersion coefficient has also increased. Also in part (c), the values of Peclet number ($P_e = \frac{xu}{D}$), which indicates the ratio of advection power to dispersion in the river channel, are plotted versus the values of diffusivity ($\frac{D}{u}$). As indicated, the transmisability values have decreased exponentially with the increase of Peclet number, and finally, in part (d) of Fig. 7, the variation of Peclet number are plotted against the longitudinal distance from the injection site. It was observed that Pe numbers increase with the growth of the length parameter, which indicates that the transfer process is stronger than the dispersion process.

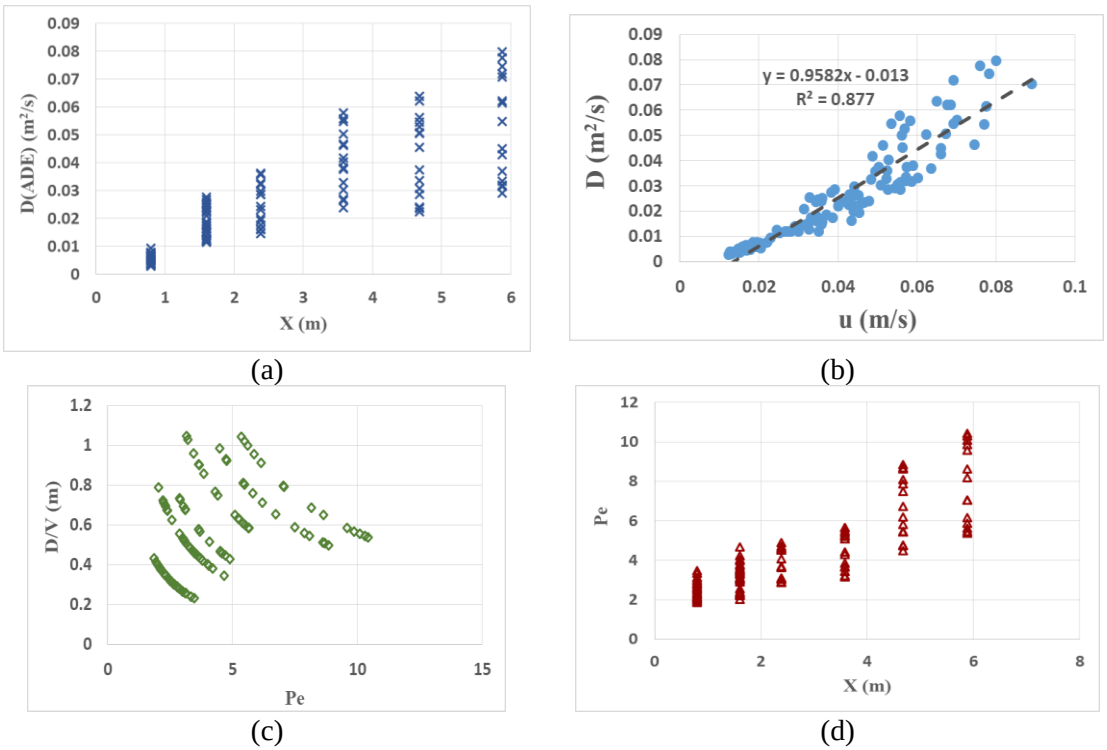


Figure 7. (a) D parameter variation along the river, (b) D parameter versus u parameter, (c) D/u parameter variation versus Peclet number, (d) Peclet number variations versus distance

4. Conclusion

In the quantitative investigation of the advection and dispersion process of pollutants through the river network, their detailed analysis at river junctions is one of the most critical issues. Due to the lack of knowledge in this regard, in the current study, it was tried to create a conceptual model of a river confluence with two sub-branches. Then, solving differential equations, an explicit equation was extracted based on the cell residence time characteristics of the upstream branches and junction zone. The presented relationship can create two-part and double-peak curves according to the general nature of the breakthrough curves through the confluences. Sodium chloride solution was selected as a mass conservative pollutant, and laboratory data was acquired. The results showed a very good agreement with the analytical model. All model parameters are temporal and gain different values based on residence time through the different parts of the conceptual model. In order to examine the temporal parameter's effect, they were varied one by one by keeping the rest of the parameter's constant, and then the artificial concentration-time curves were produced and analyzed. Additionally, the analytical curves were reconstructed and depicted by coding in MATLAB software and extracting the model parameters. The general trend shows a good match between the simulated curves and the experimental data. The model's temporal parameters were also extracted and after depicting them against each other, their variations were explored. The results show that the dispersion coefficient has risen with the increase of the distance parameter, while the scattering of its values has also increased. It was also observed that the Pe numbers increase with the growth of the length parameter, which indicates that the transfer process is stronger than the dispersed process. Generally, it was observed that the increase in the residence time of the pollutant through the diffusion cells of the model (T) causes

an increase in dispersion. On the other hand, an increase in the model's advection parameter (β) causes the right side shifting of the curve. Next, applying the least squares curve fitting method to the collected laboratory data, the actual model parameters were estimated, and then theoretical curves were created versus experimental ones. Three statistical parameters (RMSE), (MAE), and (DC) were used to test the efficiency of the model. The values of these three parameters were equal to 0.1, 72 (ppm), and 0.83, respectively, which indicates the proper functioning of the presented analytical model.

References

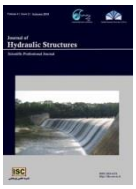
1. J. Chabokpour, B. Chaplot, M. Dasineh, A. Ghaderi, and H. M. Azamathulla, "Functioning of the multilinear lag-cascade flood routing model as a means of transporting pollutants in the river," *Water Supply*, vol. 20, no. 7, pp. 2845-2857, 2020.
2. J. Chabokpour, H. M. Azamathulla, Y. Azhdan, and M. Ziaei, "Study of pollution transport through the river confluences by derivation of an analytical model," *Water Science and Technology*, vol. 82, no. 10, pp. 2062-2075, 2020.
3. J. L. Best, "Flow dynamics and sediment transport at river channel confluences," Birkbeck (University of London), 1985.
4. J. L. Best, "Flow dynamics at river channel confluences: implications for sediment transport and bed morphology," 1987.
5. J. L. Best, "Sediment transport and bed morphology at river channel confluences," *Sedimentology*, vol. 35, no. 3, pp. 481-498, 1988.
6. P. Biron, J. L. Best, and A. G. Roy, "Effects of bed discordance on flow dynamics at open channel confluences," *Journal of Hydraulic Engineering*, vol. 122, no. 12, pp. 676-682, 1996.
7. J. L. Best and I. Reid, "Separation zone at open-channel junctions," *Journal of Hydraulic Engineering*, vol. 110, no. 11, pp. 1588-1594, 1984.
8. J. Chabokpour and A. Samadi, "Analytical solution of reactive hybrid cells in series (HCIS) model for pollution transport through the rivers," *Hydrological Sciences Journal*, vol. 65, no. 14, pp. 2499-2507, 2020.
9. J. Chabokpour, "Study of pollution transport through the rivers using aggregated dead zone and hybrid cells in series models," *International Journal of Environmental Science and Technology*, vol. 17, no. 10, pp. 4313-4330, 2020.
10. Y. Qing-Yuan, W. Xian-Ye, L. Wei-Zhen, and W. Xie-Kang, "Experimental study on characteristics of separation zone in confluence zones in rivers," *Journal of Hydrologic Engineering*, vol. 14, no. 2, pp. 166-171, 2009.
11. M. Leite Ribeiro, K. Blanckaert, A. Roy, and A. J. Schleiss, "Flow and sediment dynamics in channel confluences," *Journal of Geophysical Research: Earth Surface*, vol. 117, no. F1, 2012.
12. P. Biron, B. De Serres, A. Roy, and J. L. Best, "Shear layer turbulence at an unequal depth channel confluence," in *Turbulence: Perspectives on Flow and Sediment Transfer*: John Wiley & Sons, Ltd., 1993, pp. 197-213.
13. B. L. Rhoads and A. N. Sukhodolov, "Spatial and temporal structure of shear layer turbulence at a stream confluence," *Water Resources Research*, vol. 40, no. 6, 2004.
14. A. Shakibainia, M. R. M. Tabatabai, and A. R. Zarrati, "Three-dimensional numerical study of flow structure in channel confluences," *Canadian Journal of Civil Engineering*, vol. 37, no. 5, pp. 772-781, 2010.

15. S. Yuan, H. Tang, Y. Xiao, X. Qiu, H. Zhang, and D. Yu, "Turbulent flow structure at a 90-degree open channel confluence: Accounting for the distortion of the shear layer," *Journal of hydro-environment research*, vol. 12, pp. 130-147, 2016.
16. B. De Serres, A. G. Roy, P. M. Biron, and J. L. Best, "Three-dimensional structure of flow at a confluence of river channels with discordant beds," *Geomorphology*, vol. 26, no. 4, pp. 313-335, 1999.
17. K. Bradbrook, S. Lane, K. Richards, P. Biron, and A. Roy, "Role of bed discordance at asymmetrical river confluences," *Journal of hydraulic engineering*, vol. 127, no. 5, pp. 351-368, 2001.
18. X.-g. Wang, Z.-m. Yan, and W.-d. Guo, "Three-dimensional simulation for effects of bed discordance on flow dynamics at Y-shaped open channel confluences," *Journal of Hydrodynamics, Ser. B*, vol. 19, no. 5, pp. 587-593, 2007.
19. C. Boyer, A. G. Roy, and J. L. Best, "Dynamics of a river channel confluence with discordant beds: Flow turbulence, bed load sediment transport, and bed morphology," *Journal of Geophysical Research: Earth Surface*, vol. 111, no. F4, 2006.
20. G. H. Jirka, *Mixing and dispersion in rivers*. Taylor and Francis, London, 2004.
21. J. M. Gaudet and A. G. Roy, "Effect of bed morphology on flow mixing length at river confluences," *Nature*, vol. 373, no. 6510, pp. 138-139, 1995.
22. E. Mignot, I. Vinkovic, D. Doppler, and N. Riviere, "Mixing layer in open-channel junction flows," *Environmental Fluid Mechanics*, vol. 14, pp. 1027-1041, 2014.
23. G. Weidong and W. X. J. T. Yue, "Research of Hydraulic Characteristics of "Y" shaped Junction," *Hydroelectric Energy*, 2005.
24. G. Weidong, W. Xiaogang, Y. Jiwen, Y. Tianen, and L. Yue, "Research of Hydraulic Characteristics of "Y" shaped Junction," *Water Resour. Power*, vol. 23, pp. 53-56, 2005.
25. B. L. Rhoads and A. N. Sukhodolov, "Field investigation of three-dimensional flow structure at stream confluences: 1. Thermal mixing and time-averaged velocities," *Water resources research*, vol. 37, no. 9, pp. 2393-2410, 2001.
26. T. K. Geberemariam, "Numerical analysis of stormwater flow conditions and separation zone at open-channel junctions," *Journal of Irrigation and Drainage Engineering*, vol. 143, no. 1, p. 05016009, 2017.
27. J. Chabokpour and H. M. Azamathulla, "Numerical simulation of pollution transport and hydrodynamic characteristics through the river confluence using FLOW 3D," *Water Supply*, vol. 22, no. 10, pp. 7821-7832, 2022.
28. K. E. Bencala, "Simulation of solute transport in a mountain pool-and-riffle stream with a kinetic mass transfer model for sorption," *Water Resources Research*, vol. 19, no. 3, pp. 732-738, 1983.
29. A. Marion, M. Zaramella, and A. Bottacin-Busolin, "Solute transport in rivers with multiple storage zones: The STIR model," *Water resources research*, vol. 44, no. 10, 2008.
30. A. Bottacin-Busolin and A. Marion, "Combined role of advective pumping and mechanical dispersion on time scales of bed form–induced hyporheic exchange," *Water Resources Research*, vol. 46, no. 8, 2010.
31. X. Chen, M. B. Cardenas, and L. Chen, "Hyporheic exchange driven by three-dimensional sandy bed forms: Sensitivity to and prediction from bed form geometry," *Water Resources Research*, vol. 54, no. 6, pp. 4131-4149, 2018.
32. V. M. Radu, E. Diacu, M. A. Moncea, F. D. Dumitru, A. M. Panait, and P. Ionescu, "Numerical modelling of pollutant dispersion in the lower Danube River," *Rev Chim Bucharest*, vol. 68, no. 11, pp. 2477-2481, 2017.

33. N. Tantemsapya, W. Wirojanagud, and S. Suwannakom, "Modeling approach to water quality management in the lower Pong river, Thailand," *Warasan Wichai Mokho,* 2008.
34. I. Park and I. W. Seo, "Modeling non-Fickian pollutant mixing in open channel flows using two-dimensional particle dispersion model," *Advances in water resources,* vol. 111, pp. 105-120, 2018.
35. N. Pengpom, S. Vongpradubchai, and P. Rattanadecho, "Numerical Analysis of Pollutant Concentration Dispersion and Convective Flow in a Twodimensional Confluent River Model," *Mathematical Modelling of Engineering Problems,* vol. 6, no. 2, 2019.
36. T. Lyubimova, A. Lepikhin, Y. N. Parshakova, C. Gualtieri, S. Lane, and B. Roux, "Influence of hydrodynamic regimes on mixing of waters of confluent rivers," *Journal of Applied Mechanics and Technical Physics*, vol. 60, pp. 1220-1227, 2019.
37. D. Cheng, J. Song, W. Wang, and G. Zhang, "Influences of riverbed morphology on patterns and magnitudes of hyporheic water exchange within a natural river confluence," *Journal of hydrology*, vol. 574, pp. 75-84, 2019.

© 2024 by the authors. Licensee SCU, Ahvaz, Iran. This article is an open access article distributed under the terms and conditions of the Creative Commons Attribution 4.0 International (CC BY 4.0 license) (http://creativecommons.org/licenses/by/4.0/).

Journal of Hydraulic Structures
J. Hydraul. Struct., 2024;10(3):34-50
DOI: 10.22055/jhs.2024.46669.1293



OPEN ACCESS

Feasibility study of fuzzy method in slope stability analysis of earth dams with respect to the uncertainty of geotechnical parameters

Amin Falamaki [*1]
Amir Hossein Shafiee [2]
Mahdiye Esfandiyari [1]

Abstract

The stability of earth dams is assessed through safety factors, indicating stability if they exceed one. Due to soil property uncertainties, fuzzy logic tools seem suitable for slope stability analysis. Uncertainties in parameters like unit weight, cohesion, and internal friction angle can be encompassed by fuzzy set theory. This study employs fuzzy set theory to analyze slope stability factor of safety, considering the varied materials and soils in earth dams. Information and parameters were gathered, and slopes were modeled using Slide (v. 6) software. Shear strength parameters and safety factors were categorized based on results and expert opinions, defining ranges for each. MATLAB software applied fuzzy logic rules to relate inputs (unit weight, cohesion, friction angle) to the output, factor of safety. Comparing results from probabilistic and fuzzy methods revealed close numerical alignment. The fuzzy method, with adaptable rules accommodating different conditions, yielded quicker and more accurate safety assessments, assuming specific data inputs. Overall, the fuzzy approach offers flexibility, facilitating quicker and more accurate determinations of safety factors, albeit requiring specific data assumptions.

Keywords: Slope Stability; Fuzzy System; Probabilistic Analysis; Fuzzy Rules

Received: 20 April 2024; Accepted: 10 May 2024

1. Introduction

Slope analysis is critical in the process of developing an earth dam. In reality, the slope stability of earth dams is generally assessed using safety factors (FS), and dam slopes are deemed stable if these factors exceed one [1]. However, there is a significant amount of uncertainty in predicting the slope stability. These uncertainties are divided into two categories:

[*] Email: a_falamaki@pnu.ac.ir (**Corresponding Author**)
[1] Department of Civil Engineering, Payame Noor University, P.O. Box 19395-3697, Tehran, Iran.
[2] Department of Civil Engineering, Faculty of Civil Engineering and Architecture, Shahid Chamran University of Ahvaz, Ahvaz, Iran.

those connected with material characteristics and those associated with layer geometry and geotechnical profile [2-4]. Artificial intelligence approaches have been widely employed in recent decades to simulate various geotechnical problems [5-7], owing to their capacity to account for uncertainty. Analyzing the stability of slopes with artificial intelligence methods has also been one of the topics of interest. For example, Khajehzadeh et al. [8] suggested an effective intelligent method based on artificial neural networks (ANN) to estimate the factor of safety of homogeneous slopes under static and dynamic loading. Paliwal et al. [9] also employed an artificial neural network to forecast the stability of a seam and the slope of the remaining soil in the Himalayas.

Among these methods, fuzzy logic method is a very useful and practical method for analyzing complex problems with high uncertainties. Fuzzy systems are a popular technique that can be employed in the geotechnical problems specially in the stability analysis of slopes and earth dams [10]. Fuzzy theory may be used to assess known uncertainties in slope stability evaluation as an alternative to probabilistic approaches. Fuzzy systems employ variables with some uncertainty, which are subsequently used in a constitutive model for every particular material. Fuzzy numbers theory has already been applied to slope stability evaluations in a few works [11-16]. Peng and Huang [14] fully analyzed the safety of earth dams using fuzzy categorization and generated safety assessment indices by analyzing many elements influencing operational and general safety in earth dams. Yang [17] applied fuzzy assessment to determine the safety performance of an earth dam using the analytic hierarchy process (AHP) and concluded that the earth dams might be designed with a combination of natural, social, and economic elements. Lim et al. [18] used three-dimensional analysis to assess slope stability and make recommendations for future evaluations. Fattahi [19] investigated slope stability prediction utilizing soft computing approaches such as the adaptive neuro-fuzzy inference system (ANFIS), which is based on clustering. The results shown that the ANFIS-SCM (subtractive clustering method) model is a valid system modeling approach for predicting slope stability. Haghshenas et al. [20] employed fuzzy multi-criteria decision making (FMCDM) methodologies to assess the importance of each component in dam construction projects. Due of the uncertainty in each factor, they employed a fuzzy inference approach to quantify their likelihood and severity. The outcomes of this analysis indicated that the risk of design faults is the biggest of all the examined hazards.

The purpose of this research is to evaluate the feasibility of the fuzzy method in analyzing the stability of the slope of earth dams with regard to the uncertainty of geotechnical parameters. The reason why the fuzzy method is used in this study is that there are imprecise facts about the limits of the parameters. However, the probabilistic method which is based on a set of random states of parameters and indicates the chance of a particular state cannot be used alone, but in combination with the fuzzy method, they can complement each other and use both methods. Therefore, it is necessary to use a probabilistic method to analyze slope stability so that these two methods complement each other. Since the shear resistance parameters of different materials used in earth dams are very different, a range of these parameters is used to obtain the reliability factor in reality. So, in this research, stable slopes for earth structures like earth dams and embankments are modeled using the fuzzy method. If a suitable method can be found to determine whether the slope is stable or not in this method, it is possible to determine the stability of slopes without the need of modeling and using this theory.

2. Analysis Method

To achieve the objectives of this study, the following actions have been taken:

- ✓ Data collection and gathering of material parameters necessary for analyzing the stability of embankment slopes of an earth dam through literature review and calculation of statistical parameters of the data.
- ✓ Modeling and stability analysis of slope structures using a probabilistic approach in Slide (v. 6) software with varying slopes within the range of material parameters.
- ✓ Investigation of variations in the factor of safety with different parameters.
- ✓ Classification of shear strength parameters and obtained factors of safety from the previous stage analysis using expert opinions, and determination of ranges for each of them.
- ✓ Calculation of statistical parameters for different classifications.
- ✓ Utilization of fuzzy logic method in MATLAB software and definition of rules to relate analysis parameters (input data) to the factor of safety (output data).
- ✓ Comparison of results obtained from the probabilistic model with those obtained from the fuzzy system and determination of the best fuzzy rules and conclusions.

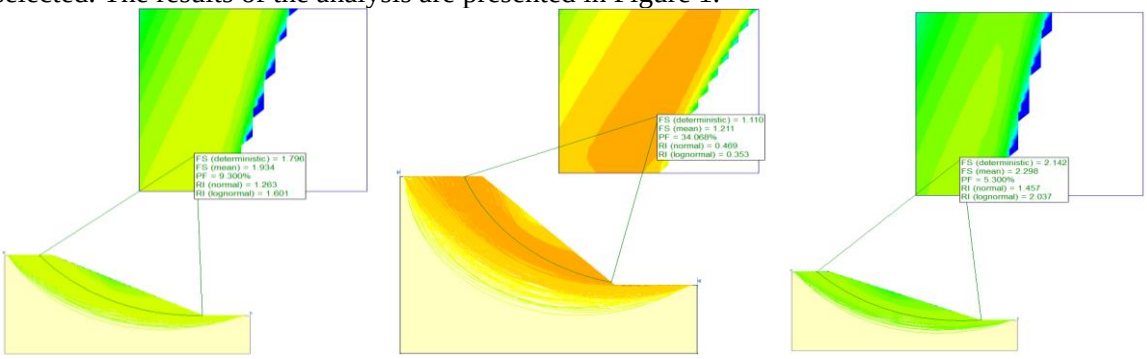
In this study, initially, all the necessary information and parameters, i.e., the cohesion (C), unit weight (γ), and internal friction angle (ϕ), for analyzing the stability of embankment slopes of an earth dam have been collected from various sources, as observed in Table 1.

Table 1. Values of shear strength parameters of materials from literature review

Ingredients	γ (kN/m^3)	C (kN/m^2)	ϕ (deg.)	Reference
Tar Sand	91-94(PCF)	15-37	18-24	[21]
Concrete and Asphalt	14.7-17.8	38-80	39.1-45	[22]
Cohesive Soil and Crushed Concrete	16.77-17.75			[23]
Weak soil and Concrete Aggregate	12.16-14.42			[24]
Concrete and Soil	16.77			[25]
Polypropylene Strips and Lateritic Soils	16.6-17.8	53-54	21.0-32.0	[26]
Substrate (sand, silt and clay) and glass	17.36			[27]
Glass and Subgrade Soil	13.97-16.18			[28]
Glass powder and Subgrade Soil	18-20	42.7-106.4	27.4-43.5	[29]
Fly Ash	15.4-18.14			[30]
Chalk		20-131	30-42.0	[31]
Dumped Rock			35-50	[32]
Rock			20-65.0	[33]
Rockfill			35-52.0	[34]
Rock	25.5	10-50.0		[35]
Rock	20.6			[35]
Rock	23	11.1-117.66	35.69-45.94	[36]
Rock	8.8-23.2			[37]
Gravel Mixtures			32-45.0	[38]
Sand and Gravel Mixtures	15.89-16.28		34-45.0	[38]
Sand and Gravel Mixtures	23	15-59.4	31-67	[39]
Sand and Gravel Mixtures			23.7	[40]
Sand and Gravel Mixtures			32-53	[41]
sand mixtures	15.89		32	[38]
sand mixtures			26.7-27	[40]
sand mixtures	14.47-17.12		18.3-41.6	[42]
sand mixtures	13.6	9.8	13.6-21	[43]
Clay mixtures	11.87	13-98	0-34	[44]
Clay-Gravel Mixture			35-50.0	[45]
Silty Sand			29-37	[46]

The Slide software (v. 6) was utilized for probabilistic stability analysis of slopes. This software enables extensive probabilistic analyses while allowing users to select the type of probabilistic analysis they prefer. Additionally, users have the capability to assign statistical distribution types for each of the input parameters, including material properties, groundwater levels, and loads. Sensitivity analysis in this software allows users to determine the effect of each variable on the factor of safety.

After collecting the desired parameters from each of the available materials, their statistical parameters, including Maximum, Minimum, Average, Median, Variance, and Standard Deviation, were calculated. Then, the slope was modeled in the Slide software. Since the slope is completely heterogeneous, probabilistic slope analysis was performed in the Slide software. For this purpose, the GLE/Morgenstern method was used for probabilistic analysis as it considers both the force equilibrium and moment equilibrium in analysis and design, which is the best method. However, other methods such as Bishop and Janbu do not consider both of these equilibrium states in their analysis. The slip surface was considered circular, the search method was set to Grid Search, the design option was selected as Statistic, Monte Carlo sampling method was used, and 1000 samples were chosen by default. The analysis was performed on three different slopes: 1 to 1, 1 to 2, and 1 to 2.5, with a constant slope height of 80 meters. Then, the relative minimum and maximum values, mean, and standard deviation for the cohesion (C), unit weight (γ), and internal friction angle (ϕ) parameters, which had been previously calculated, were defined as parameters with uncertainty, and the normal distribution curve was selected. The results of the analysis are presented in Figure 1.



Slope 1 to 1 **Slope 1 to 2** **Slope 1 to 2.5**

Figure 1. Results of modeling and probabilistic analysis of different slopes using Slide

In Table 2, the results of the analysis are also provided. According to the results obtained from the analysis of the three slopes in Table 2, slopes 1 to 2 and 1 to 2.5 are completely stable and have high factors of safety. Therefore, slope 1 to 1, which has lower factors of safety and is closer to 1, is considered as the critical slope for design purposes.

Table 2. summarizes the results of modeling with different slopes.

Slope	FS (deterministic)	FS (mean)	PF %	RI (normal)	RI (lognormal)
1:1	1.11	1.211	34.068	0.469	0.353
1:2	1.796	1.934	9.3	1.263	1.601
1:2.5	2.142	2.298	5.3	1.457	2.037

FS (deterministic): The deterministic factor of safety of the slope obtained from conventional analysis with inputting average parameters.
FS (mean): The probabilistic stability factor of the slope obtained from probabilistic analysis.
PF: The percentage of failed samples to the total number of samples.
RI: Reliability index (for normal distribution, represents the number of standard deviations that separate the mean Factor of Safety, from the critical Factor of Safety (= 1).

Following that, a scatter plot for each of the unknown parameters relative to the factor of safety was plotted, and the data for each output were extracted from Excel to compare the factors of safety for all samples for each of the unit weight, cohesion, and friction angle parameters. Since the factors of safety for parameters were the same in each sample, it was concluded that the parameter values simultaneously and in conjunction with other parameters provided a consistent factor of safety. For example, for the first sample, the factor of safety for all cohesion, friction angle, and unit weight parameters was 0.146, and similarly, the factors of safety for these three parameters were the same for other samples. Therefore, 1000 samples obtained from the probabilistic scenarios provided by the software were considered as real-life samples.

Taking into account real conditions, experiences, and consulting experts, the factor of safety was divided into three categories. The considered categories for the factor of safety were as follows: The first category included factors of safety less than 1, indicating instability (F). The second category included factors of safety greater than 1 and less than 1.5, suggesting potential stability (PS). The third category included factors of safety greater than 1.5, indicating definite stability (S). Based on these three categories, the unit weight, cohesion, and friction angle parameters were also divided into three categories within these ranges, considering low (L), medium (M), and high (H) states for each.

The maximum, minimum, mean, and median values for each parameter category were calculated and are presented in Table 3. Additionally, scatter plots were created for each parameter within each category to facilitate analysis. The scatter plot depicting cohesion versus factor of safety is presented in Figure 2, the plot for friction angle versus factor of safety is displayed in Figure 3, and the plot illustrating unit weight versus factor of safety is shown in Figure 4.

Table 3. Statistical values of the classified shear strength parameters of samples

Parameter		**1< FS**	**FS < 1.5≤1**	**FS ≥ 1.5**
C (kN/m^2)	Median	32.65	54.58	67.93
	Average	34.88	55.32	69.59
	Min	0.06	0.41	1.07
	Max	97.24	170.07	143.53
ϕ (deg.)	Median	20.99	33.2	44.85
	Average	20.62	32.67	43.81
	Min	0.72	11.49	19.46
	Max	36.56	49.01	57.34
γ (kN/m^3)	Median	16.9	16.97	15.93
	Average	16.89	17.04	16.11
	Min	11.95	12.12	11.91
	Max	24.46	24.25	23.69
FS	Median	0.76	1.24	1.73

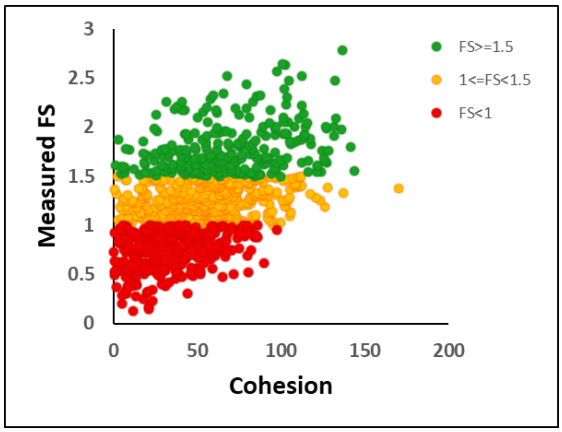


Figure 2. The values of the obtained safety factors based on samples with different cohesions

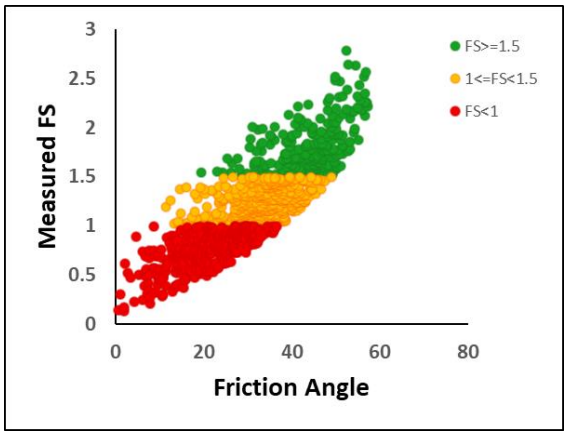


Figure 3. The values of the obtained safety factors based on samples with different friction angles

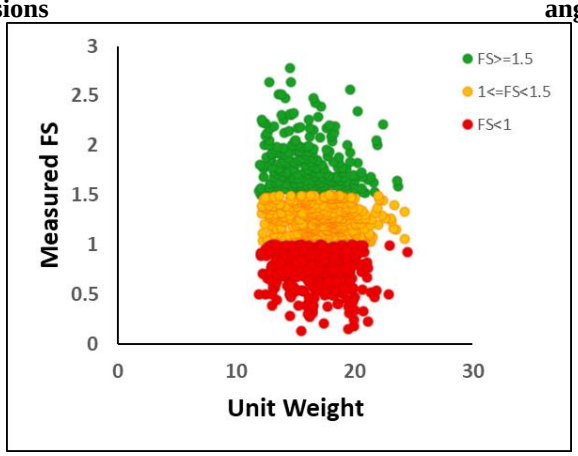


Figure 4. The values of the obtained safety factors based on samples with different unit weights

As observed in Figure 4, the variations in unit weight were nearly constant across all three categories. Therefore, only one average condition for unit weight was considered. However, in the cohesion and friction angle plots, as expected, it was observed that with an increase in these parameters, the safety factor also increased. Nevertheless, many values in these categories overlapped with each other. This implies that, for instance, a range of values from the first category, yielding safety factors less than 1, might also fall within the second or third category, where their safety factors are greater than 1 or 1.5, respectively. In such situations, analyzing the safety factor becomes challenging because it's not clear which specific cohesion, unit weight, or friction angle value may result in what safety factor. In these circumstances, fuzzy logic theory is highly applicable and provides an appropriate solution. These overlaps and uncertain boundaries essentially embody the concept of fuzzy logic, which has been introduced for handling uncertain boundaries and ambiguous parameters.

2.1. Fuzzy Stability Analysis

To utilize fuzzy theory, MATLAB software is necessary. The fuzzy system comprises inputs, rules, and outputs. Here, the inputs include unit weight, cohesion, and friction angle, while the output is the factor of safety. The considered ranges are explained further in Table 4.

Table 4. Information of the defined fuzzy system for models

Input	C (kN/m^2)	L	Type	trapmf
		M	Type	trimf
		H	Type	trapmf
	ϕ (deg.)	L	Type	trapmf
		M	Type	trimf
		H	Type	trapmf
	γ (kN/m^3)	M	Type	trimf
Output	FS	F	Type	trapmf
		PS	Type	trimf
		S	Type	trapmf
Methods	And method			min
	Or method			max
	Implication			min
	Aggregation			max
	Defuzzification			centroid

trapmf = Trapezoidal membership function
trimf = Triangular membership function
L=low, M = medium and H =high
F = instability
PS = potential stability
S = definite stability

The ranges for each category were selected based on the scatter plots from Figures 2 to 4. To do this, scattered points were disregarded, and boundary points for each category were considered to define its range. In these circumstances, some points also overlapped with other categories. The membership degree of each point to each category, indicating the extent to which it belongs to that category, was determined using fuzzy membership functions. A fuzzy inference system (FIS) consists of 6 stages, which are:

1. Input Data: In this stage, the input parameters such as unit weight, cohesion, and friction angle, which have been predetermined, are specified as input parameters.
2. Fuzzification: In this stage, a specific function is determined for each parameter, and the ranges considered for the functions are also indicated on the graph. In this part, the membership degree of the input functions is determined. Among the functions that are most commonly used are triangular, trapezoidal, Gaussian, sigmoidal, π-shaped, and S-shaped.
3. Implication: In this stage, using a set of rules, we relate the input data to the output data. To define these rules, past experiences, expert opinions, and comparison with actual results are utilized. If necessary, adjustments to the rules can be made to reduce errors, ensuring that fuzzy analysis results closely match real-world outcomes. Conditions can be defined using "and" and "or" operators between sentences. The "and" operator (fuzzy intersection), also known as "T-norm," has several methods, including "min" and "prod," which consider the minimum and product of states, respectively. Similarly, the "or" operator (fuzzy union), also known as "S-norm," has two methods: "max" and "probor," which consider the maximum value and the probabilistic sum of functions, respectively. The Implication method itself can also have two modes: one using the minimum value and the other using the product of functions.
4. Aggregation: In this stage, the outputs of all rules are combined with each other to form a composite fuzzy set. Aggregation of output functions is also performed using various

methods, including "max," "sum," and "probor," which respectively consider the maximum value, sum, and probabilistic sum of functions.

5. Defuzzification: Using specific methods, the fuzzy output function obtained from the previous stage, which is in the form of a fuzzy graph and lacks a clear concept, can be transformed into a definite non-fuzzy number. Some of the most important methods for defuzzifying the output function includes centroid method, median, mean of maximum, maximum value, and minimum of maximum value. However, besides these, other functions can also be defined and used.
6. Output: The numerical value obtained after defuzzification provides a degree of membership from the output functions based on the defined conditions and selected methods, which essentially represents the required confidence level.

In this study, various scenarios for each of these methods and conditions were considered. Many scenarios were discarded due to significant discrepancies with the original results obtained from slope stability analysis in the Slide software, and only six scenarios with results close to each other were investigated and compared.

Conditions Considered in the Fuzzy System

The functions chosen for this study were triangular and trapezoidal functions. The reason for selecting these two functions is their wide applicability, ease of use, and the possibility of selecting the ranges of functions. Although using curved functions such as Gaussian and bell-shaped curves might potentially provide higher accuracy if the curves are considered symmetrically, any change in one side of the curve would affect the other side, making the selected functions asymmetric. Therefore, it would be challenging to determine the desired range accurately. In Figure 5, the components of the fuzzy system and parameters are specified.

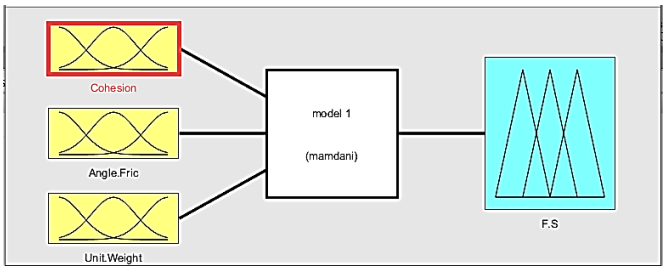
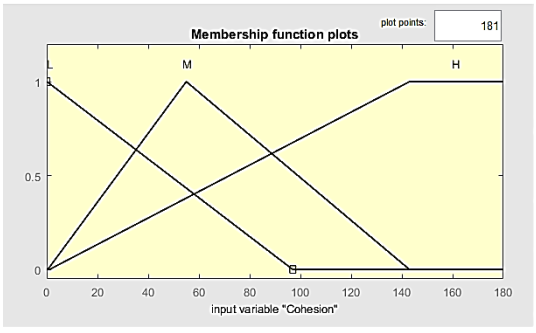
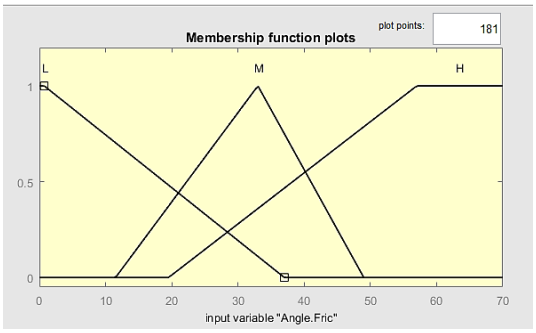


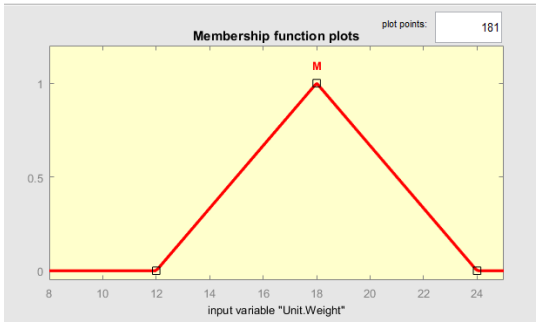
Figure 5. Parameters defined for the fuzzy system



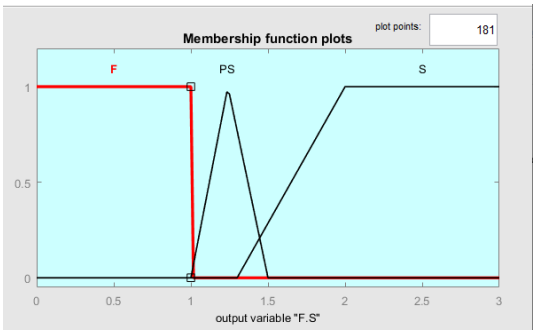
(a)



(b)



(c)



(d)

Figure 6. Functions and Parameter Ranges for (a) Cohesion, (b) Internal Friction Angle, (c) Unit Weight and (d) Factor of Safety

In Figure 6, the selected functions and the considered ranges for each function have been specified. The membership degree of each parameter can be determined in these functions. In this way, the y-axis represents the membership degree function from 0 to 1, while the x-axis denotes the range of the data. As previously mentioned, the selection of the ranges for each category is based on the obtained graphs from Figures 2 to 4, adjusted from the initial data. In triangular functions, the apex of the triangle represents the mean parameter value in that category. Additionally, the points to the left and right of each category represent the minimum and maximum parameter values in that category, respectively. As observed, the membership degree of values before the mean increases until it reaches a membership degree of 1, then decreases after the mean until it reaches 0. Points between two categories have a membership degree in both categories, decreasing in one category and increasing in the other. It is also possible for the membership degree in both categories to be 0.5. In the categories with the highest values, a triangular function with infinite properties is typically used. This means that if the parameter value exceeds a certain limit, its membership in that category will be complete, with a membership degree of 1. This condition implies that the infinite triangular function can also be used for the low (L) state, meaning that even for values below a certain threshold, its membership in this category will be 1. For the conditions and rules of the fuzzy system, attempts and errors were made in ranges close to reality, and ultimately, the combination of these conditions, which had less error compared to others, was selected.

Table 5. The range of each function defined for the models

I/O	Parameter	Function type	Model 1	Model 2	Model 3	Model 4	Model 5	Model 6
Input	C (kN/m^2) Fig. 6(a)	L = trapmf	[-inf -inf 0.06 97]	[-inf -inf 0.06 97]	[-inf -inf 0.06 97]	[-inf -inf 0.06 97]	[-inf -inf 0.06 97]	[-inf -inf 0.06 97]
		M = trimf	[0.4 55 143]	[0.41 55.32 170]	[0.41 55.32 170]	[0.41 55.32 170]	[0.41 55.32 170]	[0.41 55.32 170]
		H = trapmf	[1 143 inf inf]	[1.07 143 inf inf]	[1.07 143 inf inf]	[1.07 143 inf inf]	[1.07 143 inf inf]	[1.07 143 inf inf]
	ϕ (deg.) Fig. 6(b)	L = trapmf	[-inf -inf 0.72 37]	[-inf -inf 0.72 36.56]	[-inf -inf 0.72 36.56]	[-inf -inf 0.72 36.56]	[-inf -inf 0.72 36.56]	[-inf -inf 0.72 36.56]
		M= trimf	[11.5 33 49]	[11.5 32.67 49]	[11.5 32.67 49]	[11.5 32.67 49]	[11.5 32.67 49]	[11.5 32.67 49]
		H = trapmf	[19.5 57 inf inf]	[19.46 57.34 inf inf]	[19.46 57.34 inf inf]	[19.46 57.34 inf inf]	[19.46 57.34 inf inf]	[19.46 57.34 inf inf]
	γ (kN/m^3) Fig. 6(c)	M = trimf	[12 18 24]	[11.91 16.68 24.46]	[11.91 12.12 23.69 24.46]	[11.91 12.12 23.69 24.46]	[11.91 12.12 23.69 24.46]	[11.91 12.12 23.69 24.46]
Output	FS Fig. 6(d)	F = trapmf	[-inf -inf 1 1]	[-inf -inf 1 1.1]	[-inf -inf 1 1.1]	[-inf -inf 1 1.1]	[-inf -inf 1 1.1]	[-inf -inf 1 1.1]
		PS = trimf	[1 1.24 1.5]	[1 1.24 1.5]	[1 1.24 1.5]	[1 1.24 1.5]	[1 1.24 1.5]	[1 1.24 1.5]
		S = trapmf	[1.3 2 inf inf]	[1.3 2 inf inf]	[1.3 2 inf inf]	[1.3 2 inf inf]	[1.3 2 inf inf]	[1.3 2 inf inf]

After several trials and errors, six models were chosen, which had similar results and were better than other analyses. Tables 5 and 6 provide information on the methods, rules applied, and changes made in the six fuzzy analyses performed.

Table 6. Defined rules for models

Model	Rule No.	Rules	Model	Rules
	1	If (C is L) and (ϕ is L) and (γ is M) then (FS is F)		If (C is L) and (ϕ is L) and (γ is M) then (FS is F)
	2	If (C is L) and (ϕ is M) and (γ is M) then (FS is F)		If (C is L) and (ϕ is M) and (γ is M) then (FS is F)
	3	If (C is L) and (ϕ is H) and (γ is M) then (FS is PS)		If (C is L) and (ϕ is H) and (γ is M) then (FS is PS)
	4	If (C is M) and (ϕ is L) and (γ is M) then (FS is F)		If (C is M) and (ϕ is L) and (γ is M) then (FS is PS)
1	5	If (C is M) and (ϕ is M) and (γ is M) then (FS is F)	4	If (C is M) and (ϕ is M) and (γ is M) then (FS is PS)
	6	If (C is M) and (ϕ is H) and (γ is M) then (FS is PS)		If (C is M) and (ϕ is H) and (γ is M) then (FS is PS)
	7	If (C is H) and (ϕ is L) and (γ is M) then (FS is PS)		If (C is H) and (ϕ is L) and (γ is M) then (FS is PS)
	8	If (C is H) and (ϕ is M) and (γ is M) then (FS is PS)		If (C is H) and (ϕ is M) and (γ is M) then (FS is PS)
	9	If (C is H) and (ϕ is H and (γ is M) then (FS is S)		If (C is H) and (ϕ is H and (γ is M) then (FS is S)
	1	If (C is L) and (ϕ is L) and (γ is M) then (FS is F)		If (C is L) and (ϕ is L) and (γ is M) then (FS is F)
	2	If (C is L) and (ϕ is M) and (γ is M) then (FS is F)		If (C is L) and (ϕ is M) and (γ is M) then (FS is F)
	3	If (C is L) and (ϕ is H) and (γ is M) then (FS is PS)		If (C is L) and (ϕ is H) and (γ is M) then (FS is PS)
	4	If (C is M) and (ϕ is L) and (γ is M) then (FS is F)		If (C is M) and (ϕ is L) and (γ is M) then (FS is PS)
2	5	If (C is M) and (ϕ is M) and (γ is M) then (FS is PS)	5	If (C is M) and (ϕ is M) and (γ is M) then (FS is PS)
	6	If (C is M) and (ϕ is H) and (γ is M) then (FS is S)		If (C is M) and (ϕ is H) and (γ is M) then (FS is PS)
	7	If (C is H) and (ϕ is L) and (γ is M) then (FS is PS)		If (C is H) and (ϕ is L) and (γ is M) then (FS is PS)
	8	If (C is H) and (ϕ is M) and (γ is M) then (FS is S)		If (C is H) and (ϕ is M) and (γ is M) then (FS is PS)
	9	If (C is H) and (ϕ is H and (γ is M) then (FS is S)		If (C is H) and (ϕ is H and (γ is M) then (FS is S)
	1	If (C is L) and (ϕ is L) and (γ is M) then (FS is F)		If (C is L) and (ϕ is L) and (γ is M) then (FS is F)
	2	If (C is L) and (ϕ is M) and (γ is M) then (FS is F)		If (C is L) and (ϕ is M) and (γ is M) then (FS is F)
	3	If (C is L) and (ϕ is H) and (γ is M) then (FS is PS)		If (C is L) and (ϕ is H) and (γ is M) then (FS is PS)
	4	If (C is M) and (ϕ is L) and (γ is M) then (FS is PS)		If (C is M) and (ϕ is L) and (γ is M) then (FS is PS)
3	5	If (C is M) and (ϕ is M) and (γ is M) then (FS is PS)	6	If (C is M) and (ϕ is M) and (γ is M) then (FS is PS)
	6	If (C is M) and (ϕ is H) and (γ is M) then (FS is PS)		If (C is M) and (ϕ is H) and (γ is M) then (FS is PS)
	7	If (C is H) and (ϕ is L) and (γ is M) then (FS is PS)		If (C is H) and (ϕ is L) and (γ is M) then (FS is PS)
	8	If (C is H) and (ϕ is M) and (γ is M) then (FS is PS)		If (C is H) and (ϕ is M) and (γ is M) then (FS is PS)
	9	If (C is H) and (ϕ is H and (γ is M) then (FS is S)		If (C is H) and (ϕ is H and (γ is M) then (FS is S)

3. Analysis of Results

Figure 7 compares the factor of safety obtained from the fuzzy analyses with the estimated and initial factor of safety. Statistical parameters were utilized for a more accurate comparison. These parameters include:

- RMSE (Root Mean Square Error): The square root of the mean of the squared differences between estimated and simulated values, providing an indication of the typical deviation.
- CD (Coefficient of Determination): Indicates the proportion of the variance in the simulated values that is predictable from the estimated values.
- EF (Modeling Efficiency): Measures the efficiency of the modeling process.
- CRM (Coefficient of Residual Mass): Measures the remaining mass coefficient.
- SE (Standard Error): Measures the typical deviation of the estimated values from the simulated values.
- RE (Relative Error): Indicates the relative deviation between estimated and simulated values.
- COREE (Correlation): Also known as the correlation coefficient (r), measures the strength and direction of the linear relationship between estimated and simulated values.

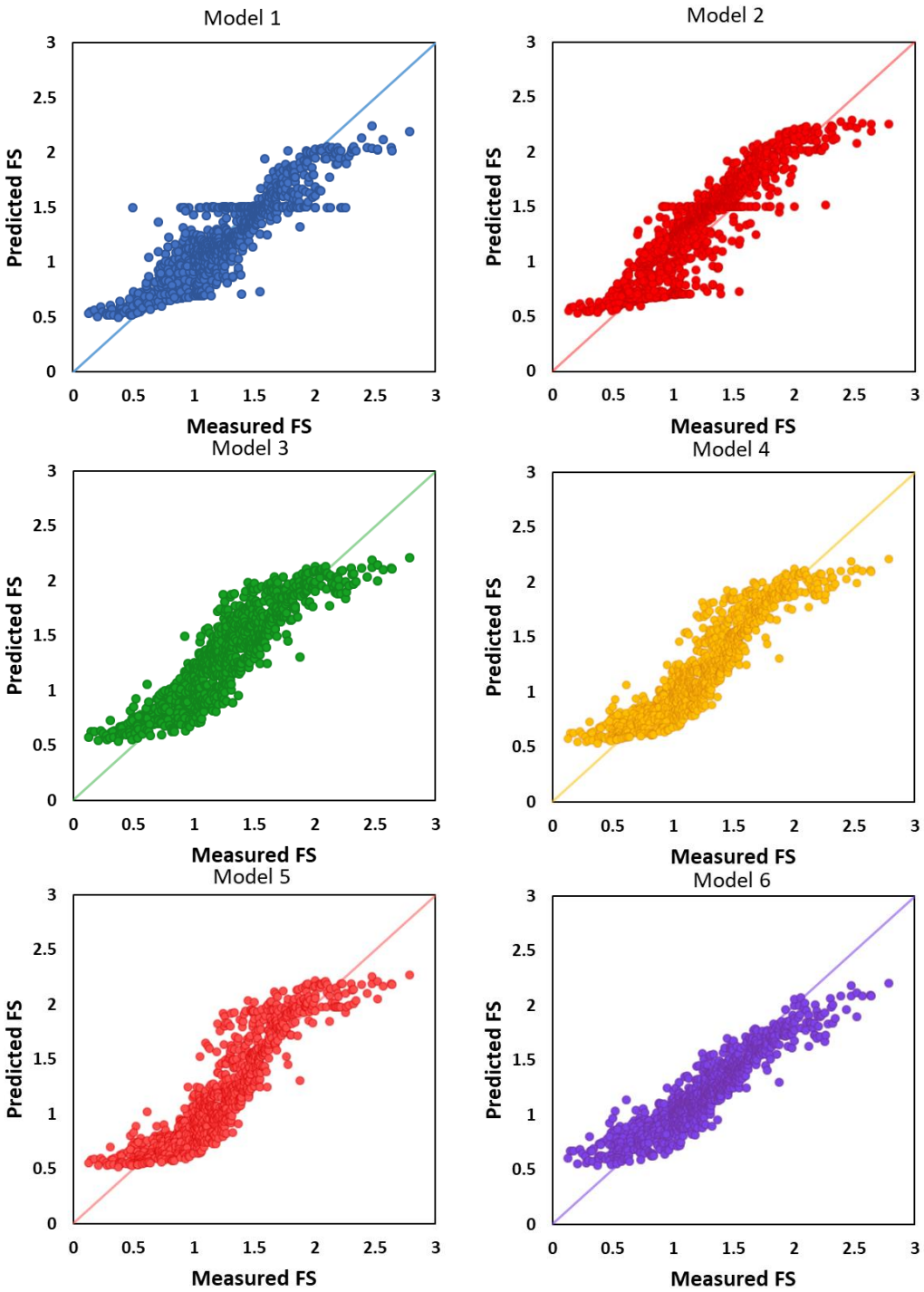


Figure 7. Comparison of Estimated and Simulated Factor of Safety in Different Models

$$\mathrm{RMSE} = \left[\frac{\sum_{i=1}^{n}(S_i - M_i)^2}{n}\right]^{\frac{1}{2}} \frac{100}{\bar{M}} \quad (1)$$

$$\mathrm{CD} = \frac{\sum_{i=1}^{n}(M_i - \bar{M})^2}{\sum_{i=1}^{n}(S_i - \bar{M})^2} \quad (2)$$

$$\mathrm{EF} = \frac{\sum_{i=1}^{n}(M_i - \bar{M})^2 - \sum_{i=1}^{n}(S_i - M_i)^2}{\sum_{i=1}^{n}(M_i - \bar{M})^2} = 1 - \frac{\sum_{i=1}^{n}(S_i - M_i)^2}{\sum_{i=1}^{n}(M_i - \bar{M})^2} \quad (3)$$

$$\mathrm{CRM} = \frac{\sum_{i=1}^{n} M_i - \sum_{i=1}^{n} S_i}{\sum_{i=1}^{n} M_i} \quad (4)$$

$$\mathrm{SE} = \sqrt{\frac{1}{n-2}\left[\sum_{i=1}^{n}(M_i - \bar{M})^2 - \frac{[\sum_{i=1}^{n}(S_i - \bar{S})(M_i - \bar{M})]^2}{\sum_{i=1}^{n}(S_i - \bar{S})}\right]} \quad (5)$$

$$\mathrm{RE} = \left|\frac{M_i - S_i}{M_i}\right| \times 100 \quad (6)$$

$$\mathrm{R} = \frac{n(\sum_{i=1}^{n}(P_i)(O_i)) - (\sum_{i=1}^{n} P_i)(\sum_{i=1}^{n} O_i)}{\sqrt{n\left[\sum_{i=1}^{n}(P_i)^2 - (\sum_{i=1}^{n}(P_i))^2\right]\left[n\sum_{i=1}^{n}(O_i)^2 - (\sum_{i=1}^{n}(O_i))^2\right]}} \ , -1 \le r \le 1 \quad (7)$$

In the aforementioned equations, S_i and M_i denote the simulated and measured values, respectively. $\bar{S}$ and $\bar{M}$ represent the mean of the simulated and measured values, respectively, while n denotes the sample size. Zarei et al. [47] explained the characteristics of these parameters. The minimum value for Mean Error (ME), Root Mean Square Error (RMSE), and Coefficient of Determination (CD) may be equal to zero, while the maximum value for Efficiency Factor (EF) could be one. EF and Correlation Ratio Measure (CRM) may assume values less than zero. A higher RMSE value indicates the accuracy of simulations (whether overestimation or underestimation is present). The CD statistic signifies the relationship between the scatter of simulated values and measurements. EF compares the simulated values with the average of measured values. A negative EF value implies that the average of measured values offers a superior estimate compared to the simulated values. CRM gauges the model's inclination to overfit or underfit the measurements. A negative CRM indicates a propensity to overfit. When all simulated and measured data are identical, the resultant statistics are as follows: ME = 0; RMSE = 0; CD = 1; EF = 1; CRM = 0 [48]. The statistical outcomes derived from the six models are illustrated in Figure 8.

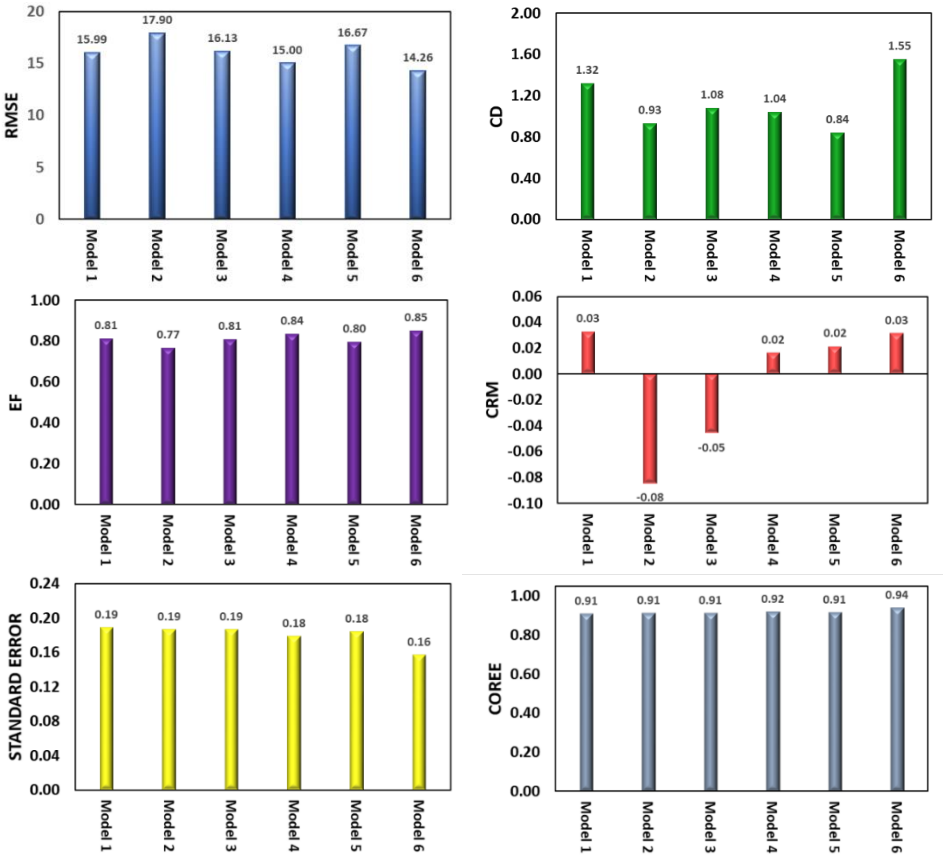


Figure 8. Comparison of statistical parameters for different models.

For a better understanding of each model's behavior, the percentage of data points with relative errors (RE) less than 10, 20, 50, and 100% is counted and shown in Figure 9. Essentially, the higher the percentage of data points with lower REs, the better the model. For example, RE less than 10% indicates an error of less than 10%. The higher the number of data points with errors less than 10% in a model, the more practical and accurate that model is.

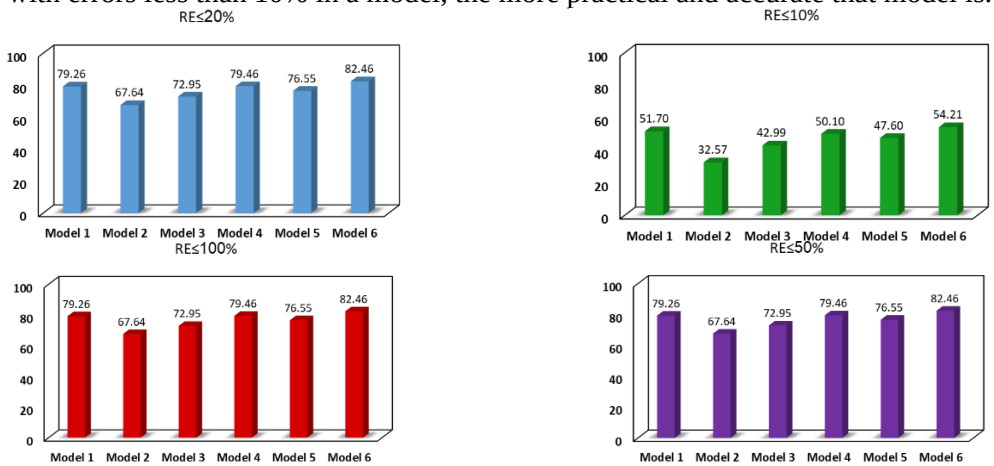


Figure 9. Comparative plots of parameters with RE less than a certain value (%) for different models

In Table 7, all statistical parameters along with their comparison are provided side by side. The best models, in order, are Model 6, Model 4, Model 3, Model 5, Model 1, and Model 2.

Table 7. Comparison of all statistical parameters obtained from the conducted analyses

Parameters	RMSE	CD	EF	CRM	Standard err	COREE	RE≤10%
Model 1	15.99	1.32	0.81	0.03	0.19	0.91	51.70
Model 2	17.90	0.93	0.77	-0.08	0.19	0.91	32.57
Model 3	16.13	1.08	0.81	-0.05	0.19	0.91	42.99
Model 4	15.00	1.04	0.84	0.02	0.18	0.92	50.10
Model 5	16.67	0.84	0.80	0.02	0.18	0.91	47.60
Model 6	14.26	1.55	0.85	0.03	0.16	0.94	54.21

4. Conclusions

Feasibility of the fuzzy method in analyzing the stability of soil slopes was investigated considering the uncertainty of geotechnical parameters. The factor of safety of the slope was evaluated using two methods. The first method involved slope analysis and design in Slide software, where the factors of safety were obtained for 1000 samples using statistical and real data of materials in a soil dam. In this method, three slopes, namely 1:1, 1:2, and 1:2.5, with a constant height of 80 meters were considered, among which slopes with ratios of 1:2 and 1:2.5 were completely stable, while the 1:1 slope exhibited critical conditions. In this scenario, the slope was modeled using probabilistic methods, and the results obtained were extracted as output. The second method aimed at finding the factor of safety in MATLAB software through fuzzy theory, where the slope itself was not modeled. Instead, factors of safety were derived using fuzzy rule definitions and input parameters (i.e., cohesion, internal friction angle, and soil unit weight) to obtain the output results (real factors of safety). Various scenarios were considered for the fuzzy method, many of which were eliminated due to high error rates, and only six scenarios that yielded the best results and were close to each other were selected. Different assumptions were made for these six analyses. Subsequently, statistical equations were employed to compare the six models.

The results of comparing the statistical parameters are summarized in Table 7. Ultimately, by comparing the models, it was concluded that Model 6 (with the assumptions specified for this model in Tables 5 and 6) had the closest values to the real factors of safety and the least error compared to other models, demonstrating better performance. The efficiency of this model is 85%, with a standard error of 16%, which is the lowest error compared to the others. The findings of this study confirm the applicability of the fuzzy method in slope stability analysis. A limitation of this study lies in its exclusive analysis of slopes under dry conditions, without accounting for fluctuations in groundwater levels. Consequently, it is essential to evaluate the method's efficacy across various underground water and drainage scenarios.

References

1. Belazouz L, Bouzelha K, Hammoum H, Amiri O, Khelil N (2024) Reliability Analysis of the Slope Stability of Homogeneous Earth Dam under Seismic Loading. Periodica Polytechnica Civil Engineering 68 (1):107-121
2. Falamaki A, Eskandari M, Khodayari S, Forouzeshfar I, Ghaedsharaf A, Baneshi Z (2019) Laboratory simulation of aeration on municipal solid waste from Barmshoor Landfill. International Journal of Civil Engineering 17:897-906

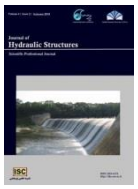
3. Falamaki A, Shafiee A, Shafiee AH (2021) Under and post-construction probabilistic static and seismic slope stability analysis of Barmshour Landfill, Shiraz City, Iran. Bulletin of Engineering Geology and the Environment 80 (7):5451-5465
4. Shafiee AH, Falamaki A, Shafiee A, Arjmand F (2022) Probabilistic analysis of an 80,000 m2 landslide in Shiraz, Iran. Landslides 19 (3):659-671
5. Falamaki A, Eskandari M (2013) Using multi criteria decision making approach for municipal solid waste landfill siting in Yasouj. Iran Occupational Health 10 (5):44-55
6. Falamaki A, Shahin S (2019) Determination of shear strength parameters of municipal solid waste from its physical properties. Iranian Journal of Science and Technology, Transactions of Civil Engineering 43:193-201
7. Karimpour-Fard M, Machado SL, Falamaki A, Carvalho MF, Tizpa P (2019) Prediction of compaction characteristics of soils from index test's results. Iranian Journal of Science and Technology, Transactions of Civil Engineering 43:231-248
8. Khajehzadeh M, Taha MR, Keawsawasvong S, Mirzaei H, Jebeli M (2022) An effective artificial intelligence approach for slope stability evaluation. Ieee Access 10:5660-5671
9. Paliwal M, Goswami H, Ray A, Bharati AK, Rai R, Khandelwal M (2022) Stability prediction of residual soil and rock slope using artificial neural network. Advances in Civil Engineering 2022
10. Mohammadi M, Ershadi MJ, Kamyab H (2024) Assessment of stability of earth dams based on construction pace by fuzzy inference logic. Dams and Reservoirs:1-10
11. Dodagoudar G, Venkatachalam G (2000) Reliability analysis of slopes using fuzzy sets theory. Computers and Geotechnics 27 (2):101-115
12. MEYDANI M, Habibaghai G, KATEBI S (2004) An aggregated fuzzy reliability index for slope stability analysis.
13. Silva M (2008) Application of Fuzzy Logic to the Prediction of Risk in Slope Sliding of Residual Soil. Master's Dissertation (In Portuguese), Center of Technology and Sciences
14. Peng H, Huang Y-x The comprehensive safety assessment of earthfill dam based on multi-stratum fuzzy evaluation. In: 2009 Second International Symposium on Computational Intelligence and Design, 2009. IEEE, pp 218-222
15. Khademi Hamidi J, Shahriar K, Rezai B, Bejari H (2010) Application of fuzzy set theory to rock engineering classification systems: an illustration of the rock mass excavability index. Rock mechanics and rock engineering 43:335-350
16. Hosseini N, Gholinejad M (2014) Investigating the slope stability based on uncertainty by using fuzzy possibility theory. Archives of Mining Sciences 59 (1):179-188
17. Yang HN (2012) The application of fuzzy evaluation method to assess safety behavior of xixia reservoir earthfill dam. Applied Mechanics and Materials 212:934-941
18. Lim K, Li A-J, Lyamin A (2015) Three-dimensional slope stability assessment of two-layered undrained clay. Computers and Geotechnics 70:1-17
19. Fattahi H (2017) Prediction of slope stability using adaptive neuro-fuzzy inference system based on clustering methods. Journal of Mining and Environment 8 (2):163-177

20. Haghshenas SS, Neshaei MAL, Pourkazem P, Haghshenas SS (2016) The risk assessment of dam construction projects using fuzzy TOPSIS (case study: Alavian Earth Dam). Civil Engineering Journal 2 (4):158-167
21. Ola S (1991) Geotechnical properties and behaviour of Nigerian tar sand. Engineering geology 30 (3-4):325-336
22. Zedan AJ, Hummadi RA, Hussein SA (2019) Effect of adding mixture of (concrete waste and asphalt waste) on the properties of gypseous soil. Tikrit Journal of Engineering Sciences 26 (1):20-25
23. Karkush MO, Yassin S (2019) Improvement of geotechnical properties of cohesive soil using crushed concrete. Civil Engineering Journal 5 (10):2110-2119
24. Paul H, Cyrus S Stabilization of weak subgrade soil using demolished concrete aggregate. In: Indian Geotech Conference IGC, 2016. vol 1. pp 93-105
25. Rahardjo H, Gofar N, Satyanaga A (2018) Effect of concrete waste particles on infiltration characteristics of soil. Environmental earth sciences 77:1-12
26. Nsaif MH (2013) Behavior of soils strengthened by plastic waste materials. Journal of Engineering and Sustainable Development 17 (4):182-194
27. Mahdi Z, Al-Hassnawi NS (2018) Assessment of subgrade soil improvement by waste glass powder. International Journal of Civil Engineering and Technology 9 (10):12-21
28. Lingwanda MI (2018) Use of waste glass in improving subgrade soil properties. International Journal of Research in Engineering and Technology 7 (04):28-32
29. Javed SA, Chakraborty S (2020) Effects of waste glass powder on subgrade soil improvement. World Scientific News (144):30-42
30. Sharma R (2020) Utilization of fly ash and waste ceramic in improving characteristics of clayey soil: a laboratory study. Geotechnical and Geological Engineering 38 (5):5327-5340
31. Bundy SP (2013) Geotechnical properties of chalk putties. University of Portsmouth Portsmouth, UK,
32. Barton N Shear strength of rockfill, interfaces and rock joints, and their points of contact in rock dump design. In: Rock dumps 2008: proceedings of the first international seminar on the management of rock dumps, stockpiles and heap leach pads, 2008. Australian Centre for Geomechanics, pp 3-17
33. ELIASI M (2005) Determination of rock-mass internal friction on the basis of shear plane bearing slickenside lineation.
34. Frossard E, Hu W, Dano C, Hicher P-Y (2012) Rockfill shear strength evaluation: a rational method based on size effects. Géotechnique 62 (5):415-427
35. Meng Q, Hodgetts D (2019) Combined control of décollement layer thickness and cover rock cohesion on structural styles and evolution of fold belts: A discrete element modelling study. Tectonophysics 757:58-67
36. Shen J, Shu Z, Cai M, Du S (2020) A shear strength model for anisotropic blocky rock masses with persistent joints. International Journal of Rock Mechanics and Mining Sciences 134:104430

37. Kilic R, Yavuz S (1994) Relationships between geotechnical properties of the Antalya travertine (Turkey). Bulletin of Engineering Geology & the Environment 50 (1)
38. Yagiz S (2001) Brief note on the influence of shape and percentage of gravel on the shear strength of sand and gravel mixtures. Bulletin of Engineering Geology and the Environment 60:321-323
39. Chang K-T, Cheng M-C (2014) Estimation of the shear strength of gravel deposits based on field investigated geological factors. Engineering geology 171:70-80
40. Chang W-J, Phantachang T (2016) Effects of gravel content on shear resistance of gravelly soils. Engineering Geology 207:78-90
41. Simoni A, Houlsby GT (2006) The direct shear strength and dilatancy of sand–gravel mixtures. Geotechnical & Geological Engineering 24:523-549
42. Mamo B, Banoth K, Dey A Effect of strain rate on shear strength parameter of sand. In: Proceedings of the 50th Indian geotechnical conference, Pune, India, 2015.
43. Hooshyar A, Rostami V (2018) Granular Soil Bearing Capacity Improvement Using Waste Plastic Materials. Amirkabir Journal of Civil Engineering 50 (4):755-764
44. Babakhani P, Rahimi E, Gharavi H, Motahari M, Rastegarnia A (2020) Determining of cohesion and internal friction angle of low-plasticity clays (CL) soils using SPT number and investigating the effect of lime on compressive strength of clay soil. New Findings in Applied Geology 14 (28):129-149
45. Li Y, Huang R, Chan LS, Chen J (2013) Effects of particle shape on shear strength of clay-gravel mixture. KSCE Journal of Civil Engineering 17:712-717
46. Salgado R, Bandini P, Karim A (2000) Shear strength and stiffness of silty sand. Journal of geotechnical and geoenvironmental engineering 126 (5):451-462
47. Zarei G, Homaee M, Liaghat A (2009) Modeling transient evaporation from descending shallow groundwater table based on Brooks–Corey retention function. Water Resources Management 23:2867-2876
48. Falamaki A, Eskandari M, Baghlani A, Ahmadi SA (2013) Modeling total sediment load in rivers using artificial neural networks.

© 2024 by the authors. Licensee SCU, Ahvaz, Iran. This article is an open access article distributed under the terms and conditions of the Creative Commons Attribution 4.0 International (CC BY 4.0 license) (http://creativecommons.org/licenses/by/4.0/).

Journal of Hydraulic Structures
J. Hydraul. Struct., 2024; 10(3): 51-71
DOI: 10.22055/jhs.2024.46835.1298



OPEN ACCESS

Application of machine learning methods on investigation the effect of interrupted deflector's height and downstream depth changes on energy dissipation at flip bucket spillways

Arash Adib[1]
Danial Ebrahimzadeh[2]
Mahmood Shafaei Bejestan[3]
Morteza Lotfirad[2]
Masoud Oulapour[2]

Abstract

Flip bucket is a type of energy dissipator structure. Flip buckets can sometimes be improved by adding wedge-shaped deflectors. This research introduced the best height proportion of used deflector on the flip buckets to increase energy dissipation. It used 4 types of deflector series including 32, 45, 47 and 55 degrees toward horizon with two different regular and irregular layouts and 19 different heights from 2.31 to 5.6 cm and in different hydraulic condition and the results were compared with a flip bucket without a deflector. The characteristics of laboratory flume were: length= 7.5 m, width= 0.58 m and height= 1.6 m. The results illustrates that the energy dissipation in the model with deflectors increased from 11.83 to 19.38 percent as compared with model without a deflector. The greatest percentage of energy dissipation was 80.74% which observed at a deflector angle of 55° and a discharge of 10 L/s, at deflector's ratio of n=0.8 and in non-uniform layout and in free hydraulic jump. Larger deflector angles and side lengths initially boosted energy dissipation, but this effect plateaued or even reversed at very large angles. For calculating energy dissipation and hydraulic jump length parameters, the regression relations were extracted in this research and results of this relations were compared with results of the gene expression programming (GEP), random forest (RF) and multivariate adaptive regression splines (MARS) methods. The results showed that the RF method is the most accurate method for calculating energy dissipation and hydraulic jump length parameters.

Keywords: Deflector, Flip bucket, Hydraulic jump, Froude number, RF

Received: 05 May 2024; Accepted: 26 May 2024

[1] Civil Engineering and Architecture Faculty, Shahid Chamran University of Ahvaz, Ahvaz, Iran, Email: arashadib@yahoo.com **(Corresponding author)**
[2] Civil Engineering and Architecture Faculty, Shahid Chamran University of Ahvaz, Ahvaz, Iran.
[3] Hydraulic Structure Department, Faculty of Water and Environmental Engineering, Shahid Chamran University of Ahvaz, Ahvaz, Iran.

CC BY

1. Introduction

Without energy dissipaters, the powerful flow of water from a spillway can scour the riverbed downstream, eventually leading to structural problems and dam failure. These structures play a crucial role in safeguarding the dam and surrounding areas [1].

Because of the lack of appropriate design of an energy dissipation structure in spillways of dams, each year, many events have occurred in the world, these events endanger human lives, plants, animals, and the environment. The energy dissipation structures can reduce the number of these dangerous events and suitable design of these structures is an important problem. The flip buckets are one type of dissipating energy structure that is used to reduce the energy of the flow. The most common dissipators used in spillways are flip buckets, stepped chutes, and stilling basins with a hydraulic jump [2]. Depending on the geological and topographical features of the dam location, engineers often favor ski jump spillways with flip buckets as an economical way to handle water flow and energy reduction.

The following outcomes will be occurred because of ski-jump poor design [3]**:**

1- Bucket radius is too small Energy dissipation by dispersion may be insufficient

2- Extreme erosion due to water jet inopportune location to fall

3- Too small bucket trajectory angle makes energy dissipation by depreciation structure inadequate

Researchers [4] used a small-scale model to study how pressure distributes along a ski jump spillway equipped with a triangular flip bucket. These flip buckets are particularly useful in areas prone to cavitation, where water flow speeds exceed 15 to 20 meters per second [5]. Cavitation is the formation and collapse of bubbles which can damage the spillway structure. Flip buckets work by deflecting the high-speed water flow away from the dam itself. This reduces the risk of structural instability and erosion downstream [6]. In simpler terms, flip buckets act like a ramp, directing the forceful water flow away from the dam and protecting it from damage. Novak et al. [7] and Chadwick and Morfett [8] used diverse flip bucket types at the end of spillway and chutes. To achieve efficient energy dissipation, the flip bucket's minimum radius is recommended to be 3 to 5 times greater than the approaching flow depth. Additionally, the lip angle (or takeoff angle) should range from 20° to 35° to promote a jet spreading angle of roughly 5° in the air [9]. There are three parameters that they have a remarkable effect on the production of the maximum pressure and its magnitude: jet Froude number, relative bucket curvature, and the bucket angle [10]**.** Yamini et al. [11] conducted an experiment to analyze the influence of the entrance flow conditions on the pressure oscillations occurring on the bed of compound flip buckets. When there's more water coming in (higher depth and discharge) or the flow is less velocity (lower Froude number), the pressure on the spillway generally lessens. However, these conditions also lead to more frequent and larger variations in pressure (increased pressure fluctuations).

Nugroho et al. [12] surveyed the effect of the toothed spillway on the energy dissipation and the jump length with different arrangements and discovered that the length of hydraulic jump decreased compared to toothless mode and also energy dissipation soared about 30% to 50%. Deng et al. [13] presented a new type of ski-jump design and energy dissipation for baffled chute spillway. They analyzed the results and discovered that the optimal amount of the angular slope for desirable ski jump performance and sufficient amortization is from 30° to 45 °. Lian et al. [14] investigated the effect of the bucket type and angle on the downstream blade due to turbulent jet. Researchers compared the wind flow behind two types of spillway buckets (continuous and tab-shaped) at five different angles (40°, 45°, 50°, 55°, and 60°). They found that as the bucket angle increased, the height and width of the area affected by the downstream wind (think of it as the "wind blade") also increased. Interestingly, the effect on the length of the wind blade worked in

the opposite direction - it actually decreased with a larger bucket angle. The wind speed decreases in both types of buckets along the flow direction. Choi et al. [15] investigated the effect of deflector angle on the downstream grain of a submerged spillway. They tested four deflector models with angles of 0°, 30°, 45°, and 60° and discovered that the least angle for the deflector superior performance is 45° and in general a deflector can extend the throw length up to 40%. Daneshfaraz et al. [16] investigated how adding rough blocks to the base of an ogee spillway (a spillway with a particular curved shape) affects water flow. They looked at two aspects: how much energy is dissipated (lost) and how far the water travels (jet length). They tested spillways with and without a flip bucket (a structure at the end that redirects the water flow) at different angles. Their computer simulations showed the model accurately represented the water flow over the spillway. The presence of rough blocks on the spillway floor, in the absence of a flip bucket, resulted in a 15.4% increase in energy dissipation compared to a smooth floor configuration. When they added a flip bucket at 32 or 52 degrees, the increase in energy dissipation was slightly lower at 9.5%. In all cases, the rough blocks on the spillway floor significantly reduced the jet length by up to 58% compared to a smooth floor. Pourabdollah et al. [17] investigated how different types of stilling basins (structures used to control water flow) affect hydraulic jumps. They found that compared to a standard hydraulic jump, these basins resulted in a decrease in three key measurements: a) the depth of the calm water downstream (sequent depth) b) the depth of the turbulent flow within the jump (submerged depth) c) the total length of the zone where the jump occurs. The research by Heidarian et al. [18] centered on how the design of teeth (angle, arrangement, and radius) impacts three things: whirlpool formation, wasted kinetic energy, and the rate at which turbulence fades in the flow. The research revealed that unequal angles and a larger overall angle for the teeth were key factors in maximizing total turbulence loss. This implies that a strategic design with a mix of angles and a steeper tilt is most efficient in creating turbulence.

In addition to empirical studies, many types of research have been conducted using data mining techniques. A field of artificial intelligence that is related to representation and generalization using the data learning method is Machine learning (ML) [19].

Inspired by Darwin's theory of evolution, Gene Expression Programming (GEP) is a method that utilizes genetic operators like crossover and mutation to create improved solutions, similar to how new generations evolve in nature [20]. Several studies have compared GEP to other techniques for analyzing hydraulic phenomena. For example, researchers found GEP to be more accurate than methods like Support Vector Regression (SVR) and Artificial Neural Networks (ANN) when predicting characteristics of free hydraulic jumps in rough channels [21]. Similar results were obtained for studying hydraulic jumps in expanding channels and for determining discharge coefficients in ogee spillways [22 to 25]. These findings suggest that GEP is a powerful tool for analyzing hydraulic behavior, often surpassing traditional methods and other soft computing techniques [26].

Unlike most research on deflectors used with flip buckets, this study takes a fresh approach by analyzing how the angle and height of triangular deflectors on an ogee spillway affect both energy dissipation and the downstream hydraulic jump length. To understand how these deflectors work, researchers tested triangular deflectors of various sizes and angles under different water flow conditions. Using a technique called dimensional analysis, they were able to identify key factors (without specific numbers) that influence how much energy is dissipated and how long the hydraulic jump becomes with this type of deflector. Two relations to predicting energy dissipation and hydraulic jump length were obtained by multivariate nonlinear regression. Then, observed data were compared with results of different ML methods. The applied ML methods were GEP, RF and MARS methods. These methods have different bases. The base of GEP method is

nonlinear regression, evolutionary algorithm, the base of MARS method is linear nonparametric regression, and the base of RF method is ensemble learning under supervision and classification.

The research begins by highlighting the significance and need for the study.

Next, it delves into a technique called dimensional analysis, focusing on key hydraulic parameters.

The methodology section then details the materials and procedures used in the laboratory modeling stage.

Following that, the research explores the application of specific ML methods.

To analyze the findings, the next section utilizes graphs and laboratory observations.

Finally, the research culminates with a concluding section that summarizes the key takeaways.

In summary, the innovations and objectives of this research are:

- Simultaneous investigation of the effects of deflector height and angle on energy dissipation and hydraulic jump length downstream of a flip bucket. Two dimensionless relationships are derived for this purpose, whereas previous studies have not considered all of these factors.

- Selection of the best model among ML models that are prominent in water engineering (these models have different natures) for simulating energy dissipation and hydraulic jump length. Previous studies have typically used models with similar natures.

2. Material and methods

2.1. Dimensional analysis

Building a general correlation for flow energy dissipation begins with identifying the relevant variables that affect it. Ideally, these variables should be readily measurable input parameters to facilitate the development of a straightforward relationship. The energy dissipation of the flow over a flip bucket with a triangle deflector, ΔE, rely on the water density (ρ), the deflector angle (θ), the water dynamic viscosity (μ), the discharge per unit width of the approach channel (q), the bucket radius (R), the surface tension (σ), and the gravitational acceleration, (g), flow velocity (V), depth flow on the spillway (y), tailwater depth (y_t), opening ratio of the width of the flume ($\frac{\mathbf{L}}{\mathbf{B}}$), Reynolds number (Re), Weber number (We), the distance of the side deflectors to the channel wall (X_s), the distance of the deflectors from each other (X_m), height of the edge of the bucket from the floor of the channel (Z). These variables can be functionally expressed as:

$$\Delta E = f\ (\ \mu, \rho, \sigma, g\ ,V, R, Re\ ,We\ ,\ Fr\ ,\ \theta, \frac{y_t}{y}\ ,\ \frac{L}{B}, \frac{X_s}{X_m}, \frac{L_d}{L_b}) \quad (1)$$

Due to the turbulence of the flow in the present study and considering that the Reynolds number of the minimum flow is Re = 14171.6, so the ratio of viscosity to inertia is low and it has no effect on the motion of the flow, so we omit the Reynolds number in the effective parameters. Considering that the minimum height of water on the overflow crown in experiments is 2.8 cm (at a flow rate of 10 liters per second), the effects of surface tension and Weber number can be ignored [27].

We can express the relative energy dissipation (ΔE) of the flip bucket with a triangular deflector using a functional relationship that incorporates relevant parameters.

$$\Delta E = \frac{\Delta E}{E_0} = f\ (\mathrm{Fr}, \theta, \frac{y_t}{y}\ ,\ \frac{X_s}{X_m}, \frac{L}{B}, \frac{X_s}{X_m}, \frac{L_d}{L_b}) \quad (2)$$

$\frac{\mathbf{L}}{\mathbf{B}}$ = The opening ratio of the width of the flume, is equal to the transverse ratio of the flume that is not blocked by the deflectors to the total width of the flume, which is 0.35 in all experiments.

(Eliminated due to consistent value)

θ = The deflector angle to the horizon in terms of radians is equal to 0.558, 0.785, 0.82, 0.96.

$\frac{\mathbf{R}}{\mathbf{Z}}$ = The ratio of the radius of the bucket to the height of the edge of the bucket from the floor of the flume, which is constant in all experiments and is equal to 1.2 and does not help regression. (Eliminated due to fixed value)

$\frac{L_d}{L_b}$ = The ratio of the deflector length to the bucket chord length, which in all experiments has a constant value of 0.2. (Eliminated due to fixed value)

$\frac{X_s}{X_m}$ = The ratio of the distance of the side deflectors to the channel wall to the distance of the deflectors from each other, the value of this parameter is directly related to the arrangement of deflectors and in uniform and non-uniform arrangement is equal to 1 and 0.68, respectively. Utilizing a non-uniform arrangement mitigates the effects of the channel walls, leading to an increase in energy dissipation and a reduction in the length of the hydraulic jump downstream.

$\frac{\mathbf{y_t}}{\mathbf{y}}$ = The ratio of run-off depth to water depth at the overflow inlet. The value of y depends on the flow rate and the value of y_t is unique in each experiment.

Fr = The input Froude number to the cup which is a minimum of 6.331 and a maximum of 21.759.

2.2. Experimental model

Laboratory flume of hydraulic laboratory in the Water Sciences Faculty of Shahid Chamran University of Ahvaz was used as experimental model in this research. We used deflector series of four including 32, 45, 47, and 55 degrees toward the horizon with two different regular and irregular layouts. The heights of these deflectors are 2.31 to 5.6 cm based on 19 proportions from 0.33 to 0.8(the proportion was the height of the deflector to the critical depth of the maximum discharge). The layouts of deflectors were uniform and non-uniform layouts. The tests were performed by 12 discharges of 10 ,13.5 ,15 ,18 ,20 ,21 ,22 ,25 ,27 ,30, 32 and 35 Lit/s and three different tailwater conditions to create classical, semi-submerged and submerged hydraulic jumps. The total number of tests was 5508 tests. In all experiments, it was recorded the trajectory coordinate and all geometrical characteristics and hydraulic parameters before and after the ski jump. The features of flume and tests are:

Deflector design and testing:

- The deflectors were wedge-shaped with different angles and a width matching the flume channel (waterway). See Fig. 2 for examples.

-Researchers investigated deflectors with various angles (**θ=**32° to 55°) and a single size (L=10 cm side length).

-The deflectors were positioned at a specific height relative to the maximum water depth from the spillway (critical depth).

-The bottom of each deflector was kept parallel to the bottom of the flip bucket.

Experimental setup:

-A pump upstream of the channel-controlled water flow, measured by a flow meter.

-Water height over the spillway crest and the jet trajectory downstream were measured with a point gauge.

-Fig. 1 illustrates the overall setup (flip bucket, deflectors, etc.).

-Fig. 3 shows an example experiment with a specific flow rate and deflector angle.

Testing procedure:

-A total of 5508 tests were conducted with different flow rates, with and without deflectors.

-Key measurements throughout the tests included water discharge, tailwater depth, upstream and over-crest flow depths.

-Downstream flow depth was challenging to measure directly due to air bubbles and turbulence.

-To address this, a gate was used to create a hydraulic jump (a sudden increase in water depth) downstream, allowing for easier depth measurement.

-Using established relationships and the measured jump depth, researchers calculated the initial downstream depth.

-Finally, they calculated the energy dissipation of the water flow for each test using water depths and flow velocities upstream and downstream of the spillway.

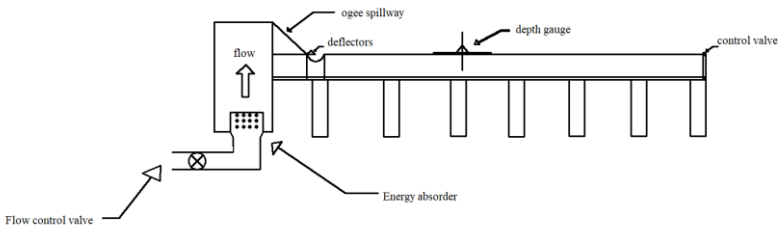
Energy dissipation calculations:

-The calculations considered the energy before (upstream) and after (downstream) the flip bucket and the hydraulic jump.

-Specific formulas were used based on water depths and velocities at different points.



(a)



(b)

Figure 1. a) The used laboratory flume in this study b) A detailed cross-sectional view of the laboratory flume used in the experiment

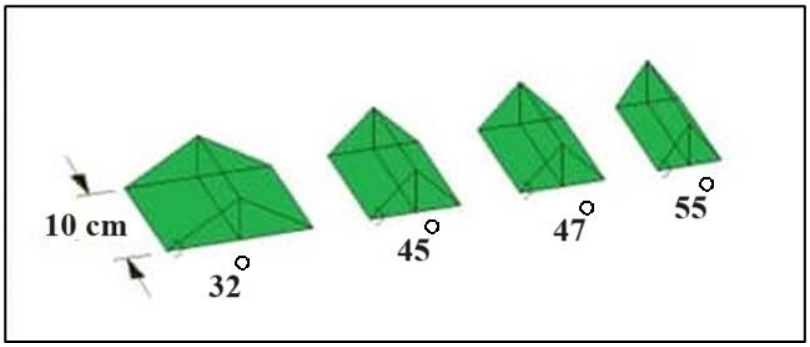


Figure 2. Geometric features of deflectors

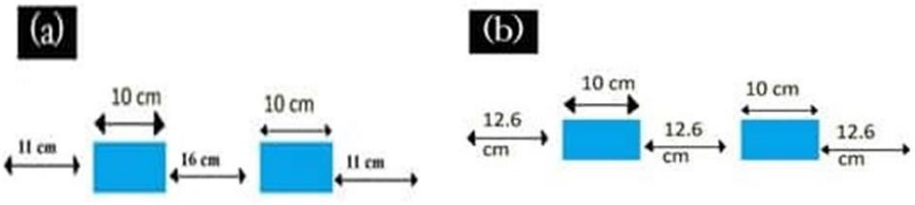


Figure 3. a) The position of the deflectors in non-uniform layout b) Uniform layout

Table 1. Parameters of the applied experimental models in this study

Deflector Characteristics	Flow Characteristics		
Θ	Q(L/s)		Tailwater conditions
Without a deflector	10	22	Classical hydraulic jump
32°	13.5	25	
45°	15	27	Semi-submerged hydraulic jump
47°	18	30	
55°	20	32	submerged hydraulic jump
	21	35	

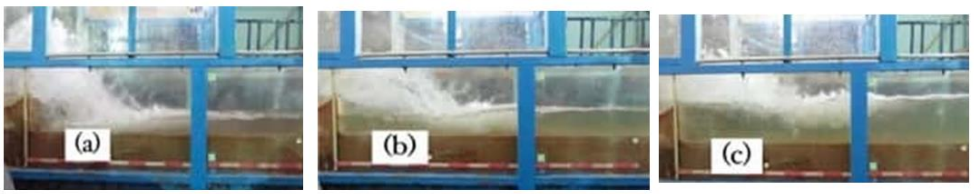


Figure 4. Experiment at the discharge of 15 L/s in the presence of a deflector with an angle of 32° in three different tailwater conditions: a) free b) semi-submerged c) submerged

In order to calculate the length of free hydraulic jump, the following experimental equation can be used:

$$L_j = A(y_2 - y_1) \quad (3)$$

A is an experimental coefficient whose value varies between 5 and 6.9 and for practical work it can be assumed to be equal to 6 [2].

Govinda Rao and Rajaratnam [28] to determine the length of submerged hydraulic jump presented a relationship:

$$L_j = [4.9(\frac{y_4 - y_2}{y_2}) + 6.1]\, y_2 \quad (4)$$

y_4 =Tailwater depth of Submerged hydraulic jump

y_2 =Tailwater depth of free hydraulic jump

Chow [29] showed that in rectangular channels with a horizontal floor, y_3 (initial depth of submerged jump) can be obtained from the following equation:

$$\frac{y_3}{y_4} = [1 + 2Fr_4^2(1 - \frac{y_4}{y_1})]^{\frac{1}{2}} \quad (5)$$

y_1 =Tailwater depth of free hydraulic jump

2.3. Conventional regression methods

The effectiveness of recommended ML models was assessed by comparing them to established methods like linear (LR) and non-linear regression (NLR). These traditional techniques were used to analyze the experimental data and derive equations describing both linear and non-linear relationships.

2.4. Gene Expression Programming (GEP)

In 2001, Ferreira [30] introduced Gene Expression Programming (GEP), inspired by Genetic Algorithms (GA) and Genetic Programming (GP). GEP offers several advantages. First, its genetic operators work directly on the chromosomes, leading to simpler diversity management. Second, GEP's unique multi-gene structure allows it to build complex applications with multiple subroutines.

Similar to GA, GEP uses biological evolution principles to create computer programs that simulate real-world phenomena [30]. GEP relies on two key elements: chromosomes, which contain the encoded genetic information, and expression trees, where this information is translated into functional programs [31]. Unlike GP, GEP uses simple, fixed-length chromosomes but allows for diverse tree structures to express the program logic.

The GEP algorithm stops when either a satisfactory solution is found or a predefined number of generations is reached [32]. The process starts by defining the function set (available operations), terminal set (data elements), a fitness function (to evaluate solutions), control parameters, and a stopping condition.

Initially, predicted values are compared to actual values. If the difference falls within a tolerance level, the process ends with the best solution found so far. Otherwise, chromosomes are selected for recombination (creating new variations) using a roulette wheel selection method. The fitness of these new chromosomes is then evaluated, and the cycle repeats until a satisfactory solution emerges [33].

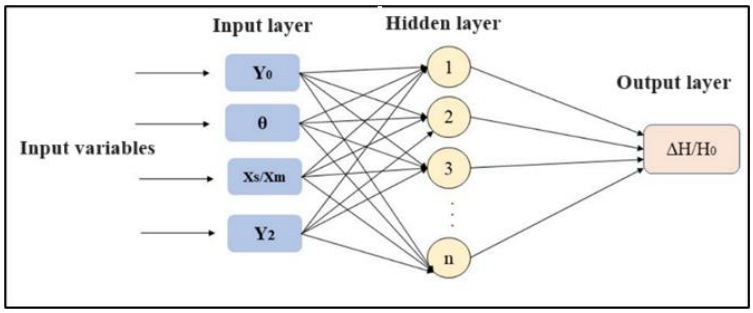


Figure 5. The specific design of the artificial neural network employed in this research

GEP utilizes traditional genetic operators alongside innovative techniques to achieve optimal solutions. The first step involves navigation, which creates an initial population of diverse candidate solutions encoded as chromosomes.

These chromos

omes are then translated into functional programs using a novel process called Expression Tree (ET). GEP uses fixed-length genes composed of terminals (representing variables like z1, z2, z3) and functional operators (+, ×, -, /, √, tanh, log, exp, etc.) [33,34]. Table 2 outlines the details of the GEP model. In this study, 70% of the data were used for training and 30% for testing.

Table 2. Details of the experimental models in this study

Parameter	Value
Number of Chromosomes	30
Head Size	7 and 8
Number of Genes	3
Linking Function	Addition
Fitness Function	MSE
Mutation Rate	0.039 & 0.042
Inversion Rate	0.1
One-Point Recombination	0.2
Two-Point Recombination	0.3
Gene Recombination	0.2
Gene Transposition	0.1
IS Transposition	0.1
RIS Transposition	0.1
Operator	+, - , ×, /, Pow, Sqrt, Exp, Ln, Atan, sin

2.5. Random Forest (RF)

The Random Forest algorithm is a supervised learning technique that leverages a group of decision trees to make predictions. As the name suggests, the forest is built randomly by combining multiple decision trees, often using a technique called bagging.

Bagging is a method that creates multiple decision trees from random data subsets. This helps to reduce the model's sensitivity to specific data points, resulting in a more stable and reliable final model.

Essentially, a Random Forest combines the strengths of several decision trees to make more robust predictions. It operates by constructing a set of regression trees based on a subset of training data. Three key parameters influence the forest's structure: the number of trees, the number of variables considered when splitting each node, and the maximum depth of the trees.

A significant advantage of Random Forests is that they do not require pruning the individual trees, which simplifies the modeling process. Additionally, they offer the versatility of handling both classification and regression tasks, making them a popular choice in ML applications [35].

Further details about the inner workings of Random Forests can be found in various research papers, such as the one by [36].

2.6. Multivariate Adaptive Regression Splines (MARS)

Developed by Friedman [37] in 1991, the MARS method excels at creating accurate models for various data types, including continuous, discrete, and binary variables. It's particularly adept at uncovering hidden patterns within the data.

The key to MARS's effectiveness lies in its unique structure, which combines three powerful approaches: standard linear regression, spline functions, and binary recursive partitioning.

-Linear Regression: MARS builds a foundation of linear regression models.

-Spline Functions: These functions introduce non-linearity by splitting the data into multiple regions with different linear relationships.

-Binary Recursive Partitioning: This technique systematically divides the data based on specific thresholds (called "knots") to create these different regions.

The resulting model combines multiple "basis functions" (BFs), each representing a linear relationship within a specific data region. Knots mark the boundaries between these regions. BFs are generated through a stepwise search process, ultimately leading to a flexible non-linear model.

$$Y = f(x) = \psi_0 + \sum_{m=1}^{M} \psi_m BF_m(x) \quad (6)$$

Y represents the outcome or dependent variable you're trying to predict.

BF stands for basis function, a building block of the model that captures a specific linear relationship within a data region.

x represents one or more predictor variables that influence the outcome (Y).

ψm denotes the coefficient associated with a particular basis function (BF). There can be multiple BFs (M total) in the final model, each with its own coefficient.

3. Results and discussion

In this study, firstly, with performing an experimental study and setting up free, semi-submerged and submerged hydraulic jumps, the data required to evaluate the performance of a new GEP model are examined and compared with the other researches. In the following, the results of prediction of free, semi-submerged and submerged hydraulic jumps characteristics by GEP model are presented. It should be mentioned that, in the present study, to ensure the free hydraulic jump formed exactly where the water jet struck the flume bottom, researchers strategically limited the water flow by partially closing the flume's exit valve. Also, in order to create semi- submerged and submerged hydraulic jumps in the first and second state, the valve to some extent was closed in proportion to the inlet flow of the water level downstream of the overflow, respectively, to the middle of the bucket and adjust its edge. It should be noted that the energy losses are due to the presence of the launcher structure (ogee spillway) has occurred alone, however, the energy losses have been solely due to the ski jump and the energy dissipation due to the downstream hydraulic

jump is not considered. As seen in the Fig. 6, in the control experiments as the flow rate decreases, the Froude number of inlet to the bucket increases, followed by this, the percentage relative energy losses have increased. These results clear that in high discharges, launcher structure's efficiency reduced, and energy dissipation of flip-bucket at high Froude numbers decreases and flip bucket has better efficiency in energy losses.

3.1. Energy dissipation

3.1.1. Experimental results

Fig. 7 compares the energy dissipation in different deflector angles(**θ**) used in this study. In general, it can be stated that the deflector angles 32°sand 45° have better performance in in energy dissipation as compared with other models. A maximum energy dissipation was about 80.74% which observed at a deflector angle of 55° and a discharge of 10 L/s, at deflector's ratio of n=0.8 and in non-uniform layout and in free hydraulic jump where the deflector's height was 5.6 cm. But Khalifehei et al. [6] showed that maximum energy dissipation was about 71% which observed at a deflector angle of 12° and a discharge of 10 L/s where the deflector's height was 0.6 cm. The minimum jump length was about 8.12%, which occurred at deflector angle of 47° and a discharge of 35 L/s, at deflector's ratio of n=0.33 and in uniform layout.

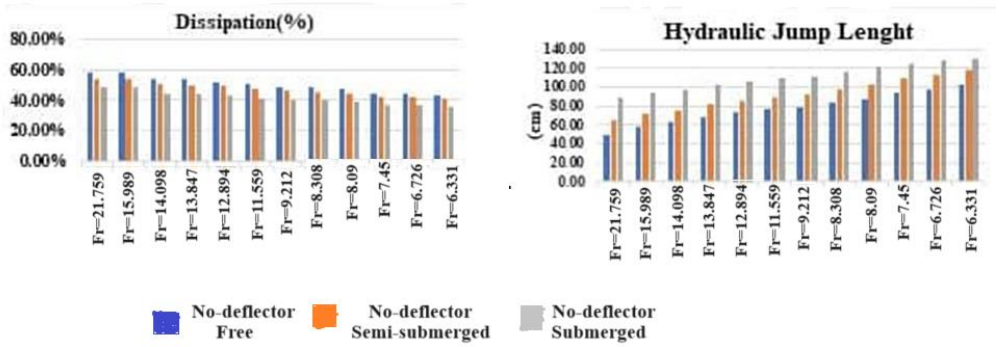


Figure 6. Control tests without deflector. A) Energy Dissipation, B) Hydraulic Jump Length

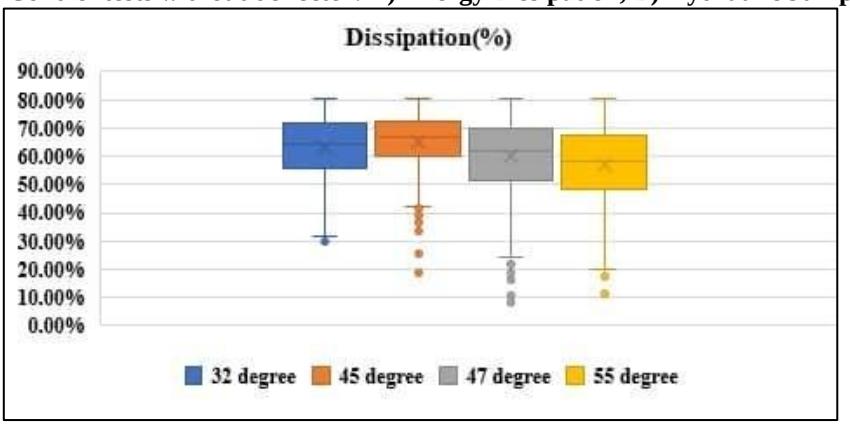


Figure 7. Energy dissipation in different deflector angles

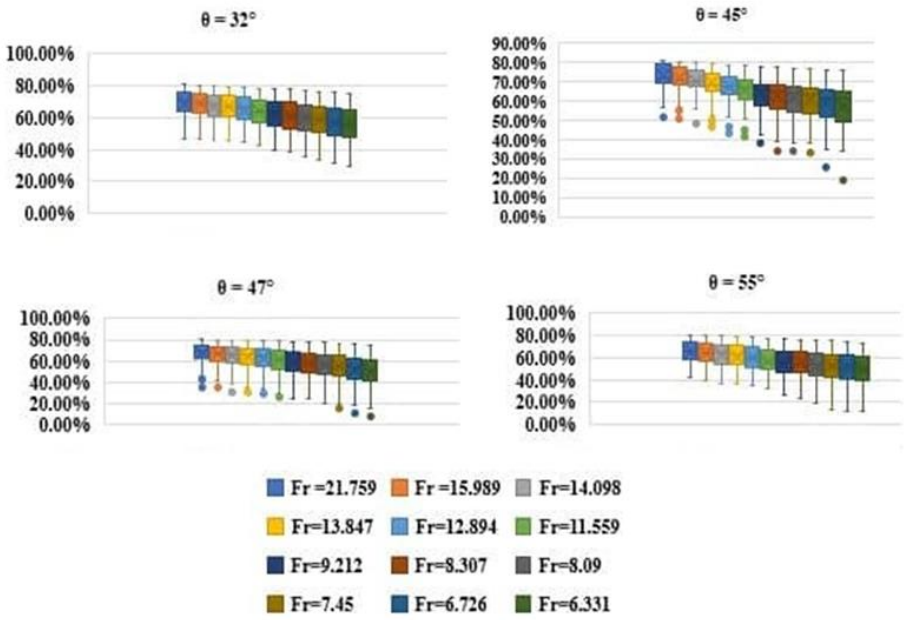


Figure 8. Percentage of energy dissipation in different deflector angle

Fig. 8 shows energy dissipation versus Froude number at different deflectors angles. As can be seen, energy dissipation decreases in all models, by decreasing the Froude number. Therefore, in a fixed angle model, Energy dissipation decreases with increase in discharge (yc). Comparing the results of the models with deflectors in Fig. 8 and without in Fig. 6 demonstrates that the bucket with a deflector causes higher energy dissipation than no- deflectors in all tests. It can be seen that in low Froude numbers (high discharges), the difference in energy dissipation versus no-deflector mode is less than in cases where the Froude number is higher, and this indicates that the arrangement of the deflectors in higher Froude numbers (lower discharge) that the inlet flow depth to the spillway is more effective.

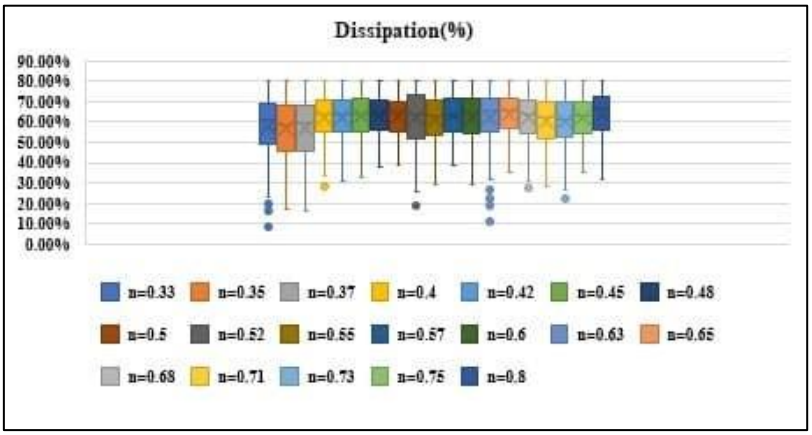


Figure 9. Percentage of Energy dissipation in different deflector's height ratios

Fig. 9 portrays the changes in the energy dissipation in all height deflector's ratios used in this study. Fig. 4 shows that the energy dissipation is steadily fluctuating as the ratio increases from

n=0.48 to n=0.57. The energy dissipation initially decreases with an increase in the deflector's height ratios from n=0.33 to n=0.54 and also from n=0.6 to n=0.8 which it experiences a downtrend at two larger ratios of n=0.33 and n=0.63. A maximum energy dissipation of about 80.74% was observed at a deflector angle of 55° and a discharge of 10 L/s, at deflector's ratio of n=0.8 and in non-uniform

layout, however, the minimum Energy dissipation was about 80.07%, which occurred at deflector angle of 47° and a discharge of 35 L/s, at deflector's ratio of n=0.33 and in uniform layout. Fig. 5 compares the Percentage of Energy dissipation in different deflector angles(θ) used in this study. Generally, we can conclude that the impact of the deflectors angle (**θ**) for a given deflector length, it can be stated that the deflector angles 45°sand 47° results in optimal energy dissipation as compared with the model without a deflector.

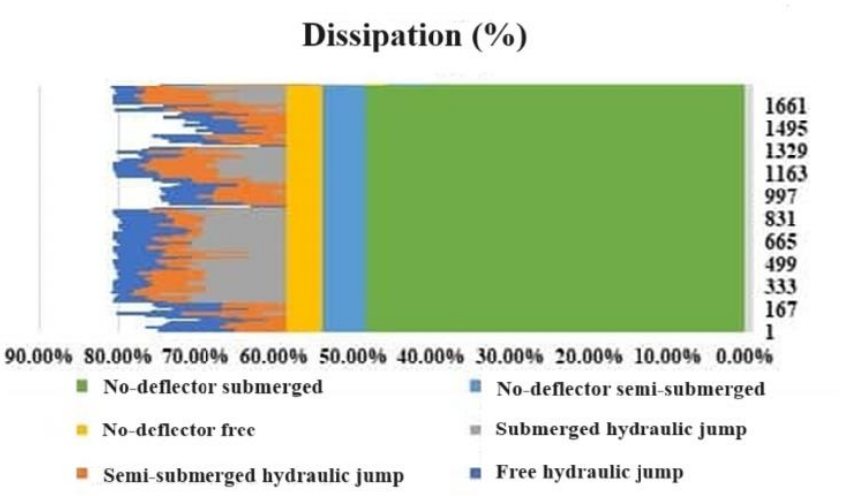


Figure 10. Energy dissipation in different condition

Fig. 10 shows energy dissipation in all different submergence condition. At a constant discharge with increasing downstream water depth, the percentage of relative energy loss decreases. Because with increasing the tailwater depth, the hydraulic jump at the downward moves towards the upward and the process of throwing the jet to downwards and depreciating due to ski jump does not occur completely. Jets are thrown from the flip bucket and deflectors before complete crossing through its curved path and depreciation due to collisions with air currents and each other to the tail water. So, in any definite discharge, the energy consumed by the flip bucket and deflectors in free hydraulic jump are more than 50% immersion ratio and energy dissipation in 50% immersion ratio is more than 100% immersion ratio

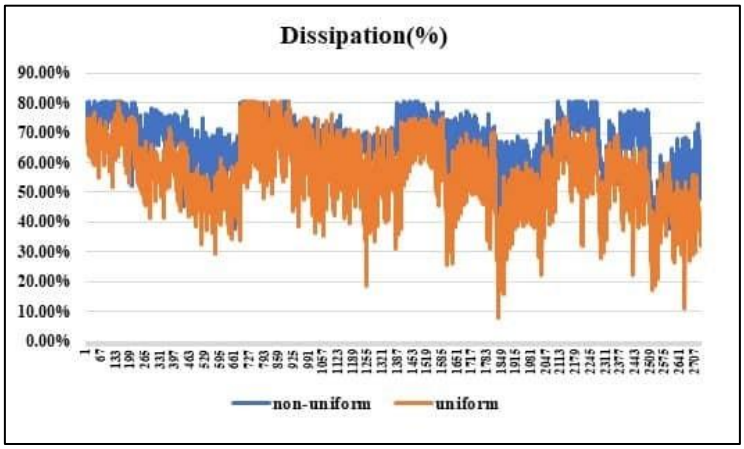


Figure 11. Energy dissipation in two different layouts

Fig. 11 portrays the energy dissipation in different layout condition. It's clear that in free, semi-submerged and submerged hydraulic jump modes in all Froude numbers, the non-uniform arrangement mode performed better than the uniform arrangement in energy dissipation and it was able to generate more depreciation. This performance has been such that the non-uniform arrangement has been able to create 17.1% more depreciation than the uniform arrangement. The reason for this difference is that in the non-uniform arrangement, the distance of the deflectors is less than the lateral arrangement of the side walls and the boundary layer formed between the overflow channel wall and the water flow causes more depreciation.

Eq. 7 was derived by multivariate nonlinear regression to predict energy dissipation in a flip bucket with a deflector, using the effective parameters extracted in the dimensional analysis section:

$$\boldsymbol{\Delta E} = \frac{-\mathbf{0.38}\left(log\frac{y_t}{y}\right)^{\mathbf{1.349}} + \left(\mathbf{0.454}\left(Fr_1^{\mathbf{0.194}}\right)\left(\frac{X_s}{X_m}\right)^{\mathbf{-0.25}}\right)}{\boldsymbol{\theta}^{\mathbf{0.096}}} \quad (7)$$

The statistical indices, R^2 and RMSE, were calculated to express the accuracy of the above correlations. R^2, RMSE for Eq. 7 were equal to 0.76 and 0.12 cm, respectively.

3.2. Jump length

3.2.1. Experimental results

Fig. 12 compares the hydraulic jump length in different deflector angles(θ) used in this study. In general, it can be stated that the deflector angles 32° and 47° results are optimal in hydraulic jump length as compared with other models. As can be seen in Fig. 6, generally, as Froude number got bigger, the jump length has decreased. It is obvious that the hydraulic jump length is steadily reducing as the Froude number increases from 6.331 to 21.759. A maximum jump length was about 259.4 cm which observed at a deflector angle of 45° and a discharge of 35 L/s, at deflector's ratio of n=0.8 and in uniform layout and submerged hydraulic jump, however, the minimum jump

length was about 0.98 cm which occurred at deflector angle of 32° and a discharge of 10 L/s, at deflector's ratio of n=0.48 and in non-uniform layout.

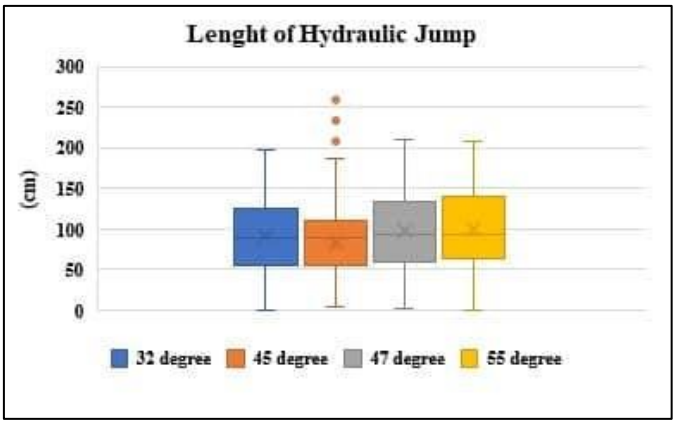


Figure 12. Length of Hydraulic Jump in different deflector angles(θ)

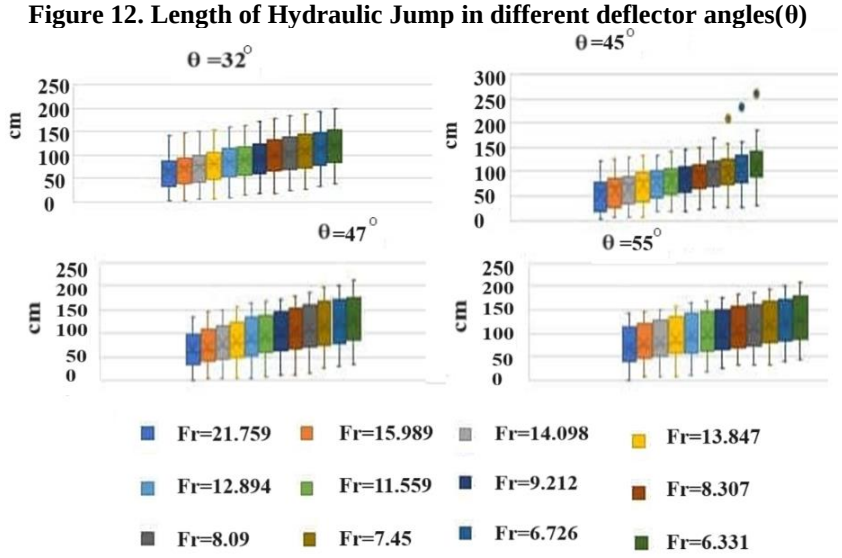


Figure 13. Length of Hydraulic Jump in deflector angle(θ)

Fig. 13 shows the hydraulic jump length against Froude number at different height ratios. Comparing the results of the models with deflectors in Fig. 13 and without in Fig. 6 represents that the bucket with a deflector affords reducing hydraulic jump length than example tests in some cases, while, in some ratios of deflectors used in this research, using deflectors has not any remarkable influence on the hydraulic jump length. As clearly seen in Fig. 14, the hydraulic jump length is steadily fluctuating as the ratio decrease from n=0.33 to n=0.52 in contrast, the hydraulic jump length initially increases with an increase in the deflector's height ratios from n=0.55 to n=0.8, however, it experiences a downtrend at two larger ratios of n=0.65 and n=0.8.

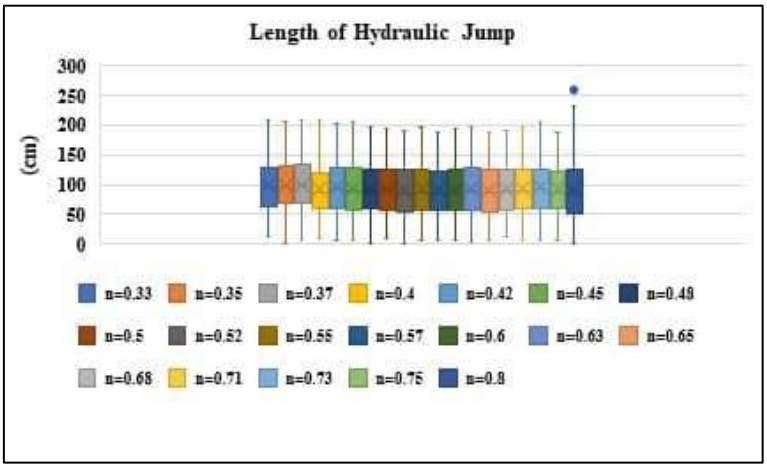


Figure 14. Length of Hydraulic Jump in different deflector's height ratios

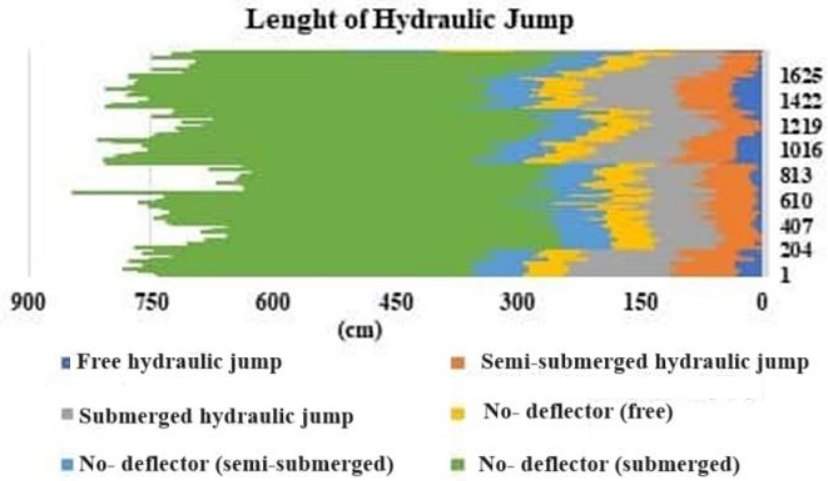


Figure 15. Hydraulic Jump Length in different submergence conditions

Fig. 15 shows the hydraulic jump length in two different submergence conditions. The results of measuring the length of the hydraulic jump downstream of the launcher structure indicate that in a certain flow rate, as the water depth downstream being less, the length of the hydraulic jump will be less. It means that in the adjusted mode downstream to form a free hydraulic jump, the free hydraulic jump length is less than the immersion ratio of 50% and in the 50% immersion ratio the jump length is shorter than the immersion ratio of 100%. In all Froude numbers increase in angle deflector from 32 to 45 degrees has reduced the length of the hydraulic jump and by increasing the angle deflector from 47 to 55 degrees we have seen an increase in the length of the hydraulic jump.

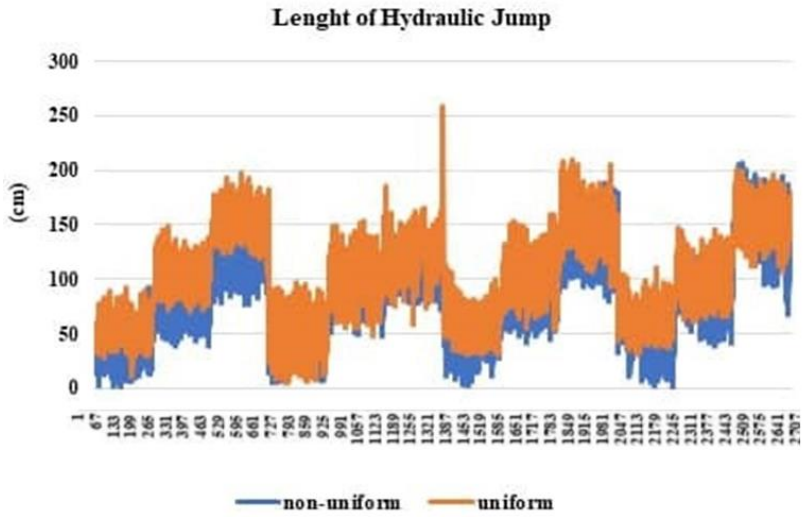


Figure 16. Hydraulic Jump Length in two different layouts

Fig. 16 illustrates the hydraulic jump length in two different layouts. It can be seen that in the free, semi-submerged and submerged hydraulic jump modes in all Froude numbers, the non-uniform arrangement mode performed better than the uniform arrangement in hydraulic jump length and was able to reduce length of hydraulic jump more. This performance has been such that the non-uniform arrangement has been able to reduce the hydraulic jump length 20.35% than the uniform arrangement.

Eq. 8 is the result of our analysis. We employed multivariate nonlinear regression, a statistical method, to create this equation. It predicts the hydraulic jump length in a flip bucket with a deflector, considering the important factors revealed earlier using dimensional analysis.

$$L_j = \frac{0.37\left(\frac{y_t}{y}\right)+\left(5.747\left(Fr_1^{-0.099}\right)\left(\frac{X_s}{X_m}\right)^{0.072}\right)}{\theta^{-0.014}} \quad (8)$$

To assess how well Eq. 8 predicts the actual jump length, we calculated two statistical measures: R^2 and RMSE. R^2 was 0.96, indicating a very good agreement between the predicted and measured values. RMSE was 18.61 cm, which means the equation's predictions typically differed from the real values by less than 19 cm.

The results of different ML methods are shown in Table 3 and Fig. 17 (Taylor diagram).

Table 3. Performance of utilized methods

Parameter	Period	Criteria	Reg	GEP	MARS	RF
ΔE	Training	R^2	0.76	0.75	0.77	0.85
ΔE	Test	R^2	0.70	0.70	0.75	0.86
ΔE	Training	RMSE (cm)	0.12	0.12	0.11	0.10
ΔE	Test	RMSE (cm)	0.14	0.13	0.11	0.09
Lj	Training	R^2	0.96	0.97	0.98	0.99
Lj	Test	R^2	0.90	0.90	0.96	0.98
Lj	Training	RMSE (cm)	18.6	18.50	18.10	17.98
Lj	Test	RMSE (cm)	19	19.2	18.2	18

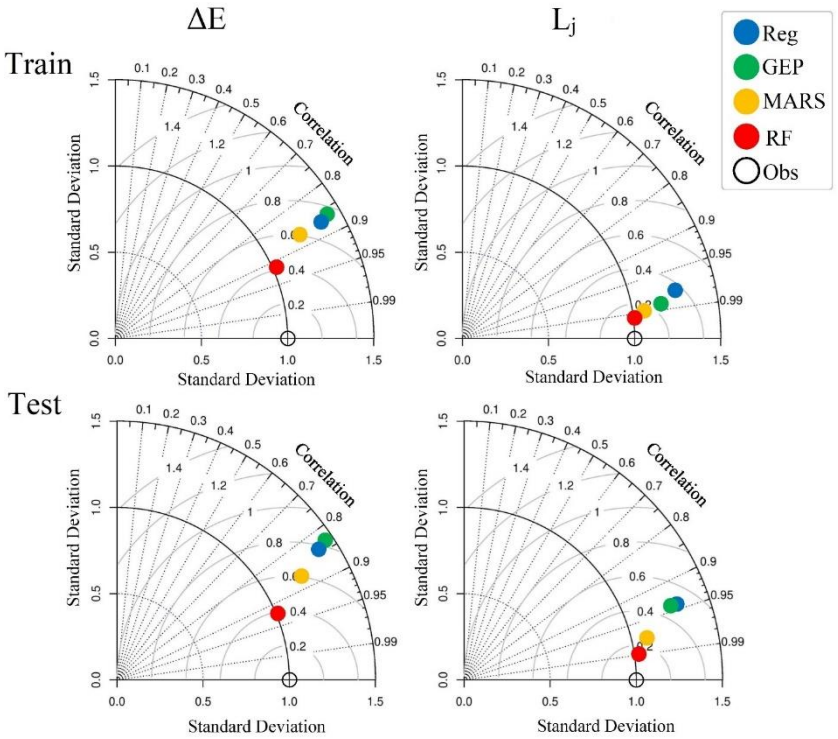


Figure 17. The Taylor diagram for the estimation of ΔE and Lj

Table 3 and the Taylor diagram illustrate that the RF model is the best method for estimating energy dissipation and hydraulic jump length. This method has the highest R^2 and the lowest RMSE. Among ML methods, the results of RF and MARS methods are more accurate than results of the extracted regression relations for energy dissipation and hydraulic jump length (Eqs. 7 and 8).

4. Conclusion

During the present study, the effect of the flip bucket besides the discontinuous transverse deflectors on the energy dissipation and hydraulic jump length surveyed. For this purpose, 5508 experiments including control and equipped with deflectors in four different angles and 19 different heights were performed, the summarizes of the results are given below. Overall, the addition of a triangular deflector to the flip bucket significantly improved its energy dissipation compared to models without one. This improvement was observed across different flow conditions: free, semi-submerged, and submerged hydraulic jumps. Specifically, the deflector increased energy dissipation by 19.5% (free jump), 14.63% (semi-submerged jump), and 11.8% (submerged jump) compared to the models without a deflector.

The study also found that the angle of the deflector (θ) plays a crucial role. As the angle increased, so did the energy dissipation, reaching an optimal range between 32° and 45°. Additionally, there seems to be a sweet spot for the deflector's height relative to the critical depth of the maximum discharge (n). The optimal height ratio was found to be n = 0.8.

Finally, this research achieved a significant outcome: a correlation for predicting the hydraulic jump length behind a flip bucket with a triangular deflector. This correlation was derived using dimensional analysis and multivariate nonlinear regression, considering the influence of multiple

factors. However, the results of measuring the length of the hydraulic jump at the downstream of ogee spillway indicates that in a certain flow rate, the lower water depth downstream, makes the hydraulic jump shorter. This means that in the downstream adjusted mode for free hydraulic jump, the hydraulic jump length is less than in the semi-submerged and in the semi-submerged, length of the hydraulic jump is shorter than the submerged hydraulic jump. An optimum angle of 32° was obtained with an optimal deflector's height ratio of n=0.52. Finally, we obtained a correlation by dimensional analysis and multivariate nonlinear regression for hydraulic jump length by a flip bucket with a triangular deflector.

In this study, four models with the nature of supervised ensemble learning (RF), nonparametric regression (MARS), evolutionary algorithm (GEP), and nonlinear regression were employed. The results of this study, with an R^2 of 0.99 in estimating the hydraulic jump length, are superior to the results obtained from the study by [21], which used the GEP model and reported an R^2 of 0.71. The results of this study are also significantly better than those of the study by [22], which estimated the R^2 of the jump length using the GEP model to be 0.7. Therefore, the use of ML models for estimating hydraulic parameters is highly accurate. Since these models do not require a lot of time to run, they are preferred over traditional methods for estimating hydraulic characteristics.

This study has some limitations that are recommended to be considered in future studies. These limitations include:

- The effect of deflector length on energy dissipation was not investigated.
- The phenomenon of cavitation at the deflector installation location was not investigated.
- Flip buckets with different geometries were not used, and the energy dissipation in them was not compared.

References

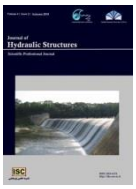
1. Arjenaki MO, Sanayei HRZ, (2020). Numerical investigation of energy dissipation rate in stepped spillways with lateral slopes using experimental model development approach. Model Earth Syst Environ 6(2): 605-616. https://doi.org/10.1007/s40808-020-00714-z
2. Hager W.H., Energy Dissipators and Hydraulic Jump. Water Science and Technology Library, vol 8. Springer, Dordrecht, pp.1-4,1992. https://doi.org/10.1007/978-94-015-8048-9_1
3. Vischer D.L., Hager W.H., Energy dissipators: IAHR hydraulic structures design manual 9. 1st Edition, Routledge, London, 208 p, 1995. https://doi.org/10.1201/9780203757512
4. Steiner R., Heller V., Hager W.H., Minor H.E., (2008). Deflector ski jump hydraulics. J Hydraul Eng 134(5): 562–571. https://doi.org/10.1061/ (ASCE)0733-9429(2008)134:5(562).
5. Khatsuria R.M., Hydraulics of spillways and energy dissipators. 1st Edition, CRC Press, Boca Raton, 680 p, 2004. https://doi.org/10.1201/9780203996980
6. Khalifehei K., Askari M.S., Azamathulla H., (2022). Experimental investigation of energy dissipation on flip buckets with triangular deflectors. ISH J Hydraul Eng 28(sup1): 292-298. https://doi.org/10.1080/09715010.2020.1775716
7. Novak P., Moffat A.I.B., Nalluri C., Narayanan R., Hydraulic structures. 4th Edition, CRC Press, London, 736 p, 2007. https://doi.org/10.1201/9781315274898
8. Chadwick A., Morfett J., Hydraulics in civil and environmental engineering. 1st Edition, CRC Press, London, 632 p, 2002. https://doi.org/10.4324/9780203027776
9. Mason P. (1984). Erosion of plunge pools downstream of dams due to the action of free-T-rajectory jets. P I Civil Eng 76(2): 523–537. doi:10.1680/iicep.1984.1257

10. Heller V., Hager W.H., Minor H.E., (2005). Ski jump hydraulics. J Hydraul Eng 131 (5): 347–355. doi:10.1061/(ASCE)0733-9429(2005)131:5(347)
11. Yamini O.A., Kavianpour M.R., Mousavi S.H., Movahedi A., Bavandpour M., (2018). Experimental investigation of pressure fluctuation on the bed of compound flip buckets. ISH J Hydraul Eng 24(1): 45–52. doi:10.1080/ 09715010.2017.1344572
12. Nugroho J., Soekarno I., Soeharno A.W.H., (2019). Experimental study of energy dissipation at baffled chute spillway. Jurnal Teknik Sipil, 26(1): 33-38. DOI: 10.5614/jts.2019.26.1.5
13. Deng J., Wei W., Tian Z., Zhang F., (2018). Design of a streamwise-lateral ski-jump flow discharge spillway. Water 10(11): 1585. https://doi.org/10.3390/w10111585
14. Lian J., He J., Gou W., Ran D., (2019). Effects of bucket type and angle on downstream nappe wind caused by a turbulent jet. Int J Env Res Pub He 16(8): 1360. https://doi.org/10.3390/ijerph16081360
15. Choi C.E., Ng C.W.W., Goodwin S.R., Liu L.H.D., Cheung W.W., (2016). Flume investigation of the influence of rigid barrier deflector angle on dry granular overflow mechanisms. Can Geotech J 53(10): 1751-1759. https://doi.org/10.1139/cgj-2015-0248
16. Daneshfaraz R., Ghaderi A., Akhtari A., Francesco S.D., (2020). On the effect of block roughness in ogee spillways with flip buckets. Fluids 5(4): 182. https://doi.org/10.3390/fluids5040182.
17. Pourabdollah N., Heidarpour M., Koupai J.A., (2020). Characteristics of free and submerged hydraulic jumps in different stilling basins. P I Civil Eng-Wat M 173(3): 121–131. https://doi.org/10.1680/jwama.19.00029
18. Heidarian P., Neyshabouri S.A.A.S., Khoshkonesh A., Bahmanpouri F., Nsom B., Eidi A., (2022). Numerical study of flow characteristics and energy dissipation over the slotted roller bucket system. Model Earth Syst Environ 8(4):5337-5351. https://doi.org/10.1007/s40808-022-01372-z
19. Sun M., Li Y., (2020). Eco-environment construction of English teaching using artificial intelligence under big data environment. IEEE Access 8: 193955–193965. doi: 10.1109/ACCESS.2020.3033068
20. Akhbari A., Ibrahim S., Zinatizadeh A.A., Bonakdari H., Ebtehaj I., Khozani Z.S., Vafaeifard M., Gharabaghi B., (2019). Evolutionary prediction of biohydrogen production by dark fermentation. Clean-Soil Air Water 47(1): 1700494. https://doi.org/10.1002/clen.201700494
21. Karbasi M., Azamathulla H.M., (2016). GEP to predict characteristics of a hydraulic jump over a rough bed. KSCE J Civ Eng 20(7): 3006–3011. https://doi.org/10.1007/s12205-016-0821-x
22. Roushangar K., Ghasempour R., (2018). Explicit prediction of expanding channels hydraulic jump characteristics using gene expression programming approach. Hydrol Res 49(3): 815–830. https://doi.org/10.2166/nh.2017.262
23. Salmasi F., (2021). Effect of downstream apron elevation and downstream submergence in discharge coefficient of ogee weir. ISH J Hydraul Eng 27(4): 375-384. https://doi.org/10.1080/09715010.2018.1556125
24. Nasrabadi M., Mehri Y., Ghassemi A., Omid M.H., (2021). Predicting submerged hydraulic jump characteristics using machine learning methods. Water Supply 21(8): 4180–4194. https://doi.org/10.2166/ws.2021.168
25. Bagatur T., Onen F., (2016). Computation of design coefficients in ogee-crested spillway structure using GEP and regression models. KSCE J Civ Eng 20(2): 951–959. https://doi.org/10.1007/s12205-015-0648-x

26. Samadi M., Sarkardeh H., Jabbari E., (2021). Prediction of the dynamic pressure distribution in hydraulic structures using soft computing methods. Soft Comput 25(5): 3873-3888. https://doi.org/10.1007/s00500-020-05413-6
27. ASCE (2000). Hydraulic modeling, Concepts and practice. Task Committee on Hydraulic Modeling, Environmental and Water Resources Institute, ASCE, Edited by R. Ettema, MOP 97. https://doi.org/10.1061/9780784404157
28. Govinda Rao N.S., Rajaratnam N., (1963). The Submerged Hydraulic Jump. J Hydraul Div, 89(HY1): 139-162. https://doi.org/10.1061/JYCEAJ.0000822
29. Chow V.T., Open Channel Hydraulics. McGraw-Hill, New York, U.S.A., 680 p, 1959.
30. Ferreira C. (2001). Gene expression programming: a new adaptive algorithm for solving problems. Complex Systems, 13(2): 87-129.
31. Ferreira C., Gene expression programming: mathematical modeling by an artificial intelligence. 2nd edition, Springer, Berlin, Germany, 480 p, 2006. https://doi.org/10.1007/3-540-32849-1
32. Bagherzadeh M., Mousavi F., Manafpour M., Mirzaee R., Hoseini K., (2022). Numerical simulation and application of soft computing in estimating vertical drop energy dissipation with horizontal serrated edge, Water Supply 22(4): 4676-4689. https://doi.org/10.2166/ws.2022.127.
33. Teodorescu L., Sherwood D., (2008). High energy physics event selection with gene expression programming. Comput Phys Commun 178(6): 409–419. https://doi.org/10.1016/j.cpc.2007.10.003
34. Kamari A., Sattari M., Mohammadi A.H., Ramjugernath D., (2016). Rapid method for the estimation of dew point pressures in gas condensate reservoirs. J Taiwan Inst Chem E 60: 258–266. https://doi.org/10.1016/j.jtice.2015.10.011
35. Breiman L., (2001). Random Forests. Mach Learn 45(1): 5–32. https://doi.org/10.1023/A:1010933404324
36. Lotfirad M., Esmaeili-Gisavandani H., Adib A., (2022). Drought monitoring and prediction using SPI, SPEI, and random forest model in various climates of Iran. J Water Clim Change 13(2): 383-406. https://doi.org/10.2166/wcc.2021.287
37. Friedman J.H., (1991). Multivariate adaptive regression splines. Ann Stat 19(1): 1-67. https://www.jstor.org/stable/2241837

© 2024 by the authors. Licensee SCU, Ahvaz, Iran. This article is an open access article distributed under the terms and conditions of the Creative Commons Attribution 4.0 International (CC BY 4.0 license) (http://creativecommons.org/licenses/by/4.0/).

Journal of Hydraulic Structures
J. Hydraul. Struct., 2024; 10(3):72-89
DOI: 10.22055/jhs.2024.46112.1287



OPEN ACCESS

Hydraulic performance evaluation of head works using FLOW 3D

Mukesh Raj Kafle [1]

Abstract

This paper evaluates the hydraulic performance of barrage and under-sluice of Sunkoshi-Marin diversion head works. The numerical simulation was carried out based on the conceptual design of hydraulic structures using FLOW 3D. Velocity vectors, pressure profiles, entrained air volume for barrage and under-sluice were assessed and evaluated. The average velocity over the barrage crest was observed more than 9 m/s at full gate opening. The maximum flow velocity at stilling basin and throughout the longitudinal profile were observed around 10 m/s was 16.90 m/s respectively. There was no sign of negative pressure formation throughout the profile. The minimum pressure observed was 101.356 KPa downstream from diversion axis, along the free surface elevation. Therefore, the structure would be free from cavitation phenomenon. The discharging capacity at FSL with simultaneous operation of barrage and under-sluice bays was assessed as 10,086 m3/s. The flood corresponding to 100 years return period equivalent to 9,241 m3/s easily passes with headwater level being lower than FSL. Further, the extreme discharging capacity of the head works for headwater level 479.5 masl was found 16,547 m3/s. Therefore, deck level adopted as 481.00 masl would be sufficient to release 10,000 years flood.

Keywords: CFD, FLOW 3D, FSL, Head Works, Under-Sluice, Sunkoshi-Marin.

Received: 11 February 2024; Accepted: 03 June 2024

[1] Department of Civil Engineering, Institute of Engineering, Pulchowk Campus, Nepal. E-mail: mkafle@pcampus.edu.np **(Corresponding Author)**

CC BY

1. Introduction

Nepal is shifting to agricultural modernization. This needs for more diversified and efficient irrigation infrastructure. In addition to infrastructures, water deficiency is a key issue. In this background, Sunkoshi-Marin diversion scheme is proposed to enhance the agriculture modernization and address the water deficiency issue in Madhesh Province of Nepal.

For the multi-purpose project head works are critical hydraulic structures. They should be capable of diverting sufficient river water into conveyance system fulfiling the requirements of multi purpose schemes. These schemes may include irrigation, hydropower and water supply as well [1,2]. Besides, the hydraulic structures should ensure the smooth operation of the system preventing coarser sediment particles into conveyance system and safely bypassing the flood [3,4]. The upstream and downstream water level difference in region of hydraulic structure in the river may create high velocity flow and hydraulic jump resulting scouring downstream the structure. It may threaten the safety of such structures due to anticipated scouring of riverbed and dissipater deformation in the downstream [5]. In addition, the safety of hydraulic structures is a key concern in water resources management. Failing of such structures may invite downstream disasters. Understanding of flow characteristics and its consideration during construction of hydraulic structures is important. Recently, many researchers have been widely used computational fluid dynamic (CFD) techniques as an effective tool to simulate many complicated hydraulic phenomena [6].

In the past, several researchers have investigated the flow characteristics around hydraulic structures in the river. Chanson & Brattberg (2000) studied the energy dissipation associated with hydraulic jump phenomenon [7]. Dhamotharan et al. (1981) analyzed flow characteristics in different weir installation using a one-dimensional model [8]. Olsen (1999) used a three-dimensional (3D) model to simulate the Kaligandaki Reservoir flow velocity [9]. Kim (2004) elaborated how the shape of underwater structures influences hydraulic characteristics of river flow [10]. Saad and Fattouth (2017) and Bagheri et al. (2018) discussed hydrodynamic characteristics of flow over circular openings and streamlined weirs respectively [11,12]. Sharafati et al. (2021) developed computational models and empirical equations to evaluate the scour around hydraulic structures [11].

This study investigates the downstream flow characteristics of Sunkoshi-Marin diversion head works with a FLOW 3D model. Overall head works arrangement and capacity are assessed for flood evacuation. Moreover, the hydraulics of barrage and under-sluice structures is investigated and rating curve is generated.

2. Study area

Sunkoshi - Marin Diversion Multipurpose Project (SMDMP) is proposed as a run-of-river basin diversion scheme planned mainly to provide irrigation facilities in the command area of Madhesh Province covered by Bagamti irrigation scheme. The project aims to augment water at the head reaches of Bagmati Irrigation scheme by diverting water from Sunkoshi into Bagmati River through Marin Khola, a major tributary of the Bagmati River. The project covers the area between 490 m and 390 m above mean sea level geographically. The head works site is located in the Lesser Himalayan zone of eastern Nepal. Its location is at Khurkot VDC of Sindhuli district, Bagmati Province (Figure 1, Figure 2).



Figure 1. Sunkoshi - Marin headworks site at Khurkot

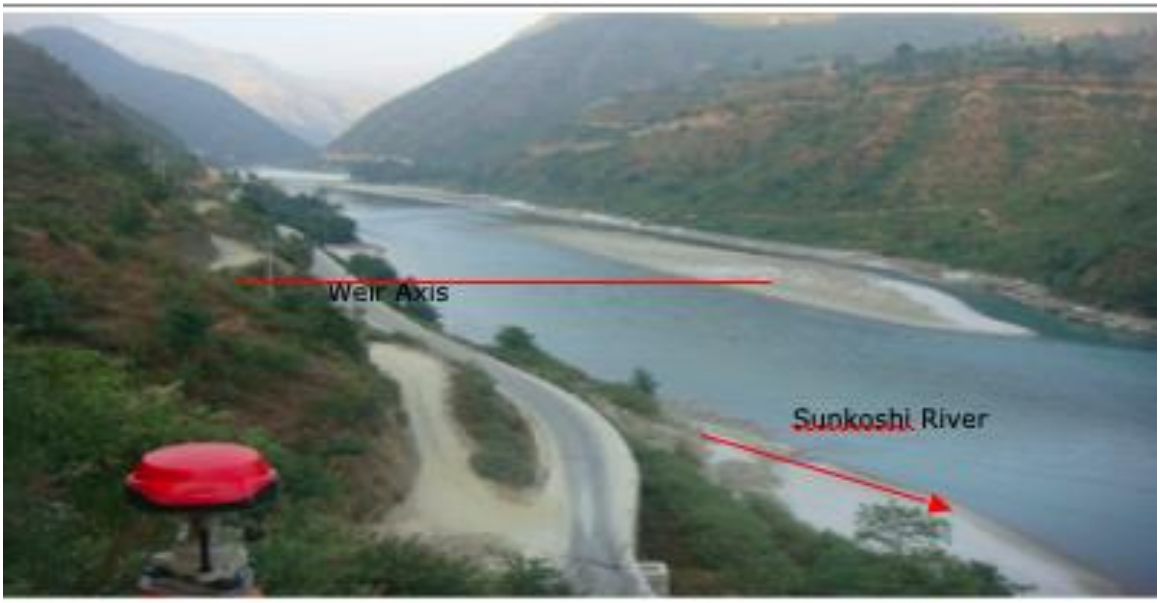


Figure 2. Weir axis at head works site

3. Methodology

A high-precision CFD model FLOW-3D was selected for numerical analysis. A model was then constructed for barrage and under-sluice. Flow characteristics downstream the head works were analysed based on the boundary and operating conditions of barrage and under-sluice. Methodology of the study incorporates the steps as discussed below.

3.1 FLOW 3D

Flow-3D is a powerful numerical modelling software, capable of solving a wide range of fluid flow problems. A good selection of different options across the entire Flow-3D graphical user interface allows the software to be applicable to such a wide variety of situations. Flow-3D allows either one or two fluid flow, with or without a free surface, and a multitude of available physics options to suit the specific application. Various meshing and geometry options are available including multi-block grids and the ability to draw simple objects in the software or import different forms of more complex geometry or topographic files.

Flow 3D has been designed for the treatment of time dependent (transient) problems in one, two and three dimensions. Steady state results are computed as the time limit of a transient. Because the program is based on the fundamental laws of mass, momentum, and energy. Conservation, it is capable to almost any type of flow process. For this reason, FLOW 3D often referred to as a general purpose CFD solver. The continuity and Renyolds averaged NavierStokes equations is presented as follows:

$$\frac{\partial U_i}{\partial X_i} = 0 \tag{1}$$

$$\frac{\partial U_i}{\partial_t} + U_j \frac{\partial U_i}{\partial_j} = \frac{1}{\rho}\frac{\partial}{\partial X_j}\left\{-P\partial_{ij} + \rho V_T\left(\frac{\partial U_i}{\partial X_j} + \frac{\partial U_j}{\partial X_i}\right)\right\} \tag{2}$$

Where U is the Reynold's- averaged velocity over time t, x is the spatial geometrical scale, ρ is the water density, P is the Renyolds averaged pressure, δ is the Kronecker delta and is the turbulent eddy- viscosity. The turbulence is predicted by the RNG k- model (turbulent kinetic energy k and its dissipation) using the constant empirical values. The pressure is calculated according to SIMPLE method (Semi-Implicit Method for Pressure-Linked Equations)

3.2 Layout of head works

The overall layout of the head works is as shown in Figure 3. The sectional elevation is shown in Figure 4. The head works is a low-head diversion structure and consists of barrage and under-sluice bays and a fish passage in between. The barrage bay includes 6 number of 15 m wide and 14 m high openings, whereas the under-sluice bay includes 2 openings, each 10 m wide and 15 m high. The existing riverbed level is about 459.0 m reduced level, which is adopted as crest level of under-sluice bays. The crest level of barrage bay is adopted one meter higher than that of under-sluice. The full supply level at the head works is 474.0 m. The head works is designed to safely pass 1,000 years return period design flood equivalent to 12,328 m^3/s and checked for 10,000 years return period flood equivalent to 15,630 m^3/s.

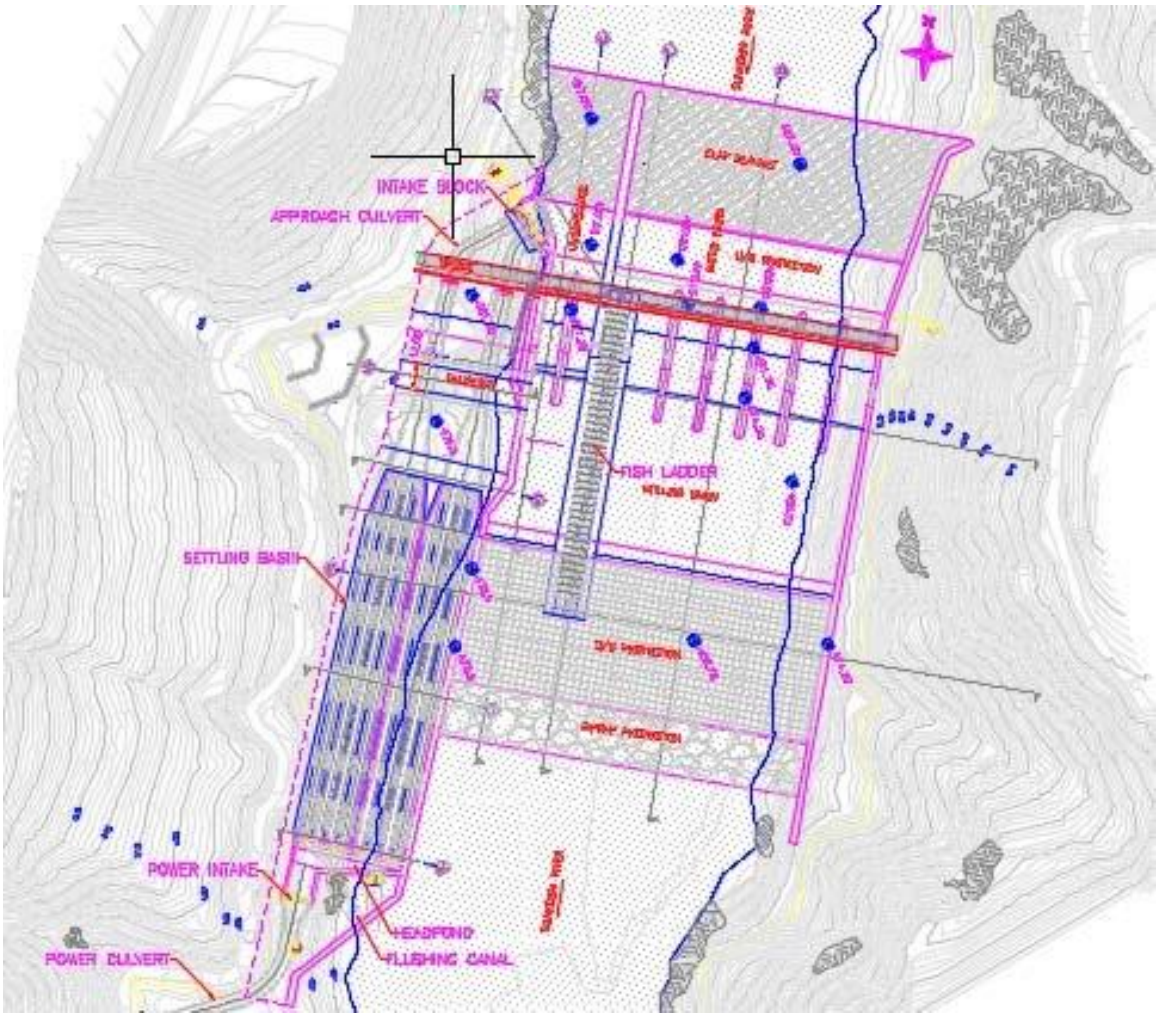


Figure 3. Project layout at head works Area

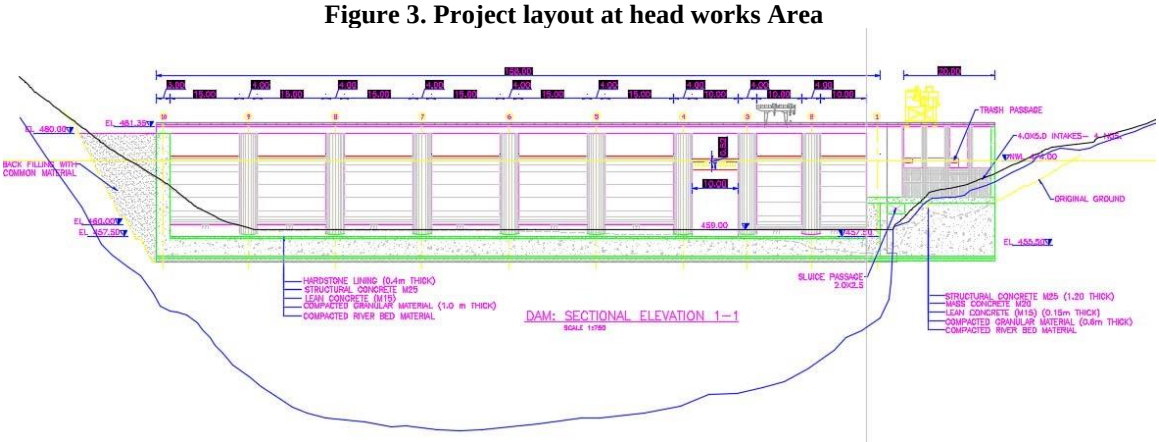


Figure 4. u/s view of dam

Both the openings barrage and under-sluices are equipped with radial gates. The arrangement of under-sluice and barrage is presented in Figure 5.

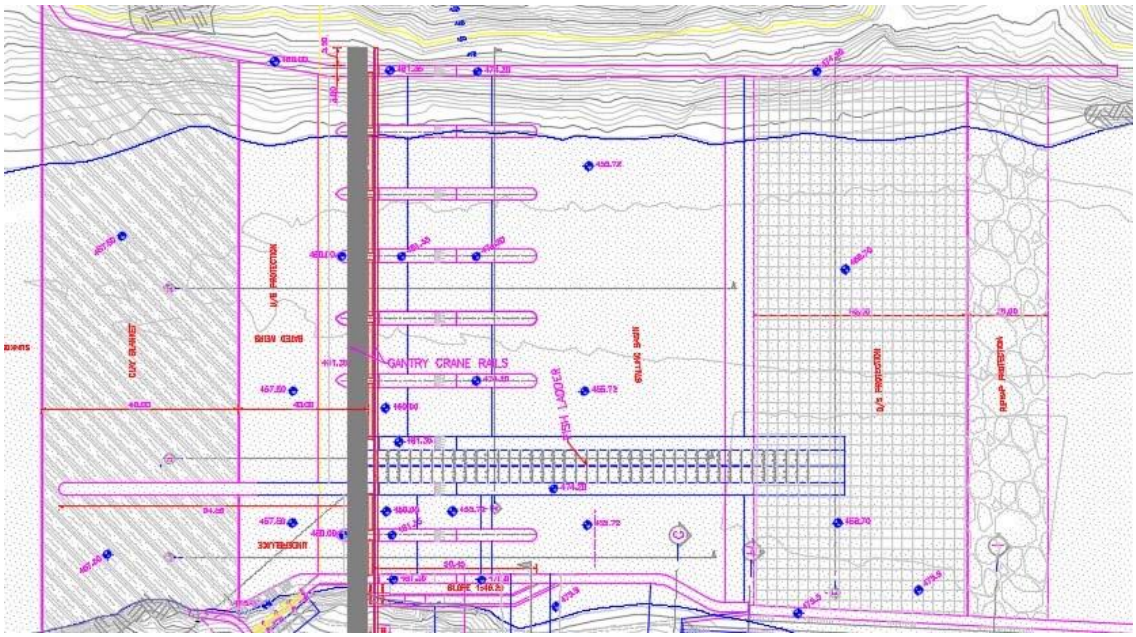


Figure 5. Plan of under-sluice and barrage

3.3 Model Setup

The 3D geometry of head works is prepared with under-sluice and barrage structure incorporating up to the stilling basin. The opening of each barrage and under-sluice is assigned with flux surface namely B1, B2, B3, B4, B5, B6 and U1, U2 respectively from right to left bank. Additional flux surface are defined at upstream face of weir axis and stilling basin. The probes are assigned along the under-sluice and barrage profile for velocity and pressure measurements (Figure 6).

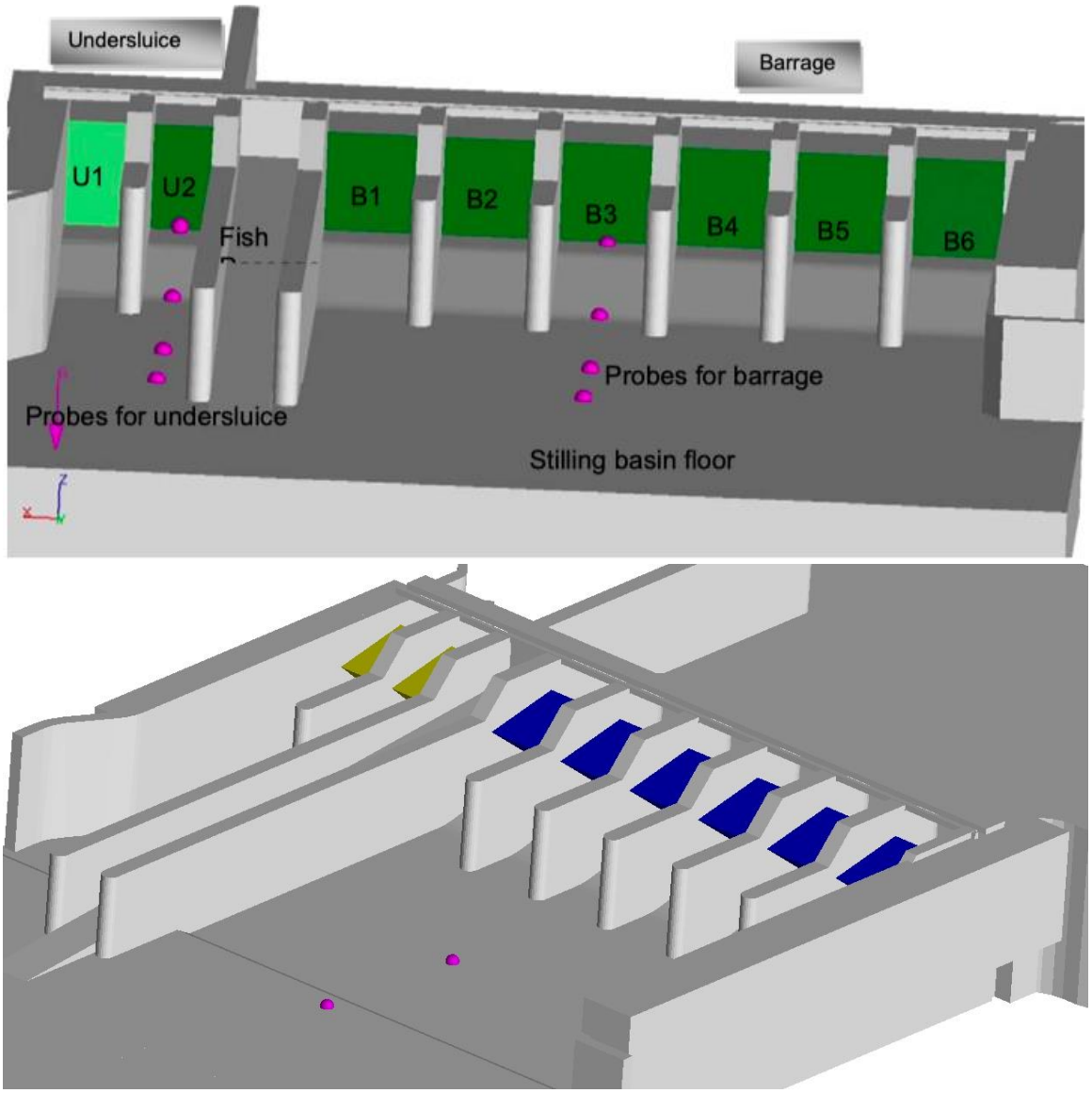


Figure 6. 3D model setup of barrage and under-sluice

Rectangular (2D) and hexahedral cells (3D) for structured and orthogonal grid are used. The non-adaptive grid is immovable during calculation. The geometry and water border is defined by Fractional Area Volume Obstacle Representation (FAVOR) method. The number of cell is adopted according to the objective of simulation (Figure 7).

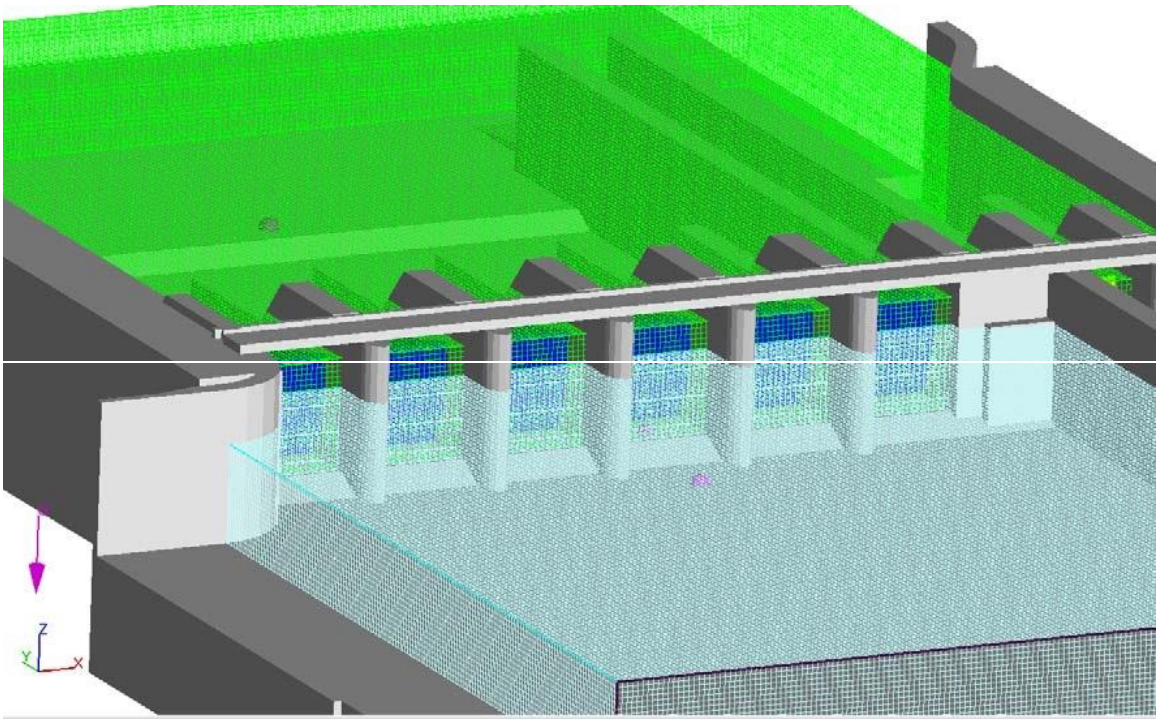


Figure 7. Meshing for Under-sluice and Barrage Modelling

3.4 Boundary and Initial Conditions

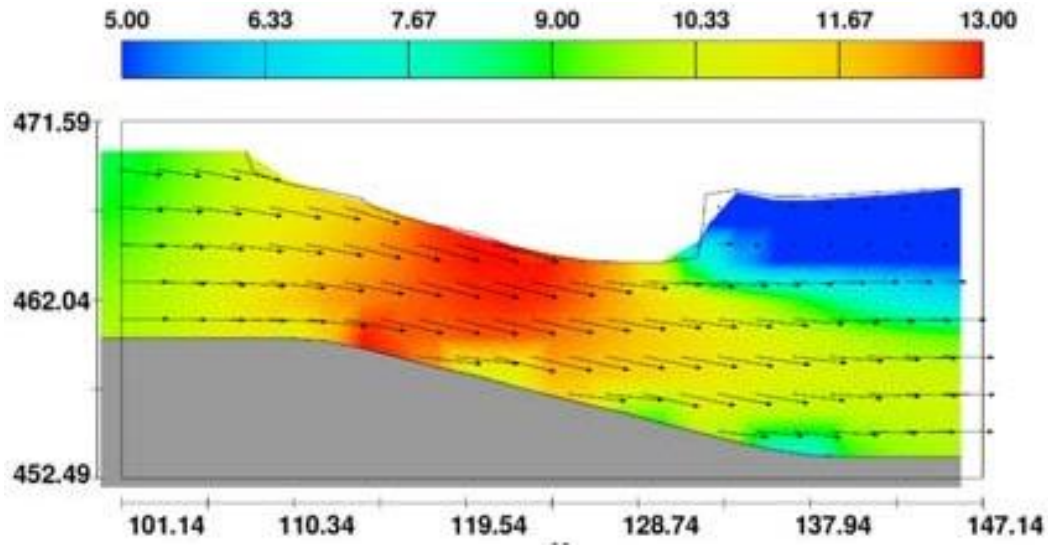
Computational domain with different mesh size is divided into two zones. These zones are sequential having overlapping boundaries. This enables faster computation avoiding the time step limitation. Specified pressure is set as inlet condition. Outflow is set as the downstream boundary. Inlet and outlet boundary conditions are set as continuative to allow water infiltration. The modelled top surface is assigned a specified pressure and rest of the boundary is set as symmetry.

4. Results and discussions

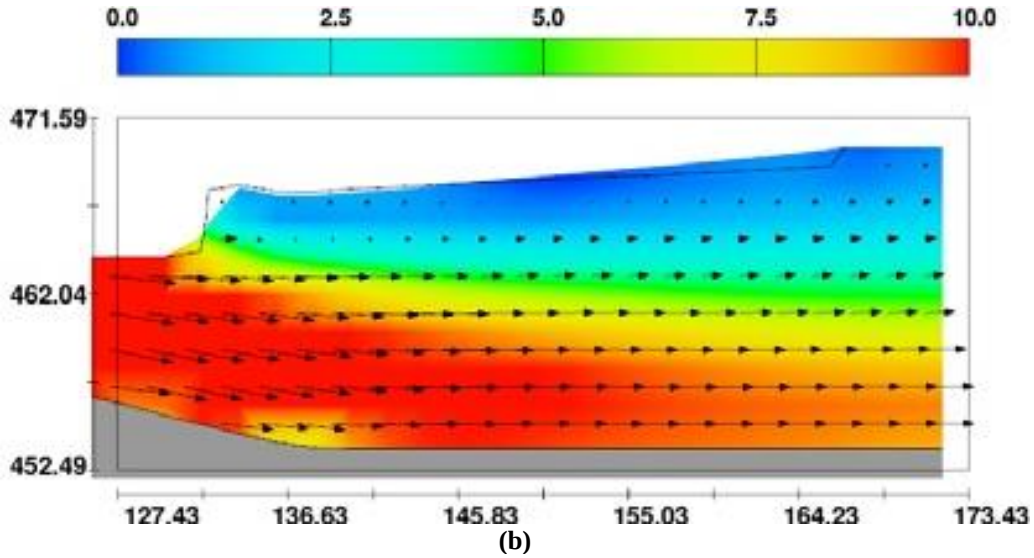
The results of the analysis for each barrage and under-sluice bay are presented below.

4.1 Velocity profiles

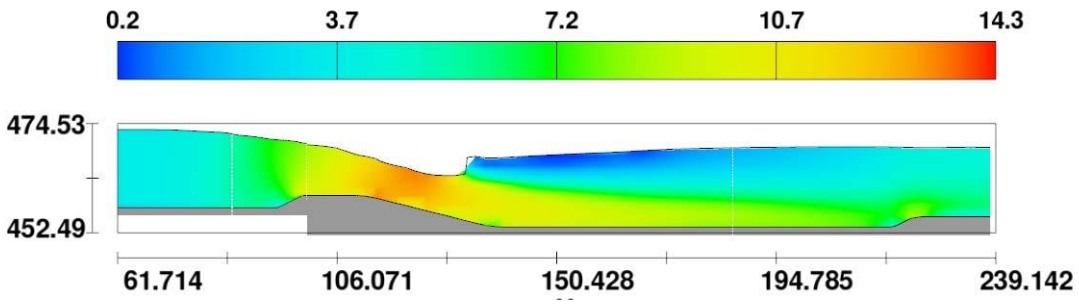
The proposed barrage assumes to regulate the reservoir level mostly at FSL and to release excess water including hazard floods. The velocity profile across the barrage bay at crest level is provided in Figure 8 (a). The average velocity over the crest is observed more than 9 m/s at full gate opening. The maximum flow velocity at stilling basin is around 10 m/s as shown in Figure 8 (b). The velocity magnitude contours along the barrage profile is presented in figure 8 (c).



(a)



(b)



(c)

Figure 8. Velocity Vector a) at crest b) at start of stilling basin c) along barrage Profile

The velocity contour for headwater elevation at 479.50 m is presented in Figure 9. The elevation of trunnion axis of radial gate is below the maximum water surface elevation for headwater elevation at 479.50 m. The maximum velocity observed throughout the longitudinal profile is 16.90 m/s.

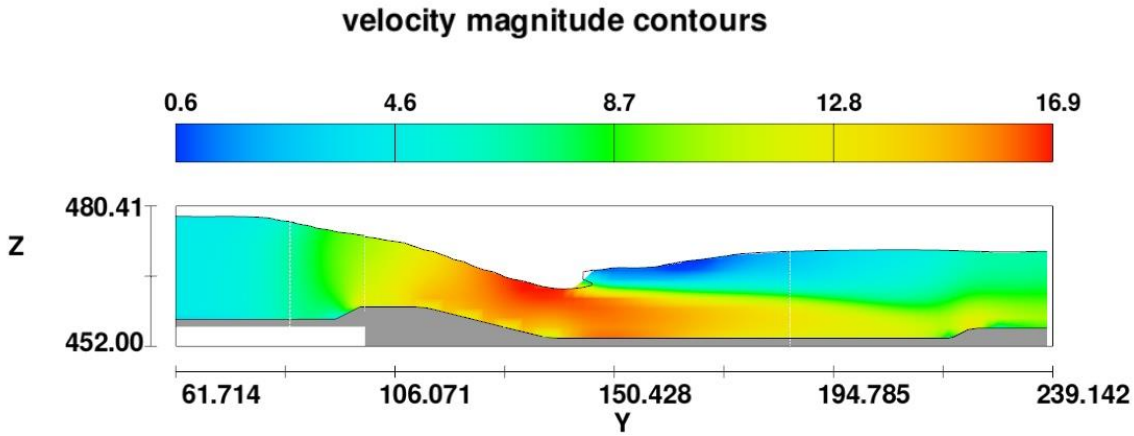


Figure 9- Velocity Magnitude (m/s) along the barrage profile at 479.5 m (Z- elevation, m and Y-distance, m)

The crest level of the double bay under-sluice is lower by 1.0 m compared to that of the barrage bay. The bays equipped with radial gates are designed to flush the sediment accumulated near the intake area and regulate the reservoir level at FSL. Like the barrage bays, they also release excess flow including hazard floods as well. The simulation is done to determine the velocity profile along the under-sluice profile. The average velocity over crest is observed more than 9 m/s at full gate opening.

The velocity magnitude profiles along the flow direction are shown in figure 10 (a). The maximum velocity observed throughout the longitudinal profile is 13.3 m/s. The velocity vector at the crest level at the under-sluice is observed 13 m/s (Figure 10 b). The maximum flow velocity at stilling basin is around 10 m/s (Figure 10 c).

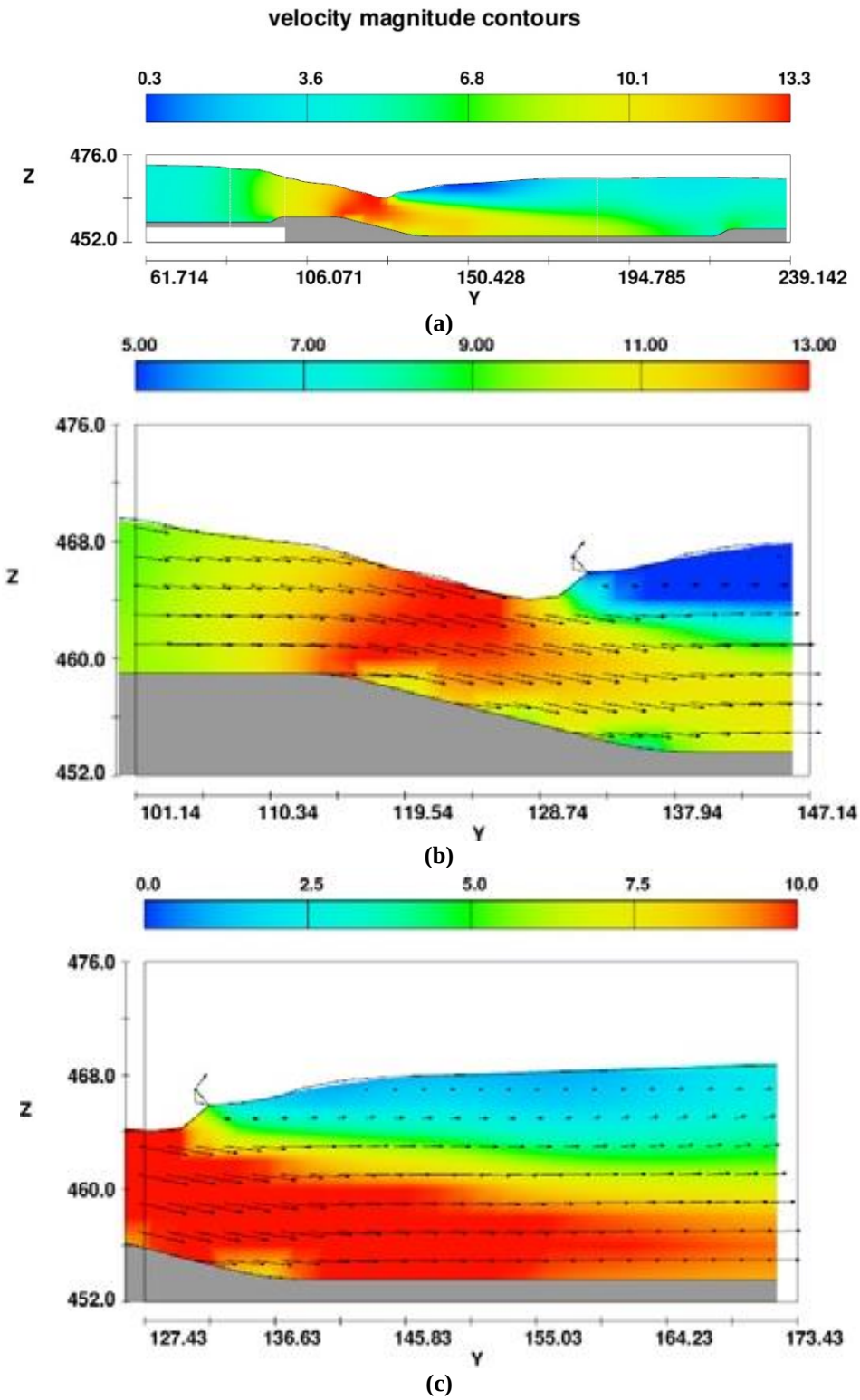


Figure 10. Velocity vector in under-sluice a) along the flow direction b) at crest c) at stilling basin

4.2 Pressure profiles

The pressure contours for FSL operation of barrage is presented in Figure 11. There is no sign of negative pressure formation throughout the profile. The minimum pressure observed is 101.356 KPa downstream from diversion axis, along the free surface elevation. Therefore, the structure will be free from cavitation phenomenon.

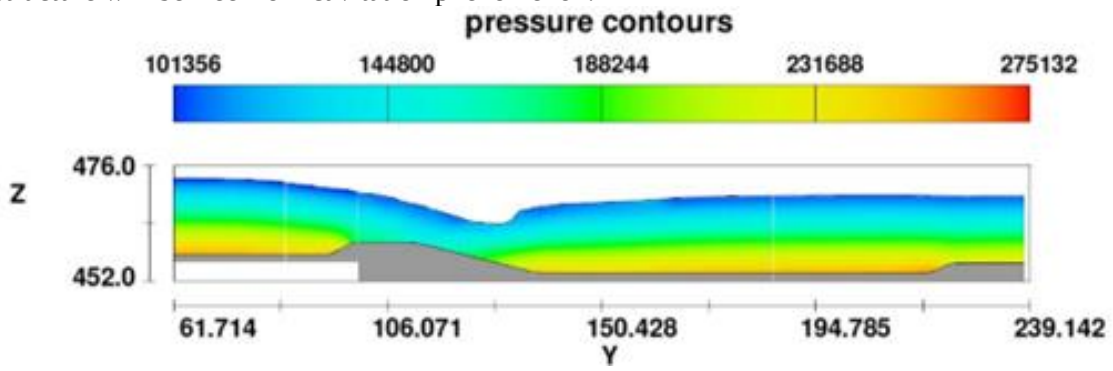


Figure 11. Pressure contours along the barrage profile for FSL operation

The pressure contours for FSL operation of under-sluice is presented in Figure 12. There is no issue with negative pressure formation throughout the under-sluice profile. The minimum pressure observed is 101.555 KPa throughout the free surface elevation.

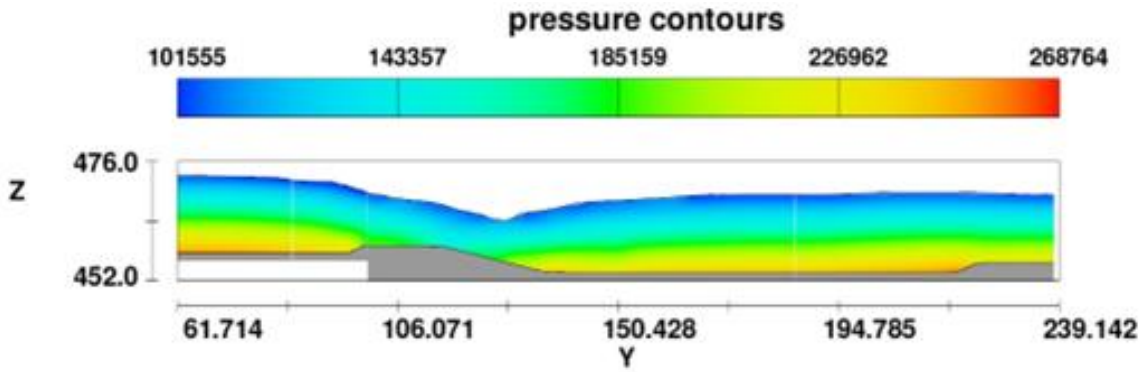


Figure 12. Pressure Contours along the under-sluice

4.3 Entrained air volume

The air entrainment starts at the start of stilling basin. The plot of entrained air volume fraction with fluid across the barrage bay with range from [0-0.05] is presented in Figure 13. The entrained air occupies stilling basin from the start to end.

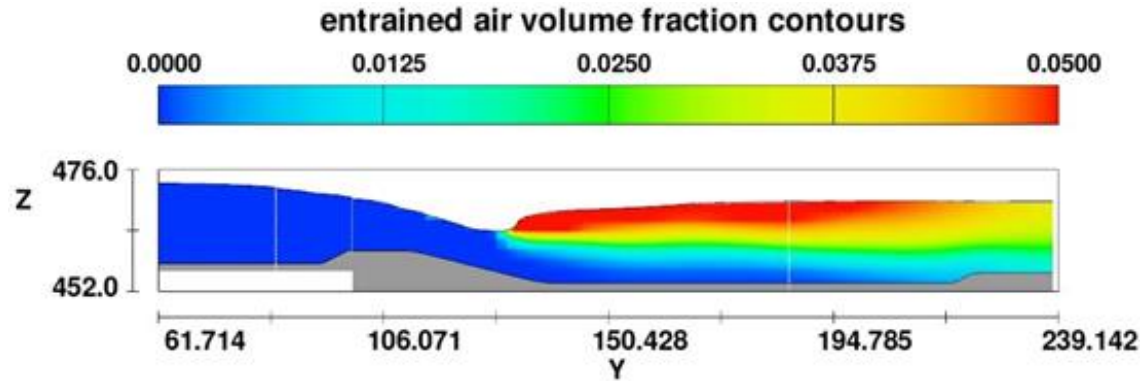


Figure 13. Entrained air volume fraction along the barrage profile

The air entrainment in under-sluice starts at the start of stilling basin. The plot of entrained air volume fraction with fluid along the longitudinal profile with range from [0-0.05] is presented in Figure 14. The entrained air occupies stilling basin from the start to end. Further downstream, air volume reduces to 50%.

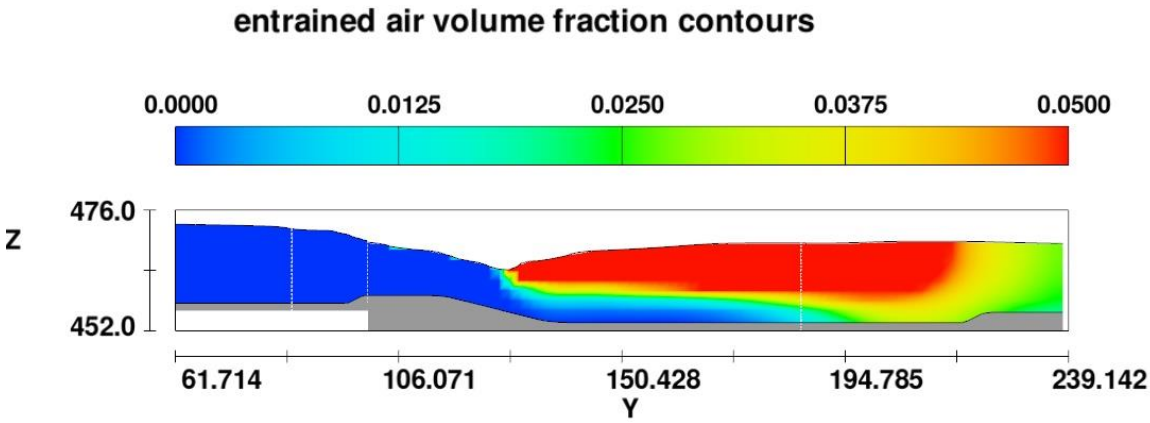


Figure 14. Entrained air volume fraction of under-sluice profile with FSL at 474.0 masl

4.4 Free surface profiles

The free surface profile with respect to bottom profile at different headwater elevation is presented in Figure 15. It can be observed that the hydraulic jump moves further upstream when the headwater is increased from 470.0 m to 474.0 m. In contrast, the hydraulic jump moves further downstream with the increase of headwater from 473.0 m to 478.0 m the jump moves downstream.

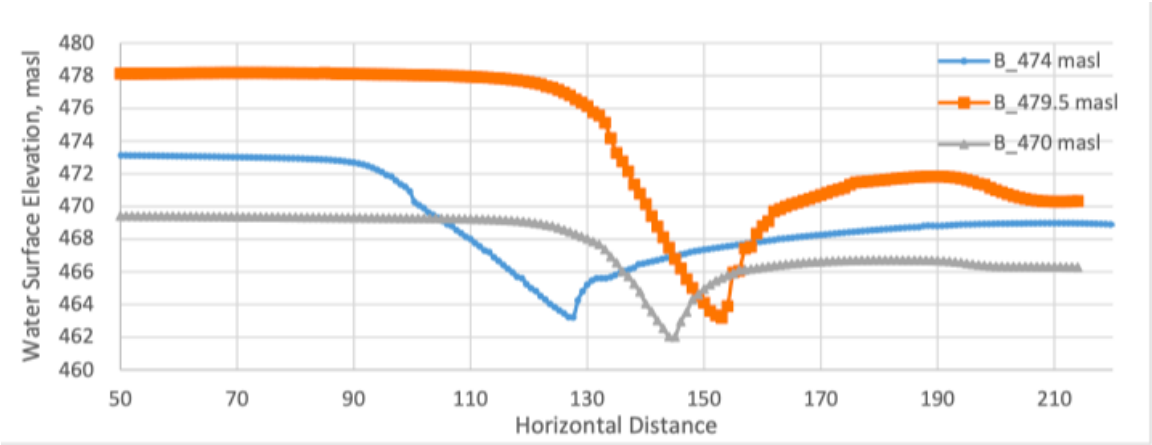


Figure 15. Free surface profile for different design head of barrage

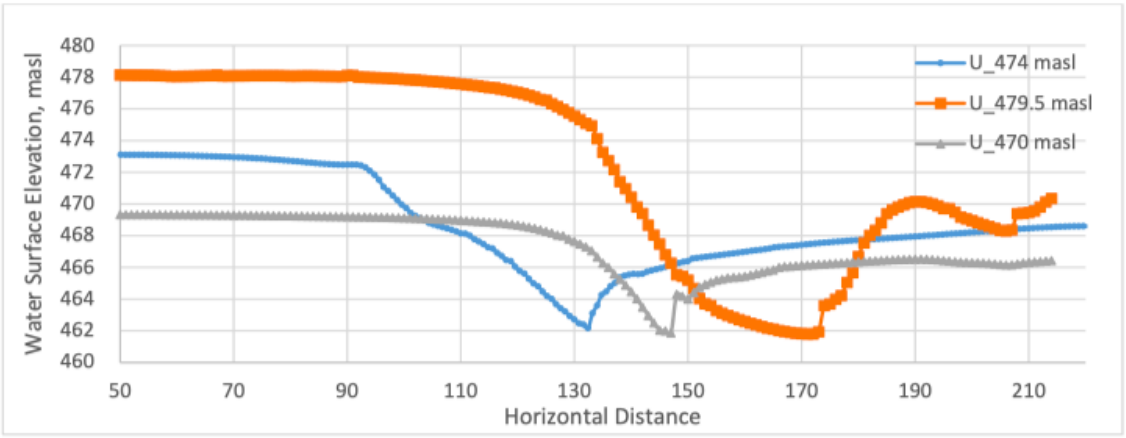


Figure 16. Free surface water profiles for under-sluice at different head water level

4.5 Rating curve

The rating curve for single barrage bay is generated simulating the bay for different head water elevation as presented in Figure 17.

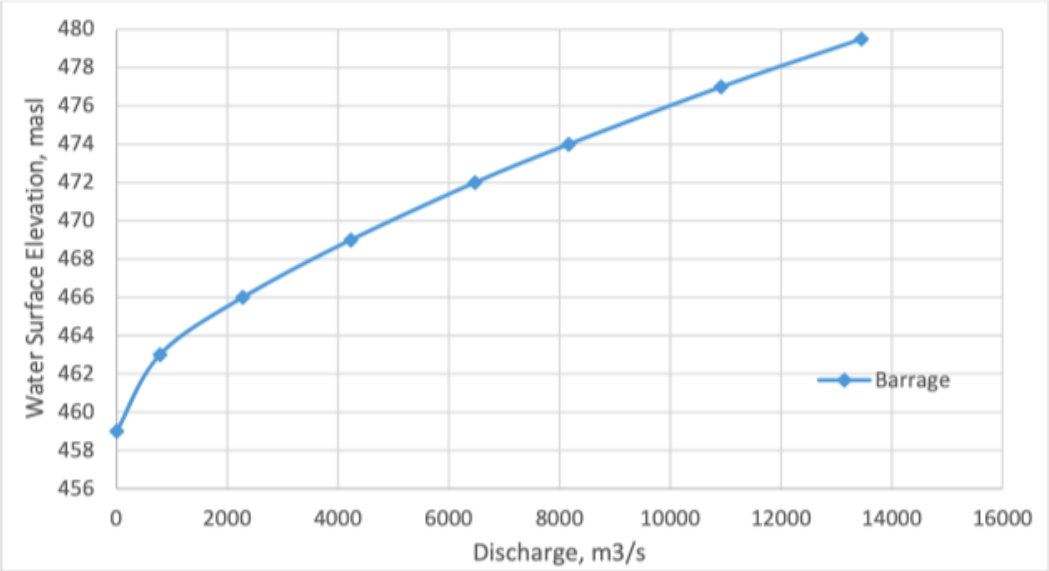


Figure 17. Rating curve of barrage bay under operation

The rating curve for under-sluice is generated and compared with the rating curve generated from 1D hydraulic equation (Continuity and Energy Equation) as shown in Figure 18.

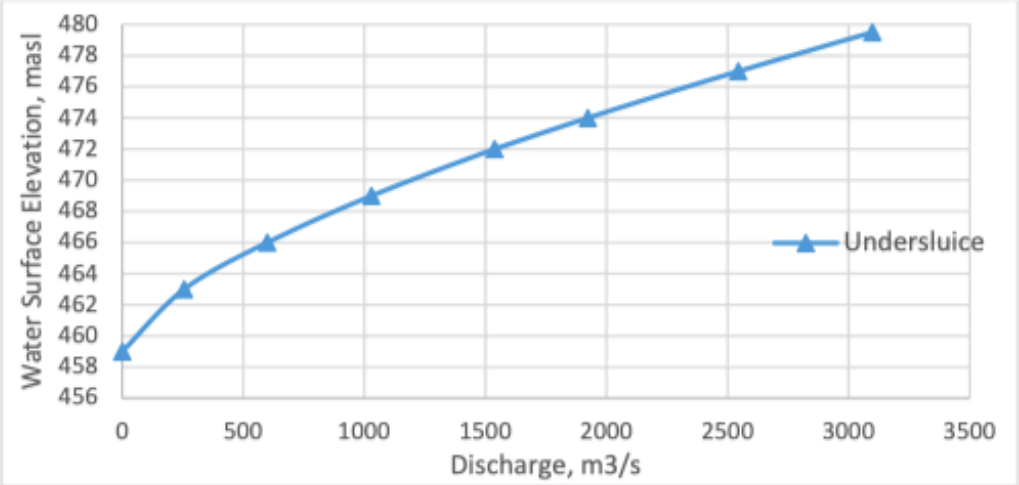


Figure 18. Rating Curve for Under-sluice operation

4.6 Combined operation of under-sluice and barrage

The simulation is used to determine the discharging capacity of head works for the given arrangement. The streamlines under operation are observed for both individual and combined bays. Small modification on the general geometry and arrangement are made to observe final simulation. Then, no local circulation and vortices are observed implying the hydraulic performance of the structure as satisfactory. The streamlines observed for combined operation is shown in Figure 19.

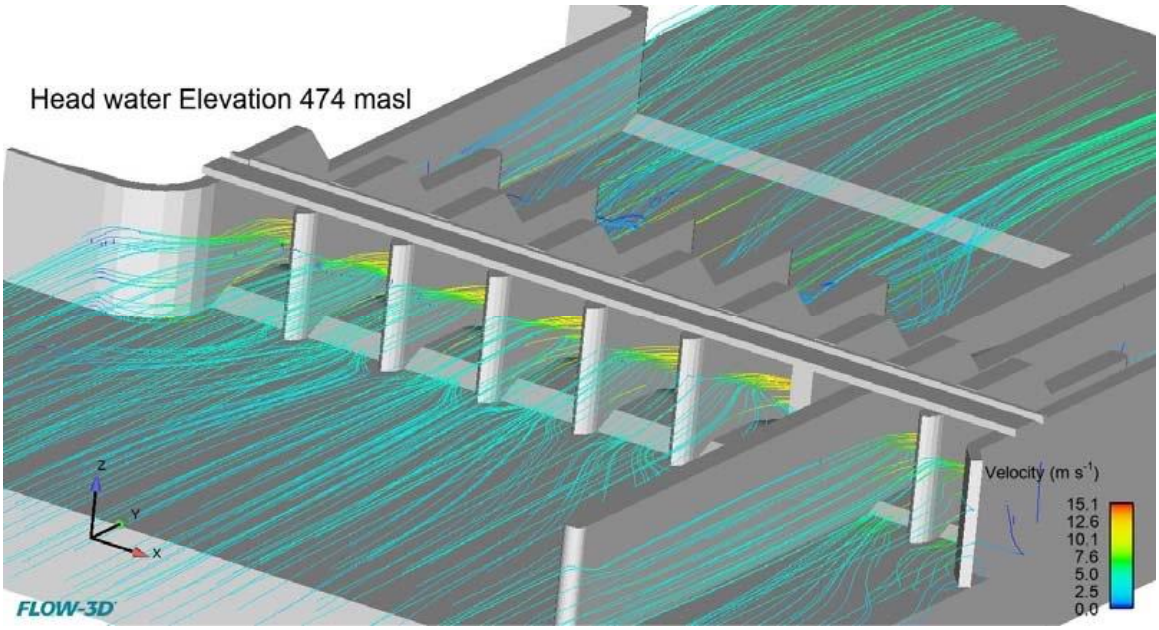


Figure 19. Streamlines from 3D model simulation for overall head works arrangement

The discharging capacity at FSL with simultaneous operation of barrage and under-sluice bays is assessed as 10,086 m^3/s. The flood corresponding to 100 years return period is 9,241 m^3/s and hence easily passes with headwater level being lower than FSL. Further, the extreme discharging capacity of the head works for headwater level as 479.5 masl is also assessed and found as 16,547 m^3/s. Therefore, deck level adopted as 481.00 masl will be sufficient to release 10,000 years flood.

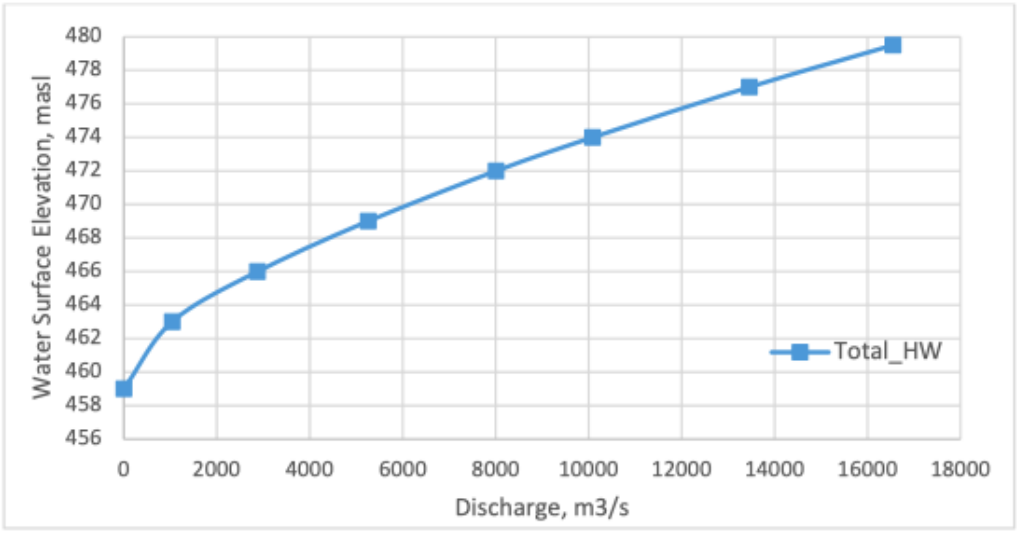


Figure 20. Rating Curve of Head works arrangement

5. Conclusions

FLOW 3D was capable of simulating and evaluating the hydraulic performance of barrage and under-sluice as well. The simulation was carried out based on the conceptual design of hydraulic structures. The proposed barrage assumes to regulate the reservoir level mostly at FSL and to release excess water including hazard floods. The average velocity over the barrage crest was observed more than 9 m/s at full gate opening. The maximum flow velocity at stilling basin was around 10 m/s. The maximum velocity observed throughout the longitudinal profile was 16.90 m/s. There is no sign of negative pressure formation throughout the profile. The minimum pressure observed was 101.356 KPa downstream from diversion axis, along the free surface elevation. Therefore, the structure would be free from cavitation phenomenon. It could be observed that the hydraulic jump moves further downstream with the increase of headwater. Further, deck level adopted as 481.0 masl would be sufficient to release 10,000 years return period flood. The produced rating curve for both barrage and under-sluice operation will be helpful in the operation and safety of barrage after placement.

This study simulates the barrage and under-sluice using FLOW 3D in the given environment and assess the performance of the structures. However, the real structures are often planned in a complex environment, where orientation of the structure, river morphology, hydraulic profiles of structures, upstream and downstream conditions play a vital role. Often flow streamlines are not witnessed as expected resulting in circulation and vorticity around the structures leading to sometimes instability of structures in some cases and lower capacity of the structures or both in other cases.

Funding: This research was self funded.
Acknowledgments: I extend my sincere thanks to Departmrnt of Irrigation, Nepal for providing necessary data and reports.
Conflicts of Interest: The author declares no conflict of interest.

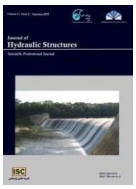
References

1. Goel, A.; Pillai, N.N (2008). A flowmeter for rectangular irrigation field channels. Water Manag. 161, 135–139.
2. Khater, A.; Kitamura, Y.; Shimizu, K.; Abou El Hassan, W.; Fujimaki, H. (2015). Quantitative analysis of reusing agricultural water to compensate for water supply deficiencies in the Nile Delta irrigation network. Paddy Water Environ. 13, 367–378.
3. Outeiro, J.C.; Umbrello, D.; M'saoubi, R. (2006). Experimental and numerical modelling of the residual stresses induced in orthogonal cutting of AISI 316L steel. Int. J. Mach. Tools Manuf. 46, 1786–1794.
4. Qiao, Q.; Li, C.G.; Jing, H.F.; Huang, L.X.; Yang, C. (2021). Impact of an artificial chute cutoff on the river morphology and flow structure in Sipaikou area of the Upper Yellow River. J. Mt. Sci. 18, 16.
5. Kim, B.J.; Hwang, J.H.; Kim, B. (2022). FLOW-3D Model Development for the Analysis of the Flow Characteristics of Downstream Hydraulic Structures. Sustainability 14, 10493. https://doi.org/ 10.3390/su141710493).

6. Le Thi Thu Hien , Duong Hoai Duc. (2020). Numerical Simulation of Free Surface Flow on Spillways and Channel Chutes with Wall and Step Abutments by Coupling Turbulence and Air Entrainment Models. Water 12, 3036; doi:10.3390/w12113036)
7. Chanson, H.; Brattberg, T. (2000). Experimental study of the air–water shear flow in a hydraulic jump. Int. J. Multiph. Flow 26, 583–607.
8. Dhamotharan, S.; Gulliver, J.S.; Stefan, H.G.(1981). Unsteady one-dimensional settling of suspended sediment. Water Resour. Res. 17, 1125–1132.
9. Olsen, N.R.B. (1999). Two-dimensional numerical modelling of flushing processes in water reservoirs. J. Hydraul. Res. 37, 3–16.
10. Kim, K.H.; Choi, G.W.; Jo, J.B. (2005). An Experimental Study on the Stream Flow by Discharge Ratio. Korea Water Resour. Assoc. Acad. Conf. 05b, 377–382.
11. Saad, N.Y.; Fattouh, E.M. (2017). Hydraulic characteristics of flow over weirs with circular openings. Ain Shams Eng. J. 8, 515–522.
12. Bagheri, S.; Kabiri-Samani, A.R. Hydraulic Characteristics of flow over the streamlined weirs. Modares Civ. Eng. J. 2018, 17, 29–42.
13. Sharafati, A.; Haghbin, M.; Motta, D.; Yaseen, Z.M. (2021). The application of soft computing models and empirical formulations for hydraulic structure scouring depth simulation: A comprehensive review, assessment and possible future research direction. Arch. Comput. Methods Eng. 28, 423–447.

© 2024 by the authors. Licensee SCU, Ahvaz, Iran. This article is an open access article distributed under the terms and conditions of the Creative Commons Attribution 4.0 International (CC BY 4.0 license) (http://creativecommons.org/licenses/by/4.0/).

Journal of Hydraulic Structures
J. Hydraul. Struct., 2024; 10(3): 90-118
DOI: 10.22055/jhs.2024.46967.1300



OPEN ACCESS

The influence of the submergence ratio of submerged vanes on the slope of the hole around the pier groups in a sharp bend

Neda Safaripour[1]
Mohammad Vaghefi[2]
Amin Mahmoudi[1]

Abstract

Bridges are metal or concrete structures, which make road connections across rivers when installed over river paths. When flooding or scouring occurs, several issues including bridge destruction and interruption of road connections arise. There are a variety of methods of protecting such structures, one of which is application submerged vanes. This research shows how two vanes with different submergence ratio affected decrease in local scour surrounding one pier and groups of piers installed in a 180-degree bend. The scour around pier groups either in a transverse position to the flow or with a longitudinal direction was analyzed. This finding suggested that applying vanes decreased the deepest scour around the piers in all the tests, and its maximum effect occurred in triad longitudinal pier groups. By raising the submergence ratio, bed scour depth at the outer bank reached its minimum size in longitudinal pier groups. In transverse pier groups, the first scour hole near the outer bank increased in depth in the presence of vanes. By using the vanes, the slope of the scour hole towards the inner bank grew larger than that towards the other bank. The maximum slope of the outer bank happened in the triad transverse pier group at an approximate value of 0.63. The most significant impact of submerged vanes on reducing the upstream slope was observed in a single pier with 75% submerged vanes and triad longitudinal piers with 25% submerged vanes, resulting in reductions of about 50 and 74% respectively compared to piers without vanes.

Keywords: Local scour; Pier Groups; Submerged Vanes; Topographical changes; 180-Degree Bend

Received: 20 May 2024; Accepted: 12 June 2024

1. Introduction

Human beings have long been forced in some cases to construct bridge piers on natural paths of rivers in order to maintain road connections. Gradually, local scour due to horseshoe and

[1]Department of Civil Engineering, Faculty of Engineering, Persian Gulf University, Bushehr, Iran.
[2] Department of Civil Engineering, Faculty of Engineering, Persian Gulf University, Bushehr, Iran, Email: Vaghefi@pgu.ac.ir **(Corresponding author)**

wake vortices occurring around bridge piers result in bridge destruction. Today, pier groups are widely employed in bridge designs. The flow pattern around pier groups is much more complicated than that of a single pier with a much wider local scour around them. Hydraulic engineers have always made efforts to increase bridge pier lifetime. A great number of strategies, for instance, stabilization of bed soil and reduction of flow velocity applied to bridge piers, have been suggested for scour reduction using protective hydraulic structures. Due to the significant impact of submerged vanes on erosion control and sediment transport changes, numerous researchers have attempted to investigate the influence of these hydraulic structures to mitigate local scour.

Voisin and Townsend [1] examined effective implementation of different parameters of submerged vanes in the bed scouring of a sharp and narrow bend. Their results illustrated that by raising the length of the vanes, scouring was transferred from thalwag to the outer bank and the overall channel bed scour decreased. The findings from Tan et al. [2] regarding the impact of a submerged vane on scouring in a straight channel indicate that the most effective vane height is approximately 2 to 3 times the height of the bed sediments. Ghorbani and Kells [3] conducted their experiments in a straight flume on the effective implementation of one and two submerged vanes in scour reduction at a single pier. As shown by the results of their work, the acting of the double vanes in decreasing scour was more favorable than that of the single vane. Bhuiyan et al. [4] examined their experiments on the scour pattern and meandering river flow pattern and the effective implementation of submerged vane installation in the outer bank scour. The results they obtained by experimenting showed that use of submerged vanes reduced outer bank scour and the scour was transported from the thalwag toward mid-channel.

Azizi et al. [5] carried out an experiment in a straight flume at the edge of different shapes of submerged vanes on reduction of bed topography alterations. The geometry of the vanes was assumed through the experiments in 4 different types, either rectangular or triple-blade, where the leading edge chamfered at 30, 45, and 60-degree angles in proportion to a vertical line. Barani and Shahrokhi Sardo [6] examined the influence of submerged vanes with different curved, flat, and angular shapes on the topography of the channel with two 90 and 180-degree bends. They discovered that the curved vanes were more effective in preventing scouring of the channel bank. Azizi et al. [7] conducted a numerical simulation of scour reduction at a single pier under the influence of submerged vanes in a straight flume. The results of modeling the flow pattern around the pier showed that by increasing the number of vanes from 2 and 4 to 6 and also increasing the angle from 20 to 30 degrees, better performance was achieved in reducing scour around the pier. Vaghefi et al. [8] installed a single bridge pier in a straight flume with two different types of piers, vertical and laterally inclined, and investigated the scour around each under different conditions. Dey et al. [9] performed their experimental research in a 180-degree bent flume so as to reduce bed scour under the influence of the angle of submerged rectangular vanes. Maatooq and Adhab [10] conducted their laboratory research by considering the role of installed submerged vanes on reduction of outer bank scour in a 180-degree channel. According to their research, when the ratio of the space of submerged vanes from the outer bank to the channel width was equal to 0.25, it demonstrated better performance than those at other distances. Laboratory and numerical research of Shabanlou et al. [11] regarding the reduction of a 180-degree bend scour influenced by submerged vanes by changing the Froude number and different parameters of submerged vanes showed that the outer bank scour was directly related to the height of the vanes from the primary bed level. In other words, raising the height of the vanes gave rise to the outer bank scour. Vaghefi et al. [12] studied topography of bed alterations due to placement of triad pier groups in two different directions of flow in different locations of a 180-

degree sharply bent. Biswas and Barbhuiya [13] found that by installing submerged vanes in a line on the outer bank of a 180-degree bend, the submerged vanes could decrease the scour depth of the outer bank by approximately 40%. Zarei et al. [14] studied the performance of various numbers, angles and lengths of vanes on topography of bed in a sharp 180-degree bend. By studying the flow pattern around triangular vanes connected to the outer bank in a rectangular flume, Bejestan et al. [15] demonstrated that submerged vanes tripled kinetic energy compared to a situation where no vanes where used. Safaripour et al. [16] studied scour reduction around pier groups under the implementation of submergence ratio of submerged double vanes in a sharp 180-degree bend. A variety of parameters, including number and different arrangements and directions of the pier group, and the submergence ratio of the submerged vanes were considered. In this research, the bed topography alterations along the bend and the downstream straight path, the scour temporal evolution of variations, the deepest scour, the highest sedimentary bar, the volume of the hole, the area of scour, and the rectangle surrounding the scour hole were investigated. Chooplou et al. [17] examined the different arrangements of double submerged vanes in scouring around a single pier located in a 180° sharp bend. Their findings indicated that positioning the vanes along the central axis of the channel led to an approximately 51% decrease in scour. Keshavarz et al. [18] investigated the effect of collar on reducing scouring of bridge piers. They examined nine different cross-sectional shapes of the pier protected with collar. Vaghefi et al. [19] altered the dimensions and number of submerged vanes to investigate scouring around a single bridge pier in a sharp 180-degree bend. They determined that submerged vanes exhibit positive results, leading to an approximated 30% decrease in scour depth around the bridge pier. Hamidi et al. [20] used a flow-3D numerical model approach to mitigate scour around a bridge pier using double submerged vanes. They found that increasing the height of the vanes above the initial bed led to a reduction in scouring. Safaripour et al. [21] investigated the flow pattern around single and twin pier groups affected by double submerged vanes. They discovered that the submerged vanes diverted the flow from the piers, with the highest velocity occurring near the vanes.

The results of prior research indicated that a combination of submerged vanes and piers in bent paths had rarely been addressed by researchers. This paper aimed to examine the role of submergence ratio of two vanes in scour decrease at one pier and at pier groups in 180-degree sharply bent channels. The pier groups have been installed in transverse or longitudinal directions. In this paper, lateral and longitudinal profiles along the channel, scour hole slopes surrounding the groups of piers, and the scour reduction at the piers were analyzed.

2. Material and methods

All of the tests were conducted in the laboratory of hydraulic structures at Persian Gulf University in Bushehr. A schematic of laboratory channel is shown in Fig. 1(a). The laboratory is equipped with a flow meter, a pump, and a bent flume. The U-shaped laboratory channel, as wide as 100 cm, is constructed with a relative curvature radius of 2 at the bend. The inlet tank is connected to the upstream side of the bend via a 6.5-meter-long straight end. The water flow is led out through an outlet tank located at the end of a 5.1-meter-long downstream end. The height is 70 cm throughout the channel, and 30 cm of this height is covered by d_{50}graded sediments and standard deviation (σ_g) equal to 1.5 mm and 1.14, respectively. According to the recommendation of Raudkivi and Ettema [22], the diameter of the sediment particles should be greater than 0.7, as suggested by Chiew and Melville [23] the geometric standard deviation should be less than 1.3. The shear Reynolds number (Re*) was determined to be 580, indicating turbulent flow, as it exceeded 250.

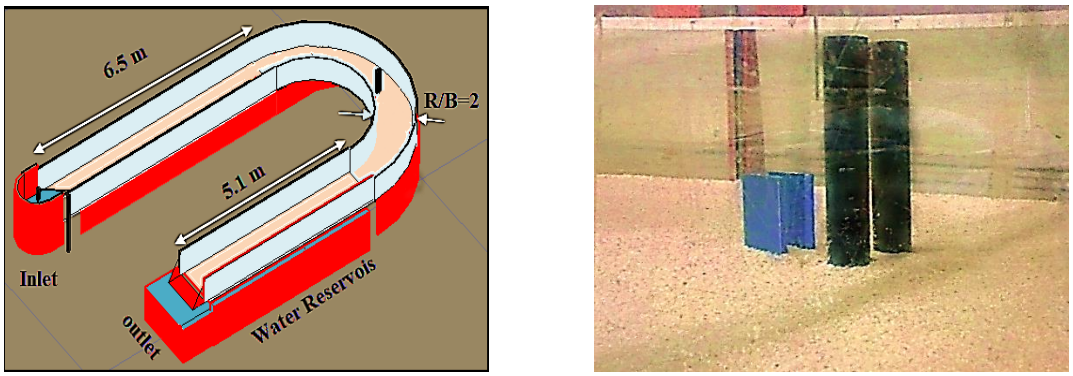


Figure 1. (a) Schematic view of laboratory channel , (b) Installation of piers and vanes

PVC pipes (where D=5 cm for Cylindrical Polyvinyl Chloride) were used to represent the piers. Rectangular Plexiglass vanes with a length of 7.5 cm (1.5 times the diameter of pier) and a thickness equal to 20% of the pier diameter were employed as submerged vanes with 25, 50, and 75% submergence ratios [16]. According to the research of Safaripour et al. [16], submerged vanes were placed upstream side of the piers at an angle of 25 degrees clockwise. Figure 1(b) illustrates a view of piers and vanes installed.

2.1. Description of the Experiments

Twenty experiments were conducted in a 180-degree sharply bent channel. The tests were carried out about one, two and three piers located in transverse or longitudinal directions, with and without the presence of vanes. The groups of piers were installed at a center-to-center space of 2 times the pier diameter from each other in the 90-degree position, located on the central line of the flume. The role of double vanes of varied submergence ratios in scour reduction at bridge pier groups was examined. The experiments were conducted for 25, 50, and 75% submergence ratios (13.5, 9, and 4.5 cm from the primary base level). Parallel arrangement of the vanes was assumed with 100% overlap at a 25-degree clockwise angle. The space between the vanes and the pier was determined to be 2.5 times the pier diameter. First, a 44-hour-long experiment was conducted with a 70-lit/sec discharge and an approximate depth of 18 cm on a single bridge pier in order to determine the te (where te= relative equilibrium time). The deepest scour was written at various intervals. After 9 hours into the experiment, the depth of scour reached 0.9 times the total scour depth; hence, 9 hours was selected as te. During the test, instabilities were observed in the slope of the hole. The slope of the hole was occasionally unstable because of the flow entering it, but the criterion for assessing the slope was complete drainage by the end of the tests. Subsequently, following drainage and throughout the measurements, the slope of the hole remained stable, as there was no flow present.

Experiment appellation denotes the pier properties in the first part and the vane properties in the second part. P represents the piers. The first symbol indicates the number of piers, and L and T denote that the group piers are in longitudinal and transverse direction, respectively. In the second part, S denotes the submerged vane, and the last number implies the submergence ratio. The variable parameters in the experiments are shown in Table 1.

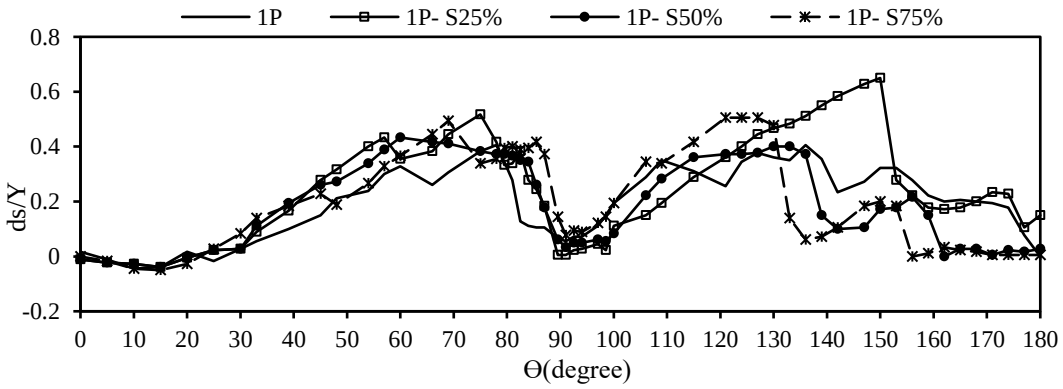
Table 1. Variable parameters in the experiments

Row	The number of piers	submergence ratio of the vanes	placement of piers in two different directions of flow
1	1P, 2P, 3P	25%, 50% , 75%	Longitudinal or Transverse

3. Results

Instances of a few longitudinal profiles along the channel are shown in Fig. 2 for investigating the implementation of the vanes present at the upstream region of a single pier. Figure 2(a) illustrates the longitudinal profile near the inner bank in single pier and tests using vanes. According to this figure, sediment piles have been created in proximity of the inner bank from the beginning to the end of the bend. The height of these piles has been reduced to approximately the same amount as the primary bed level at the center of the bend near the inner bank. According to Fig. 2(a), pile formation at a single bridge pier has an ascending trend through the first half of the bend, increasing after installation of the submerged vanes. Upon reaching the channel center, no piles are developed there. The highest sedimentary bar increased in single pier experiments accompanied by vanes from the 90 to 180–degree positions of the bend. For instance, 1P- S25% had a maximum sedimentation height almost equal to 0.65Y among the experiments.

As is observed in Fig. 2(b) by reducing the submergence ratio in the experiments including vanes, the scour increases at the upstream side of the vanes from the 0 to 90–degree positions of the bend in mid-channel. Sediments in this area oriented towards the inner bank considering the streams inside the bend, the result of which was the increased height of sediment pile in proximity of the inner bank, as is illustrated in Fig. 2(a). As shown in Fig. 2(b), after placement of the submerged vanes, the deepest scour happened at the site of the vanes. A study of the longitudinal profile in mid-channel suggested that the scour about the pier declined when using submerged vanes. It may be concluded that the vanes were capable of reducing wake vortices created at the downstream region of the pier. As is indicated in Fig. 2(b), the flow velocity increased with reduction of water height over pile (Zone 1) in P experiment, which resulted in creation of vortex and scour; therefore, the second scour hole (Zone 2) occurred. In the experiments using vanes, the pile was developed at its downstream side within the approximate distance of 100 to 125 degree angles. Thereafter, topography variations of bed get to the lowest value.



(a)

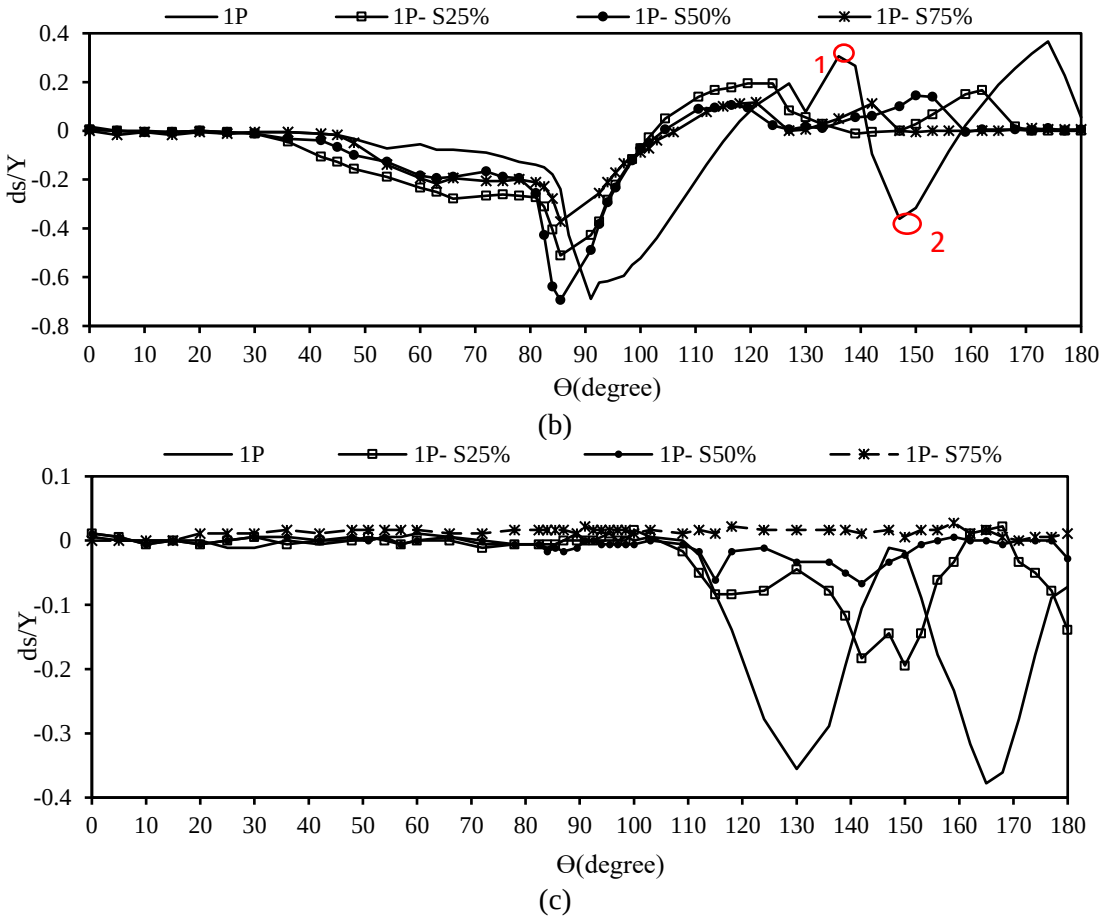


Figure 2. A sample of a longitudinal section at a distance equal to (a) 5, (b) 50, and (c) 95% of the channel width from the inner bank in the single bridge pier experiments with and without submerged vanes

It is obvious in Fig. 2(b), 1P- S75% conditions provided an acceptable performance with the most significant reduction in scour along the channel in comparison to the pier without any vanes. At the downstream region of the piers, after the pier site, the lateral flows inside the bend dragged the sediments from the outer bank towards mid-channel, the event which is verified in Fig. 2(b) and Fig. 2(c). Two consecutive scour holes of almost the same depth happened at approximate spaces of 90 and 110D from the beginning of the bend close to the outer bank in the single pier experiment in Fig. 2(c), and sediments at this area approached mid-channel and created two consecutive piles. It may be observed in Fig. 2(c) in the single pier tests containing two vanes that the longitudinal profile variations at the outer bank decreased when the submergence ratio increased. For instance, it may be stated about 1P- S75% experiment that bed topography at the outer bank underwent almost no significant variations. In 1P- S25%, the scour depth close to the outer bank increased at a space of approximately 40D from 90° position of the bend, and the sediments of this area were driven towards mid-channel.

Figure 3 presents a sample of a few lateral profiles at specific intervals in order to examine bed variations in single pier experiments with submerged vanes. The lateral profile of the single bridge pier in Fig. 3(a) indicates that the scour occurs at a space of approximately 30 to 80% of

B (where B= channel width) away from the inner wall. It may thus be concluded that the flow oriented towards mid-channel. With installation of the vanes in this position as well as reduction of the submergence ratio, the local scour increased.

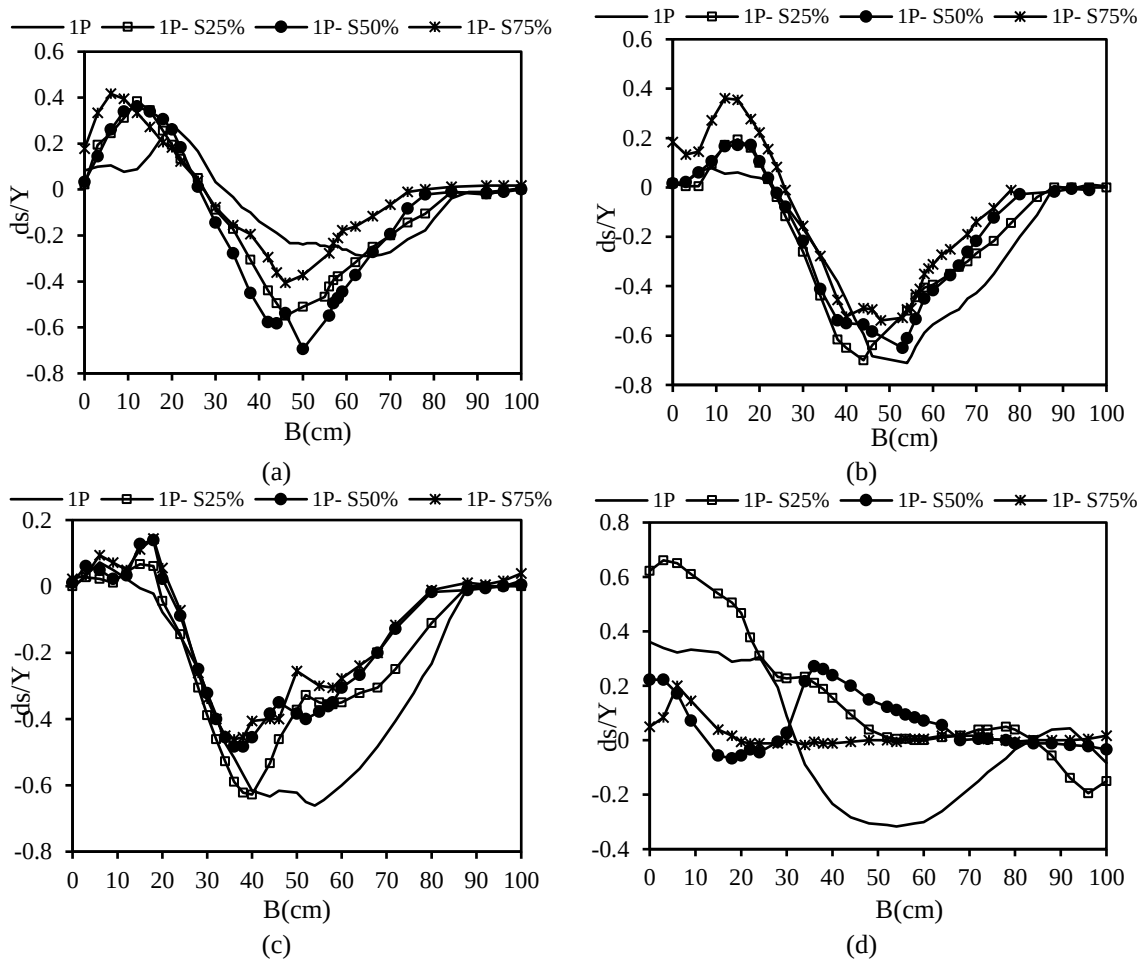


Figure 3. A sample of cross section at a distance equal to (a) 2.5 times the pier diameter towards upstream from the bridge pier location, (b) the center of the pier, (c) 2 times the pier diameter towards downstream from the bridge pier location, and (d) 42 times the pier diameter towards downstream from the bridge pier location in the single bridge pier experiments with and without submerged vanes

As shown in Fig. 3(b), the deepest scour at the location of the pier decreases in experiments containing vanes. For instance, the deepest scour at the location of the pier in 1P- S75% decreased by almost 25% compared to 1P experiment. The slope of the hole is sharper at the inner bank than that at the outer bank at this section. As is observed, increase in submergence ratio reduced the depth of scour at the cross section. Given the fact that the flow was directed by the vanes towards the inner wall, reduction of the submergence ratio increased scour at the inner bank in comparison with a pier in the absence of vanes at this section. The scour at the inner bank in 1P- S75% did not change in comparison to that in a single pier, and the scour at the outer bank decreased by an average of 44% compared to the experiment without vanes. In experiments

accompanied by vanes, the highest sedimentation bar increased, where raising the submergence ratio made further evident such an increase in height of the sediment pile. As it appears in Fig. 3(c), with installation of the vanes in the experiments, bed alterations at a space of 40% of B from the inner bank are the same in every experiment. After that distance, scour decreased by 54% on the average in tests with vanes compared to pier without any vanes. Therefore, it can be concluded that the scour volume decreased with installation of the vanes. The implementation of vanes having an effect on scour depth reduction is observable for 50 and 75% submergence ratios in this figure. According to Fig. 3(d), in the single pier experiment, the amount of scour created at mid-channel is approximately 10D on both sides with the maximum depth of around 0.3Y. Placement of vanes reduced bed scour in comparison to the tests without any vanes, and bed topography variations in 1P- S75% approximately reached the minimum. With reduction of the submergence ratio, the sediment pile was created near the inner bank. The highest pile at this section occurred in 1P- S25% with an approximate value of 0.65Y.

Figure 4 illustrates instances of a few longitudinal profiles at specified intervals in twin pier group experiments. A review of Fig. 4(a) reveals that in the first half of the channel, there are more sediment piles in 2PL than in 2PT since 2PL pier group is longitudinal, and the front pier plays the protective role. Upstream-directed recursive flows in this pier group transported the sediments in this area towards the inner wall of flume. As also indicated in Fig. 4(a), by using the submerged vanes in 2PT, the highest pile at the first half of the flume increased by approximately 1.6 times, and that in the second half increased by approximately 1.3 times in comparison to 2PT test. By using submerged vanes in 2PL pier group, the height of sediment bar barely changed in the first half of the bend; however, it increased by approximately 1.6 times that without vanes at the downstream region of the piers. The maximum sedimentation height at this section in experiments containing vanes was almost equal in both pier groups. As shown in Fig. 4(b), scour is observed in every experiment with vanes at the upstream region of the vanes. In the second half of the bend, there were more sediment piles in 2PT than 2PL because the piers were placed across the channel, which caused an increase in local scour around them, Therefore, the sediments shifted from the proximity of the piers and vanes created a pile in close of the inner bank. The transverse station of the piers to the flow added to the sedimentation height. The sedimentation height also increased in every experiment containing vanes with an approximate value of 0.7Y at a distance of 35D from the center of the channel. In experiments involving longitudinal piers with vanes, the scour pattern was the same for all three submergence ratios of the vanes. Scour depth reached the downstream side of the piers at a mild slope of 0.17 in 2PL, and 0.32 in experiments using vanes. Profile variations at the outer bank are indicated in Fig. 4(c). In this figure, the vanes installed in 2PL experiment reduced bed topography alterations to a minimum. By using the vanes in 2PT experiment, the depth of the first scour hole dropped, while that of the second scour hole climbed on the graph. The deepest scour at this section happened at spaces of 26 and 50D from the center of the channel in 2PT- S50% and 2PT experiments, respectively.

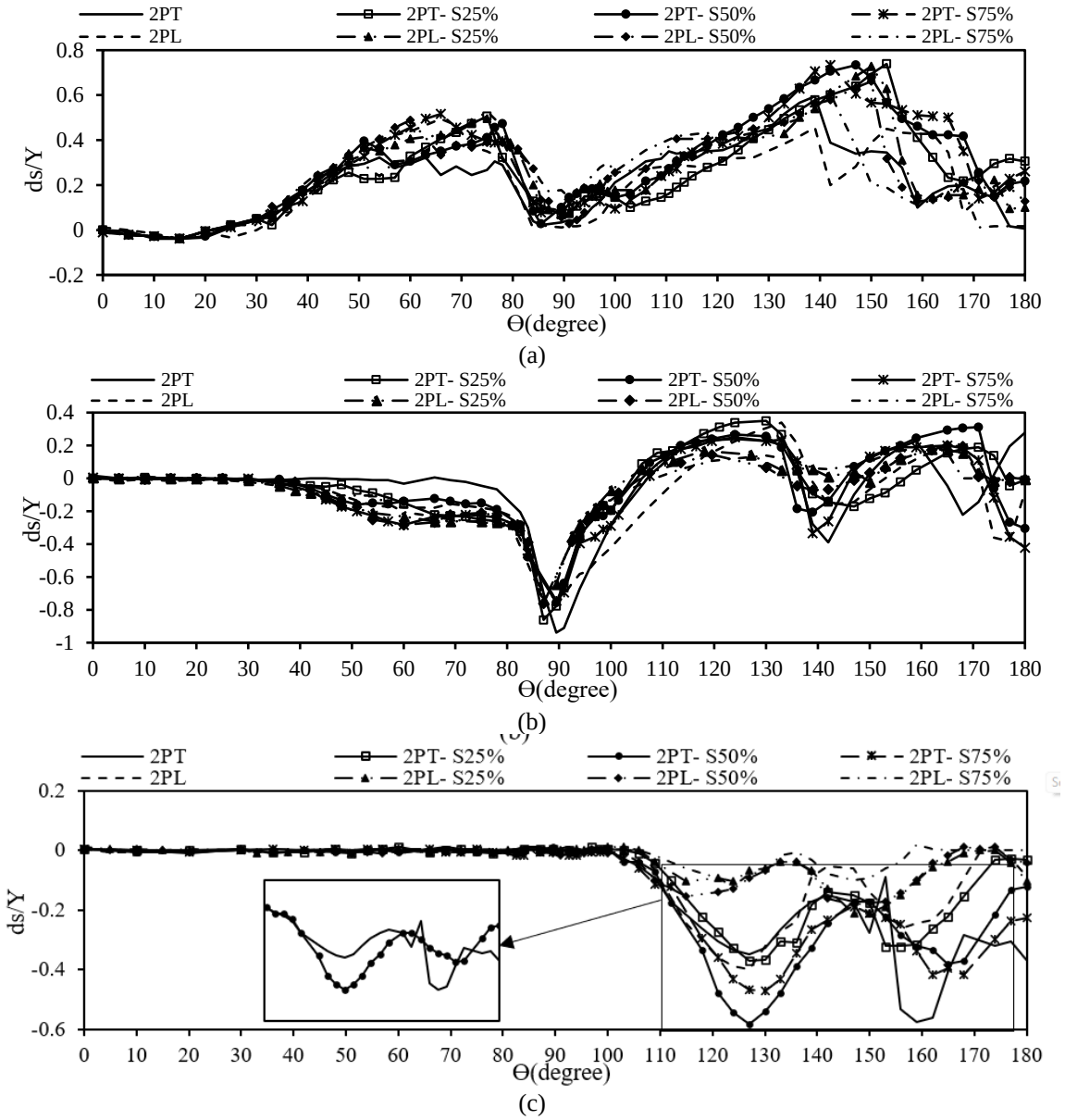
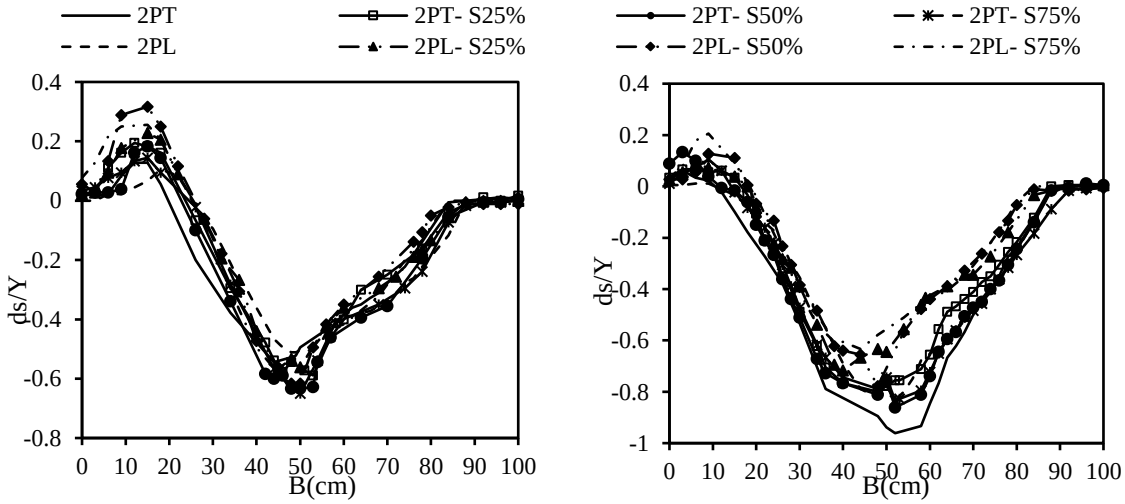


Figure 4. A sample of a longitudinal section at a distance equal to (a) 5, (b) 50, and (c) 95% of the channel width from the inner bank in twin pier groups experiments with and without submerged vanes

Figure 5 illustrates instances of a few lateral profiles in twin pier groups experiments accompanied by double submerged vanes. As shown in Fig. 5(a), in 2PL experiments using the vanes, the scour throughout the width of the section decreased, and the sedimentation height increased up to a space of 20% of B from the inner wall. In 2PT experiments, for every submergence ratio of the vanes, the inner bank scour was reduced, and the outer bank scour reduction happened only in 2PT- S25%. In 2PT- S50% and 2PT- S75% experiments, the lateral profile of the outer bank did not change in comparison to the piers without vanes. In Fig. 5(b), application of double vanes in 2PT has an acceptable performance in reducing scour in this

section. 2PT- S25% experiment reduced scour in channel width by approximately 16% on the average. Installation of the vanes in 2PL experiment did not change the bed lateral profile up to a space of 40% of B from the inner wall, compared to the piers without using vanes; however, after this point, the bed lateral profile decreased by 50% on the average. According to Fig. 5(b), it can be seen that in both groups of piers, changing the submergence ratio leads to almost equal profile variations, i.e. the same performance is observed for every submergence ratio of the vanes. As can be seen in this profile of Fig .5(b), the deepest scour in 2PL- S75% and 2PT- S25% experiments respectively decreased by approximately 30 and 20% in comparison with the test with no vanes. Figure 5(c) illustrates the area behind the piers, where the vanes reduced scour at the outer wall by directing the flow towards the inner wall. In 2PL experiment, at a distance of 60% of B from the inner wall, an average of 50% reduction in scour occurred in comparison with the test using only piers. Considering this profile in 2PT experiments, the depth of scour of the outer and inner banks with the presence of vanes underwent little change; however, the scour depth at a distance of 20% of mid-channel decreased by approximately 28% in comparison to the piers without using vanes. Alterations in the profiles of inner and outer banks in 2PT experiments accompanied by vanes almost complied with those of piers without the vanes. According to Fig. 5(d), sediment pile developed in the twin pier groups near the inner bank, the value of which took a descending trend approaching towards the outer wall. The smallest bed topography alterations occurred in 2PL- S75% experiment. As shown in Figs. 5(c) and 5(d), the lower depth of scouring at the outer bank in 2PL experiments with vanes compared to that in 2PT experiments with vanes indicates the lower volume of scour and the smaller width scour of the rectangle circumscribing the hole in the group of longitudinal piers compared to the group of transverse piers.



(a) (b)

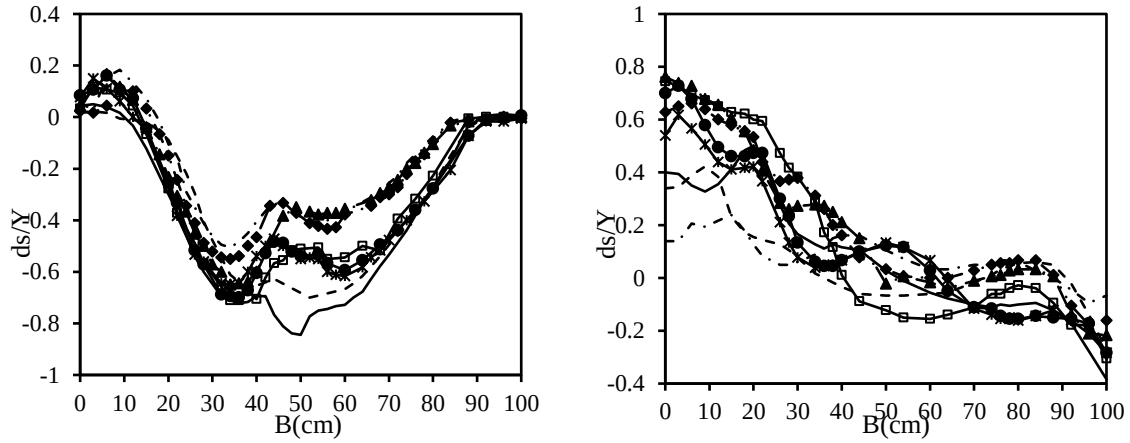
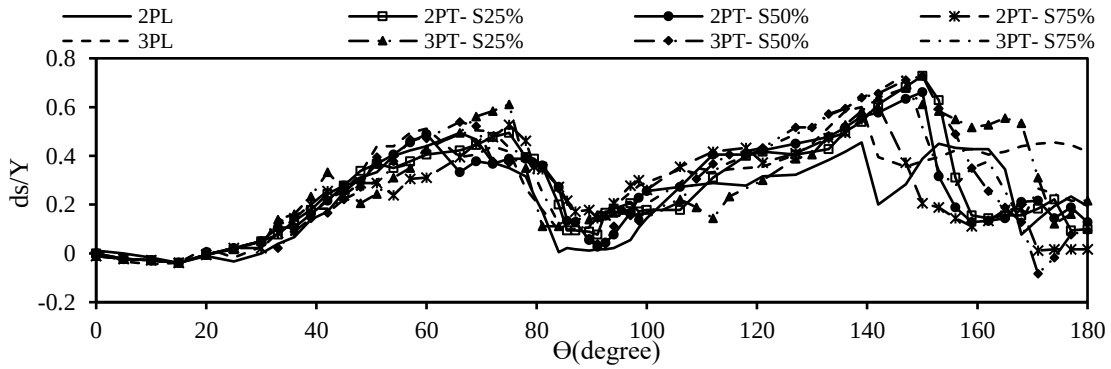


Figure 5. A sample of cross section at a distance equal to (a) 2.5 times the pier diameter towards upstream from the bridge piers location, (b) the center of the piers, (c) 2 times the pier diameter towards downstream from the bridge piers location, and (d) 42 times the pier diameter towards downstream from the bridge piers location in twin pier groups experiments with and without submerged vanes

Figure 6 examines bed alterations along the channel in experiments on longitudinal piers. As shown in the longitudinal profile near the inner bank in Fig. 6(a), the highest pile in the first half of the flume was approximately equal in both pier groups; however, in the second half of the flume, the highest sedimentation bar in 3PL experiment was approximately 1.3 times that in 2PL. As is observed in longitudinal profile variations in 2PL experiment, reduction in the height of the pile occurred at approximately 140 and 170-degree angles. With placement of the vanes in 2PL and 3PL experiments, the height of the pile at the inner bank along the channel increased in comparison with the piers with no vanes. By reducing the submergence ratio of the vanes, the sediment pile in the second half of the bend increased in twin pier group experiments with vanes, and decreased in triad pier group experiments with vanes. The maximum sediment pile was developed at a space of approximately 40D from the center of the flume in 3PL- S75%, 3PL- S50%, and 2PL- S25% experiments.



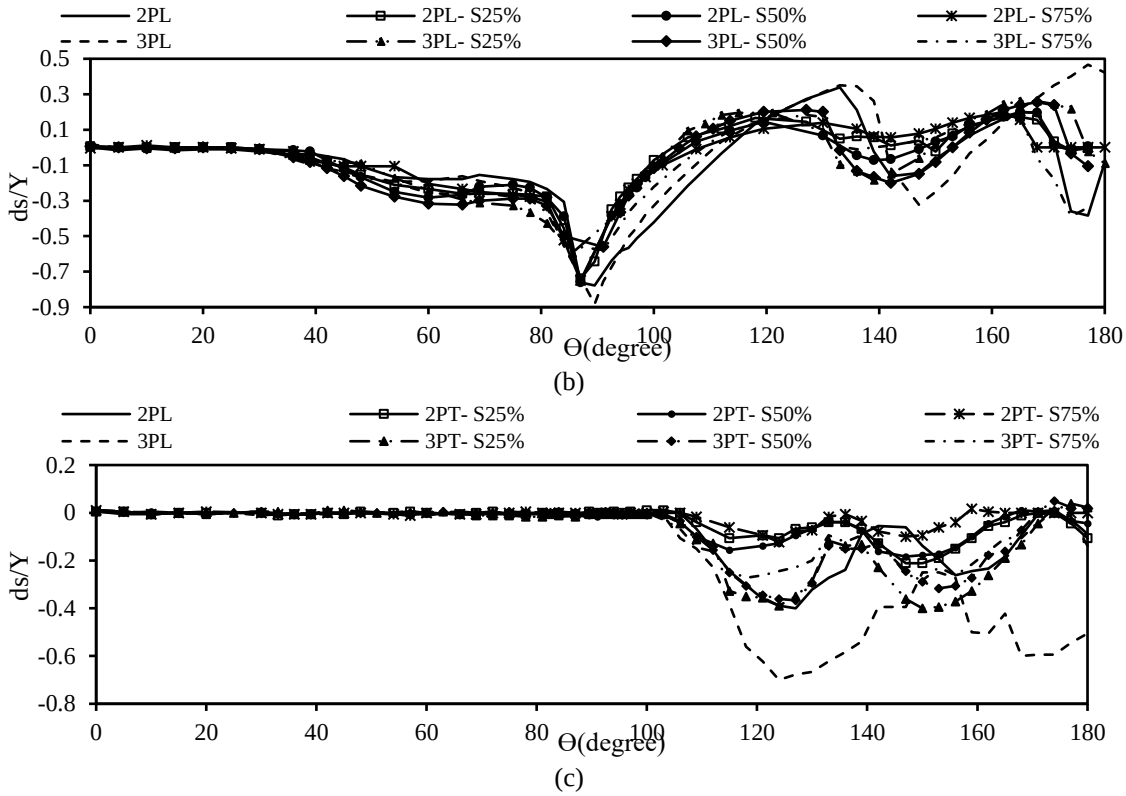


Figure 6. A sample of a longitudinal section at a distance equal to (a) 5, (b) 50, and (c) 95% of the channel width from the inner bank in experiments on longitudinal piers with and without submerged vanes

As is observed in Fig. 6(b), the longitudinal profile variations in mid-channel almost have the same pattern in both 2PL and 3PL experiments. Almost no alterations occurred in bed from the beginning of the bend to approximately 40-degree angle in every experiment. From approximately 40 to 80-degree angles, the bed underwent scour with a mild slope, the event which is due to down flow streams oriented towards bed. Then the scour slope increased at a distance of 80 to 90 degrees, which is due to local scour at the location of the vanes and the piers. After the 90-degree angle, sediment stemming from the vicinity of the piers and the vanes was developed at their downstream side and resulted in scour depth reduction. At a distance of about 30% of the end of the channel in experiments with vanes, two consecutive piles were developed in the same position with very little difference in height. By using the vanes in both pier groups, the height of the piles decreased in comparison with the piers without using vanes, and reductions in the height of the first pile in 2PL and 3PL tests were approximately 55 and 44% respectively compared to that in the test without any vanes. The second sediment pile in 3PL experiments with the presence of vanes decreased by approximately 50% in comparison with the piers without any vanes; however, in 2PL experiments, the pile height was the same whether with or without vanes. In this profile, reduction in deepest scour in both pier groups is approximately 29% in 3PL tests and 3.5% in 2PL in comparison with the piers-only tests. The second hole was formed at the downstream side, with its maximum depth occurring in 3PL experiments. As illustrated in Fig. 6(c), from the beginning of the channel to approximately 100-degree angle, no bed topography variations are observed. Thereafter, due to the flow turbulence

present after the pier, and due to orientation of the flow, the bed underwent scour. Sediments transported from the outer bank were led towards mid-channel by lateral flows. Increasing the number of piers from 2 to 3 increased scour at the outer bank. By using the vanes and increase in their submergence ratio, the scour decreased. Two scour holes were developed in both pier groups without upstream submerged vanes, where the deepest scour of the first hole in 3PL experiment was almost 1.75 times that in 2PL. With installation of the vanes, maximum depth at the outer bank decreased in both pier groups, where the ratio of deepest scour in triad pier groups to twin pier groups was approximately 4.3 times.

With the groups of piers installed in longitudinal direction and the protective role of the upstream pier, a different scour pattern happened in comparison to that in a single pier. A comparison was made between twin and triad longitudinal pier groups in order to examine the variations resulting from these pier groups and the effect of raising the number of bridge piers on topography of bed. To this end, an instance of the lateral profile is depicted in Fig. 7. The lateral profile in Fig. 7(a) at the upstream region of the front pier illustrates that the maximum scour depth in 3PL experiment is approximately 1.5 times that in 2PL. In 3PL experiments accompanied by vanes, the scour decreased throughout the cross section. Therefore, the scour at the inner bank barely changed in comparison to the piers with no submerged vanes applied, and that at 60% of B from the outer wall in 3PL- S75% decreased by averagely 45% compared to 3PL experiment. In 2PL experiments with vanes, the scour increased at an approximate distance between 30 and 50% of B from the inner wall, and decreased by about 20% at the outer bank in comparison with that in 2PL experiment. The sediment pile at 10% of B from the inner wall in 2PL experiments with vanes was approximately 2.5 times that in 2PL experiment. As shown in Fig. 7(b), by using the vanes in the pier groups tests, the bed did not change at 35% of B from the inner wall in comparison with the experiment without any vanes installed. According to this figure, the vanes have reduced scour at the outer bank in both pier groups by approximately 30% in comparison to the piers without using vanes. A review of bed topography alterations at the inner bank reveals that in twin pier group experiments, increasing the submergence ratio raised the sediment level in comparison with the piers with no vanes applied. In 3PL experiments, the vanes have not had any effect on changing the sedimentary height. In Fig. 7(c), with reduction of scour in the second half of the channel width, it might be deduced that the flow velocity in proximity of the outer bank has decreased. The scour depth decreases more in experiments with vanes in the twin pier groups than in the triad pier groups. The bed lateral profile is almost the same from mid-channel line to the outer bank for every submergence ratio in 2PL experiments accompanied by vanes. It may be observed in Fig. 7(d) that increasing the number of piers from 2 to 3 in the longitudinal pier groups, the distance of 70% of B from the outer wall has undergone scour. Installation of vanes revealed an acceptable performance in reducing scour in this area. In experiments containing vanes in both pier groups, a slope of bed profile variations increased, when the submergence ratio reduced. For example, 2PL- S25% has the highest pile in near the inner bank, and the deepest scour near the outer bank among the twin pier groups. By reducing the submergence ratio in both piers groups, the sedimentation height near the inner bank and the deepest scour of outer bank increased in comparison with the experiment without any vanes.

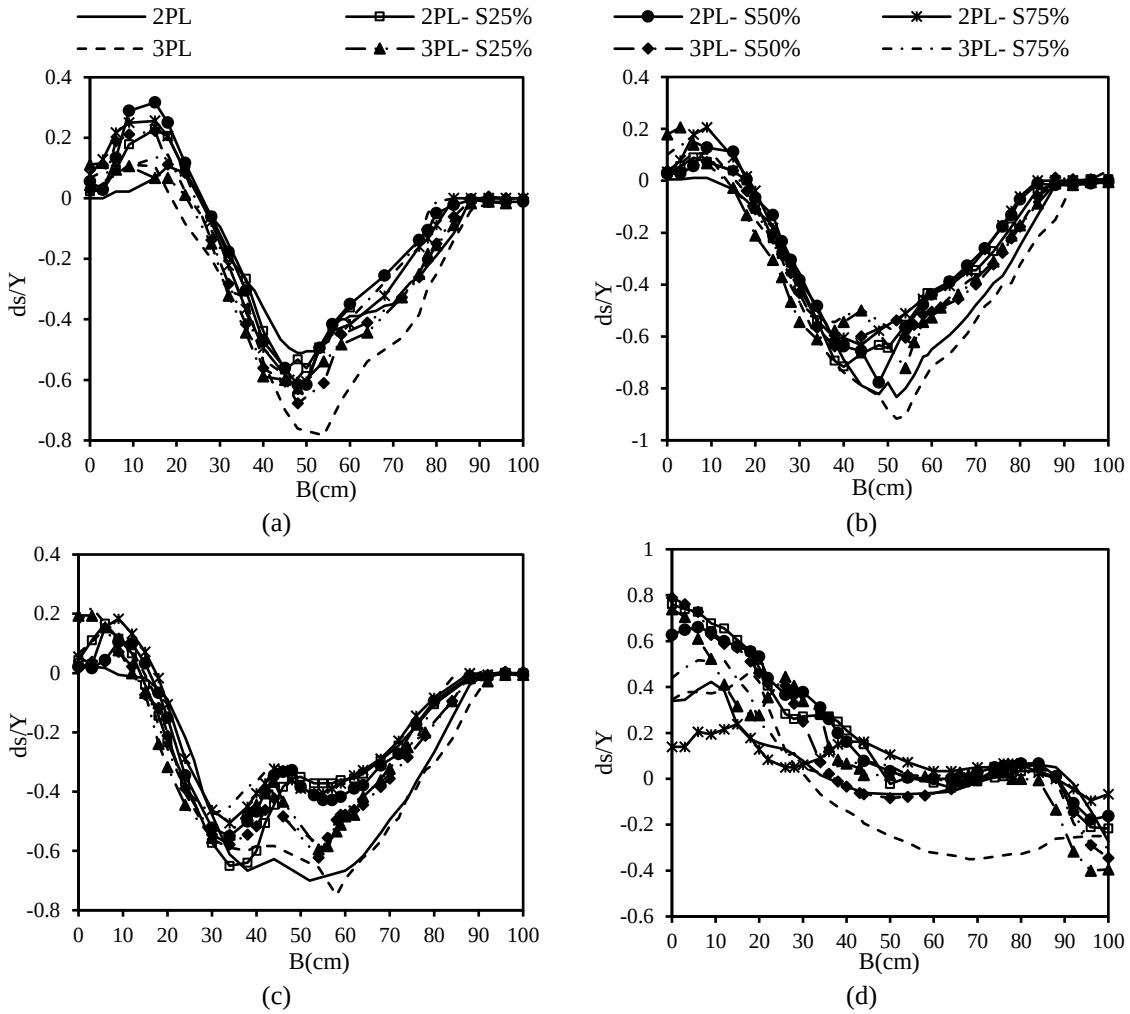


Figure 7. A sample of cross section at a distance equal to (a) 2.5 times the pier diameter towards upstream from the bridge piers location, (b) the center of the piers, (c) 2 times the pier diameter towards downstream from the bridge piers location, and (d) 42 times the pier diameter towards downstream from the bridge piers location in experiments on longitudinal piers with and without submerged vanes

Figure 8 provides an instance of longitudinal profiles in the transverse pier groups. According to Fig. 8(a), the height of sediment bar along the bend increased by using vanes in both pier groups. Increasing the number of piers heightened the sediment pile. In the second half of the flume, the highest pile was created in 3PT- S25% experiment at a space of approximately 48D from the center of the channel in downstream route with a height of around 1.2 times that in 3PT experiment. The height of pile in the second half of the flume was approximately 1.6 times that in the first half in tests with pier groups placed transverse to the flow.

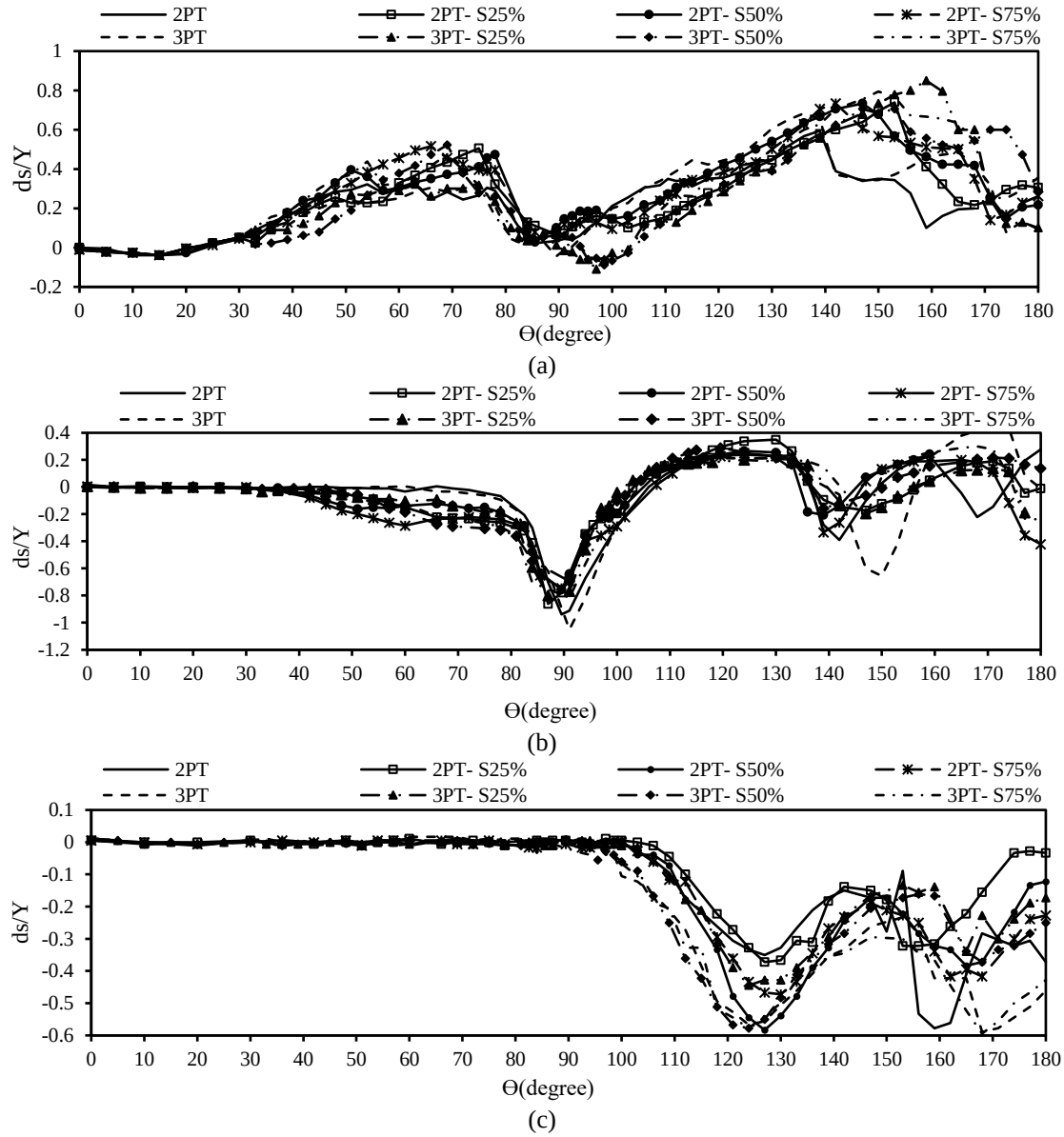
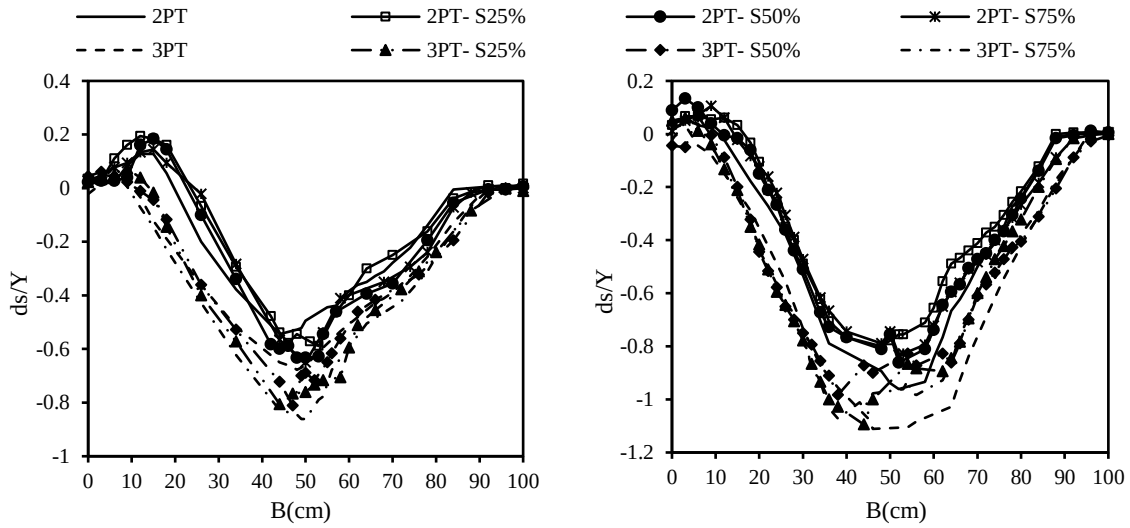


Figure 8. A sample of a longitudinal section at a distance equal to (a) 5, (b) 50, and (c) 95% of the channel width from the inner bank in experiments with pier groups transverse to the flow with and without submerged vanes

Figure 8(b) depicts the longitudinal profile in mid-channel. In 2PT and 3PT experiments, bed alterations from the beginning of the channel up to approximately 80-degree angle (equal to 55D from the beginning of the bend) were insignificant. The scour began almost from the 40-degree angle after installation of the vanes in these experiments. Increasing the number of piers from 2 to 3 in the transverse pier groups increased the highest scour in the vicinity of the piers by approximately 1.2 times. With submerged vanes utilized in twin transverse piers, the scour decreased compared to the piers with no submerged vanes installed when increasing the submergence ratio. Submerged vanes decreased the deepest scour by approximately 20% in 2PT,

and 33% in 3PT experiments in comparison to the piers without any vanes, the event observed in 2PT- S75% and 3PT- S50% respectively according to this figure. The second hole was formed at a space of approximately 30D from the center of the bend in downstream direction, where its maximum depth in 3PT was almost 1.7 times that in 2PT. Reduction in the second scour hole depth by vanes in comparison with the piers with no vanes was observed in 3PT experiment more prominently than in 2PT. In 2PT experiment accompanied by vanes, the second scour hole decreased with the submergence ratio of the vanes reduced in comparison to 2PT experiment, and the second scour reduction was about 55% in 2PT- S25%. The second hole depth in every 3PT experiment with vanes was reduced by averagely 70% in comparison with the test with no vanes applied. In this profile, the maximum height of the pile at the end of the bend was about 0.4Y, the fact observed in 3PT experiment. According to Fig. 8(c), with transverse placement of the piers to the flow, the bed at the outer bank underwent scour with a maximum depth of approximately 0.6Y. In every experiment, two consecutive scour holes were formed in almost the same positions near the outer bank. In 2PT experiments using vanes, the depth of the first hole was heightened, where its maximum value in 2PT- S50% was approximately 1.7 times that in 2PT experiment. Submerged vanes reduced scour in 3PT experiments in the vicinity of the outer bank in comparison with the piers with no vanes due to reduction of the submergence ratio. Therefore, bed topography alterations in 3PT- S75% and 3PT experiments were almost the same, and the outer bank scour in 3PT- S75% was deeper than that in 3PT- S25%.Figure 9 compares instances of a few lateral profiles at the pier groups transverse to the flow.



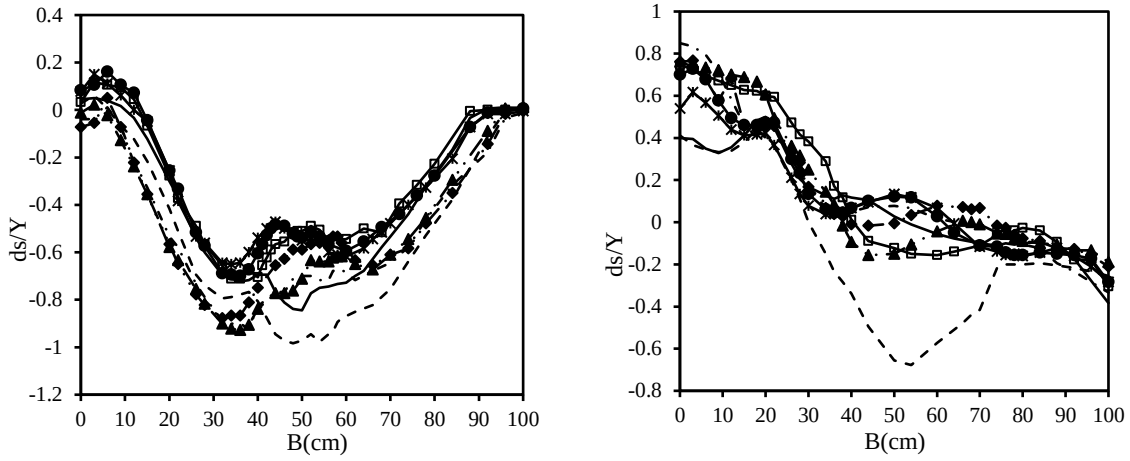
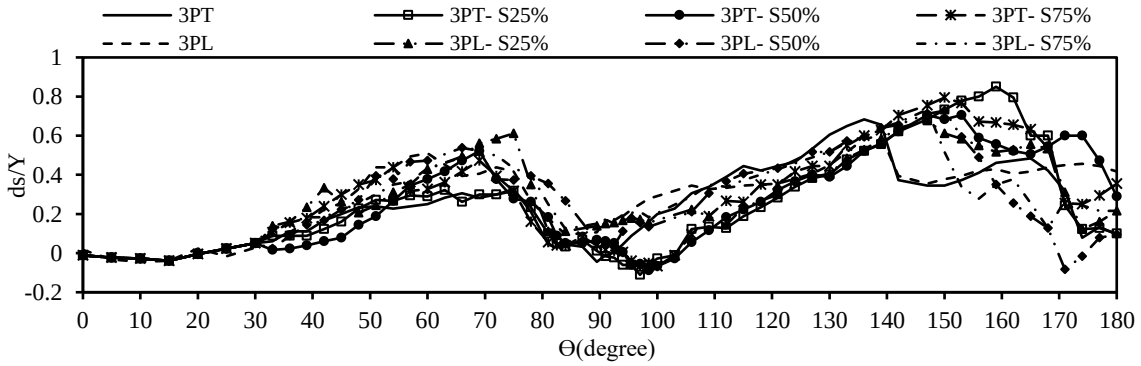


Figure 9. A sample of cross section at a distance equal to (a) 2.5 times the pier diameter towards upstream from the bridge piers location, (b) the center of the piers, (c) 2 times the pier diameter towards downstream from the bridge piers location, and (d) 42 times the pier diameter towards downstream from the bridge piers location in experiments with pier groups transverse to the flow with and without submerged vanes

As shown in Fig. 9(a), the scour depth at the location of the vanes increases at this section by averagely 32% in 3PT compared to 2PT experiment. This result was also 32% in 3PT experiments with vanes in comparison to 2PT experiments with vanes. With installation of vanes, the scour depth at this section was deeper than that in the case with no vanes installed. It may be concluded that the intervention of the vortices at the vanes with horseshoe vortices at the piers was intensified and led to sediment withdrawal from the upstream side of the piers. The bed topography alterations were the minimum in 2PT- S25% experiment in comparison to other experiments. As Fig. 9(b) illustrates, the scour depths in 3PT are averagely 1.5 times those in 2PT experiment. The scour hole slope at the inner bank was almost equal in 2PT and 3PT experiments accompanied by vanes. The submerged vanes in 3PT experiment reduced the scour about the groups of piers, and raised the scour at the inner bank. For instance, in 3PT- S50% experiment, the scour around the piers was reduced by averagely 20%, and that at the outer bank by averagely 15% in comparison with the piers with no vanes used. In 2PT experiment with vanes, the scour throughout the cross section decreased in comparison with the experiment with no vanes applied. 2PT- S50% and 2PT- S75% lateral profiles were almost the same at this section, and the scour profile in 2PT- S25% experiment was similar to those aforementioned experiments up to 50% of B from the inner wall. 2PT- S25% experiment presented an acceptable performance with 20% reduction in depth of scour at the second half of the channel width in comparison to other submergence ratios. In this pier group, the scour depths at the inner bank were almost equal for every submergence ratio. According to Fig. 9(c), bed topography alterations up to 40% of B from the inner wall are almost similar in both 2PT and piers experiments accompanied by submerged vanes. Then from this point to the proximity of the outer bank, installation of the vanes reduced scour in comparison with the piers with no vanes applied. In 2PT experiments containing vanes, the scour depths were decreased by averagely 35% in comparison to 2PT experiment. In 3PT tests, with application of submerged vanes, an increase occurred in scour depth up to 40% of B from the inner wall in comparison with the groups of piers with no vanes. Then the scour decreased after this point, where the highest

reduction happened in the middle of the flume width. For instance, 3PT- S50% experiment had the most influence with approximately 37% reduction in depth of scour around the pier groups in comparison with the piers without using vanes amongst all 3PT experiments. As shown in Fig. 9(d), the patterns of bed topography alterations in every experiment in either presence or absence of vanes in twin transverse pier groups are almost similar at this section, and the slope of these variations is approximately 0.11. By raising the number of bridge piers from 2 to 3, scour was created in mid-channel, where its maximum depth occurred at the center of the channel at an approximate value of 0.7 times the flow depth at the channel's entrance section. Application of the vanes reduced scour at cross section compared to tests of absent vanes, and a sediment pile was created up to almost 40% of B from the inner wall.

Figure 10 provides a comparison between three piers placed in two different directions to flow with submerged vanes in order to examine longitudinal profile variations. Figure 10(a) illustrates the longitudinal profile close to the inner bank. In this profile, the highest pile along the channel occurred in experiments with vanes. In a comparison between the piles in 3PT and 3PL experiments, two major differences were observed in profile variations in these pier groups. In the first half of the bend, the highest pile in 3PL experiment was about 1.5 times that in 3PT experiment. With progress of sediments towards the outlet of the bend, it could be observed that the amount of sediments accumulated near the inner bank was higher in 3PT experiment than in 3PL test. By using the submerged vanes in 3PT experiments, the sedimentation height was reduced by averagely 37% in comparison with the piers-only test from approximately the location of the piers to 32D in downstream direction. Thereafter, the height of the piles in piers with vanes increased in comparison to the pier groups without using vanes. In 3PT experiments accompanied by vanes, up to approximately 160-degree angle, the sedimentation height was ascending, and the maximum sediment pile occurred in 3PT- S25%. In 3PL experiments, in either presence or absence of vanes, the longitudinal profiles were almost the same up to approximately 140-degree angle. Thereafter, the maximum sediment pile occurred in experiments with vanes for every submergence ratio of vanes with a value equal to approximately 0.7Y. With transverse installation of the piers to the flow as well as the presence of vanes in experiments, the sediment pile increased in comparison to the pier groups with no submerged vanes so that the maximum pile in experiments accompanied by vanes for transverse piers was about 1.2 times that for longitudinal piers.



(a)

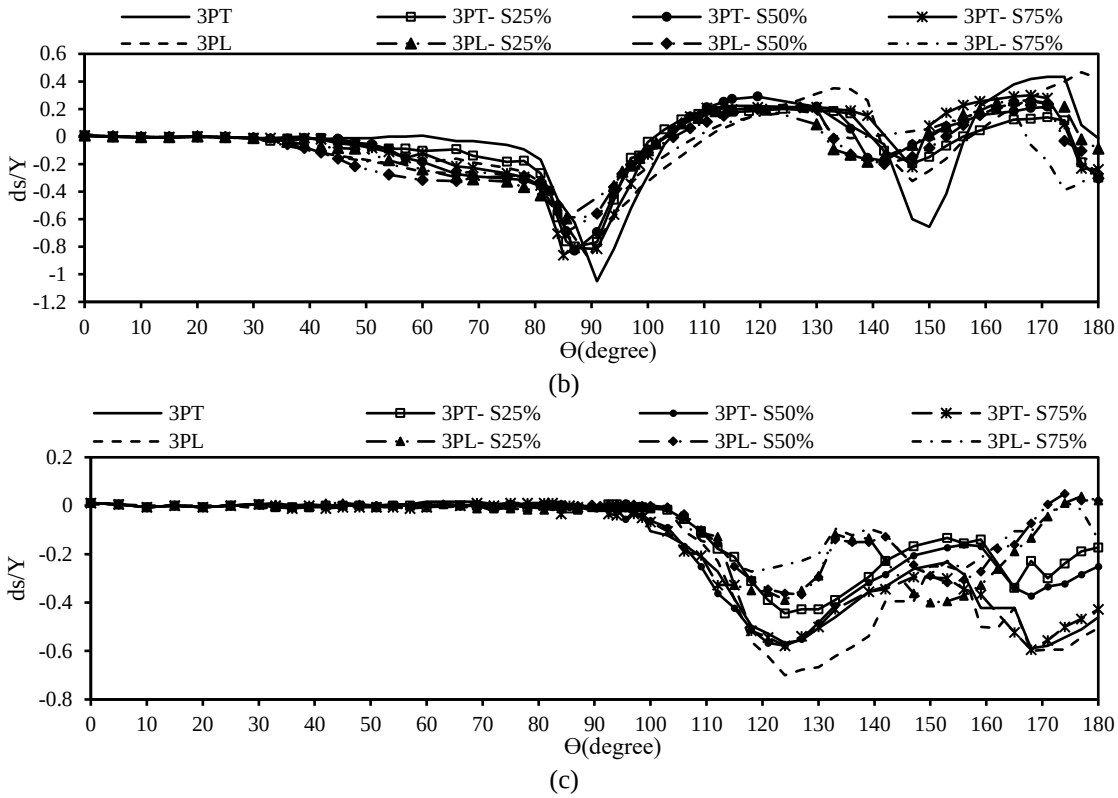


Figure 10. A sample of a longitudinal section at a distance equal to (a) 5, (b) 50, and (c) 95% of the channel width from the inner bank in triad pier groups experiments with and without submerged vanes

As shown in Fig. 10(b), with installation of the vanes in these pier groups, the deepest scour in 3PT tests reduced by averagely 22% and that in 3PL experiments by approximately 29% compared to the piers with no vanes used. When the triad piers were placed transverse to the flow, the scour hole slopes at the upstream and downstream regions of the piers in these experiments, as compared to each other, were almost equal, averagely 0.52 and 0.44 respectively. With longitudinal direction of the piers, the scour at the piers location decreased in proportion to that with transverse direction of the piers; however, its domain at the upstream region of the pier groups was extended to a distance of approximately 38D. The slope of scour around the piers in 3PL experiment extended at the downstream region of the piers with a slope of 0.25. The highest sediment pile at this section was created in 3PL and 3PT tests at a space of approximately 59D from the 90-degree position towards downstream. The second scour hole in 3PT and 3PL tests happened downstream at a distance of approximately 40D from the location of the piers. The deepest scour at transverse piers grew deeper by approximately 2 times that at longitudinal piers. By using vanes, the depth of the second scour hole declined by approximately 70% in 3PT experiments, and 50% in 3PL experiments for 50 and 25% submergence ratios in comparison to the pier groups with no vanes. In 3PL- S75% experiment, there was absolutely no trace of a second scour hole in mid-channel. According to Fig. 10(c), scour occurred at the outer bank at the downstream side of the piers in every experiment on triad pier groups. Two scour holes were observed in these experiments, and they occurred at almost the same point in 3PL and 3PT experiments. The deepest scouring of the first hole in 3PL was approximately 1.2 times

that in 3PT, and the depths of the second hole were almost equal in both pier groups. Topography alterations at the outer bank corresponded in 3PT and 3PT- S75% experiments, but in 3PT- S25%, scour depths decreased by averagely 40% compared to 3PT experiment. In 3PL experiments accompanied by submerged vanes, the depth of scour reduced in comparison to 3PL experiment due to the rise in the submergence ratio of the vanes. The minimum bed alterations happened in 3PL- S75% test with about 65% reduction of the deepest scour of the hole in comparison to the test of absent vanes.

Figure 11 illustrates instances of a few lateral profiles in tests on triad pier groups in longitudinal and transverse directions at specific intervals. As it can be noticed in Fig. 11(a), after placement of the vanes in 3PL experiments, the scour decreased throughout the cross section in comparison with the experiment of absent vanes. In 3PT experiments with vanes, the scour occurred only at the 20% distance in the middle of the cross section. 3PL- S75% and 3PT- S75% experiments respectively had the minimum and the maximum scours amongst all the experiments in this cross section. As shown in the lateral profile in Fig. 11(b), the effect of installing vanes was acceptable in both pier groups, and the scour decreased throughout the cross section. With presence of vanes in these experiments, reduction of scour at the outer bank in proportion to the opposite bank was evident. The maximum bed scour happened in 3PT, while the minimum happened in 3PL- S75%. Hence, the largest volume of scour holes took place in 3PT experiments. After changing the submergence ratio in both group of piers in tests with vanes, the scour pattern almost remained the same. The decrease in the deepest scour of 3PT- S50% to 3PT was approximately 18%, and that of 3PL- S75% to 3PL was around 23%. As depicted in Fig. 11(c), the maximum scour occurred up to 40% of B from the inner wall in 3PT tests accompanied by vanes. Thereafter, the scour decreased up to the proximity of the outer bank in 3PT experiments with vanes in comparison to the 3PT experiment. According to Fig. 11(c), the submerged vanes has an acceptable performance in reducing scour depth, with the most significant reduction behind the piers occurring in 3PT- S50% experiment. Close to the outer bank, approximately the last 30% of B, changing the submergence ratio caused no changes in bed profile in 3PT experiments; however, in 3PL experiments, the acceptable effect of vanes on scour reduction was observed in comparison with the pier groups with no vanes. For example, 3PL- S75% had the lowest bed topography alterations in both pier group experiments. According to Fig. 11(d), the scour depths increased by placing the piers transverse to the water flow, and the scour at this section was evident in 3PT experiment. This figure is also indicative of the fact that the submerged vanes reduce the scour depth, yet increase the sediment pile created at the inner bank.

Figure 12 depicts instances of the bed in the experiments. These images specify the location of sediment accumulation and scour around the piers. Given the fact that the bend used in the research was sharp, the inlet flow into the bend had a significant effect on bed topography, and made for generation of lateral flows inside the bend and creation of piles at the inner bank. With placement of the vanes in a clockwise angle, the flow was directed toward the inner wall, and resulted in scour after the location of piers and close to the inner bank, the fact which is also shown in Fig. 12(a). Sediments stemming from the scour hole formed around the piers were moved in downstream direction and toward the inner bank by lateral flows inside the bend and caused formation of a pile in this region. Figure 12(b) is illustrative of this fact.

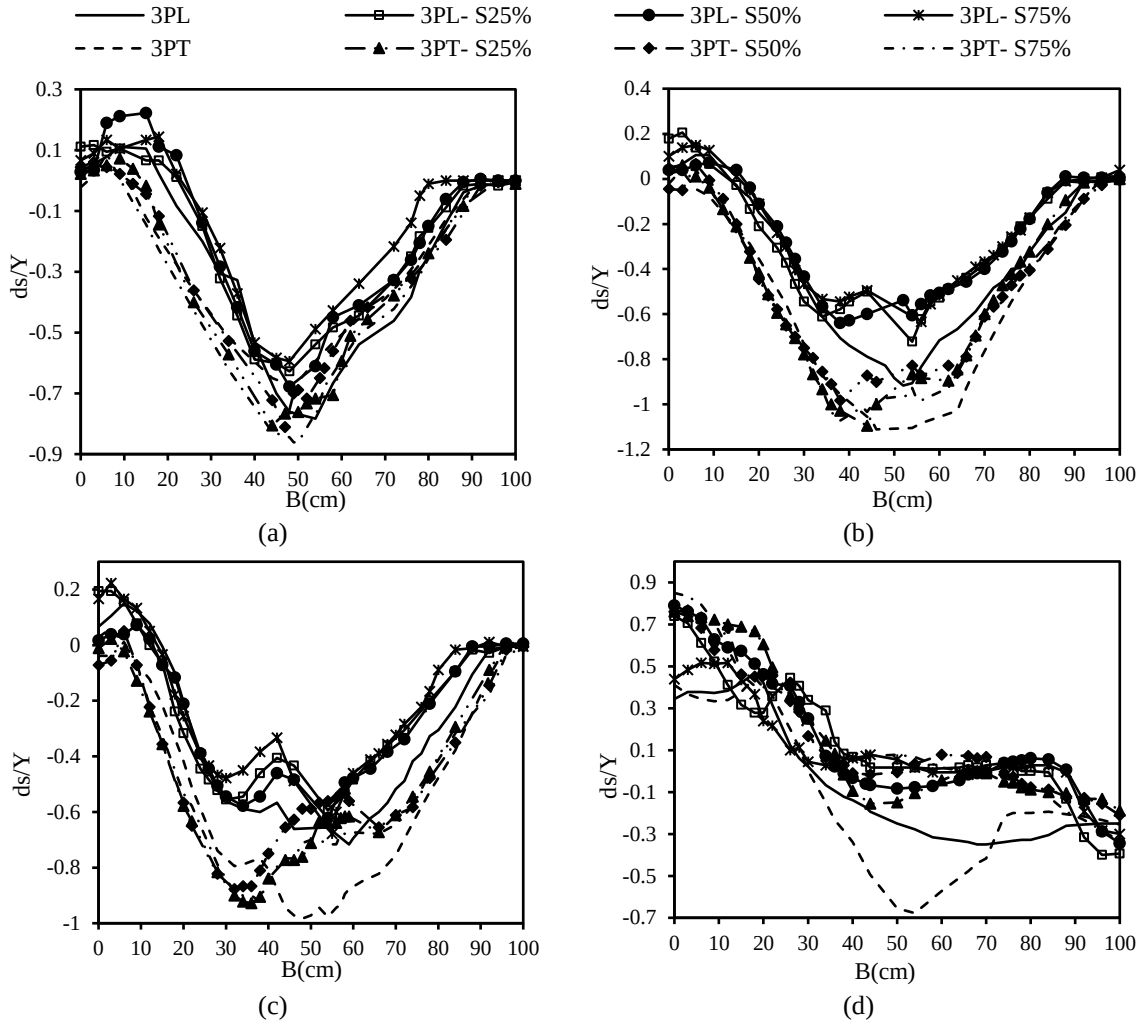


Figure 11. A sample of cross section at a distance equal to (a) 2.5 times the pier diameter towards upstream from the bridge piers location, (b) the center of the piers, (c) 2 times the pier diameter towards downstream from the bridge piers location, and (d) 42 times the pier diameter towards downstream from the bridge piers location in triad pier groups experiments with and without submerged vanes

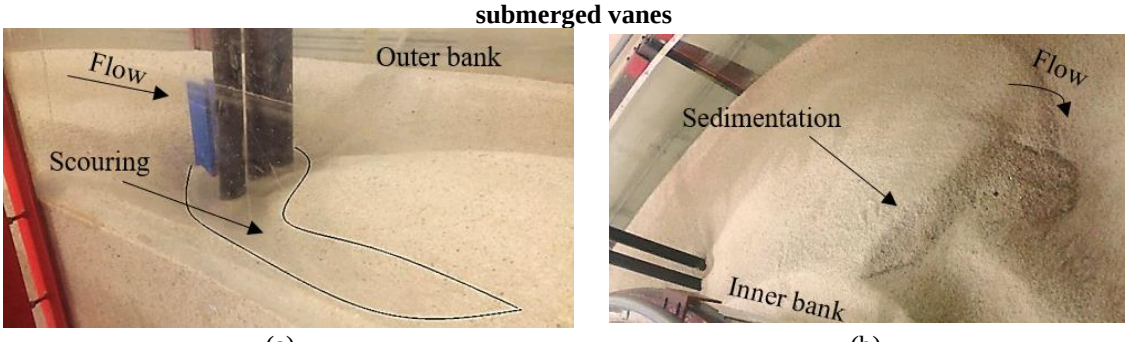


Figure 12. (a) An instance of the water flow redirected towards the inner bank, and the scour at this area in 3PT- S75%, and (b) an instance of sediments redirected towards the inner bank in 2PT

Figure 13 illustrates the scour hole slopes about the piers. In this figure, the slopes towards the inner bank, the outer bank, and the downstream side are denoted by m_i, m_o, and m_d respectively. Moreover, the upstream slope is denoted by m_u. It may be explained that m_u is a slope against m_d slope, calculated from the vicinity of the piers towards the upstream side of them.

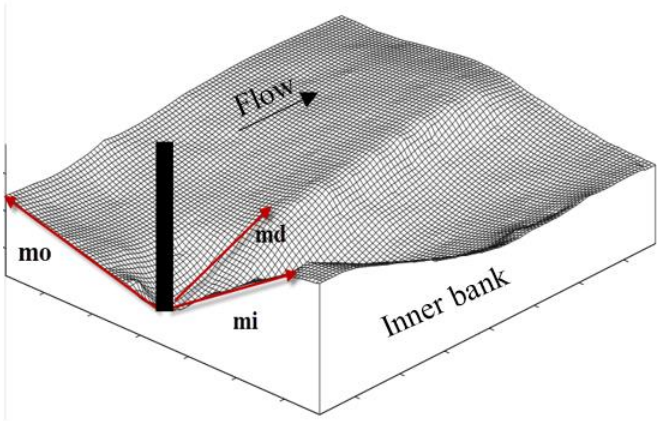


Figure 13. The scour hole slopes around the piers

Figure 14 is provided to examine the slopes of the generated scour.

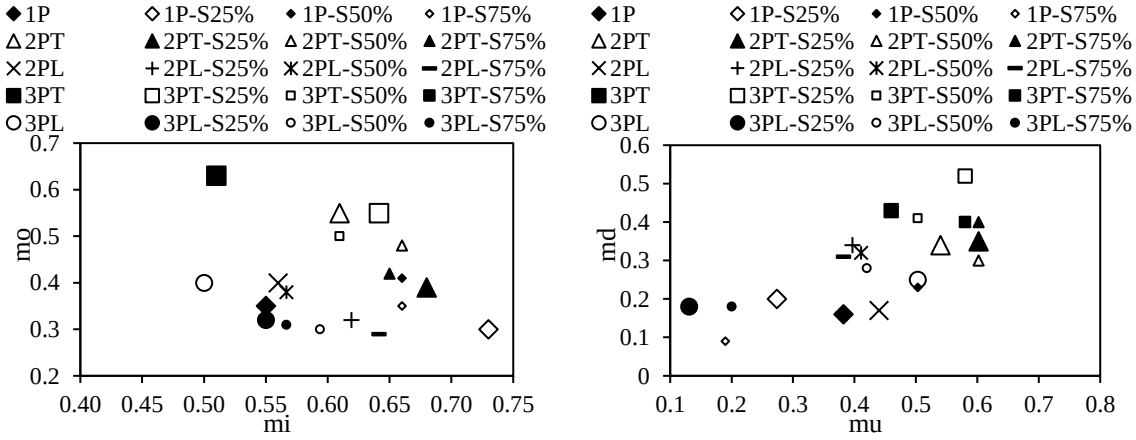
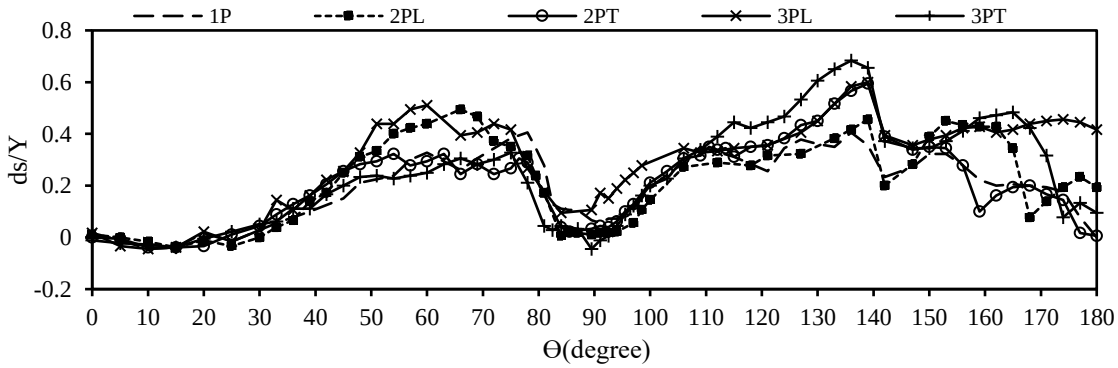


Figure 14. A comparison of scour hole slopes in the vicinity of the piers at (a) the cross section and (b) the longitudinal section of the channel

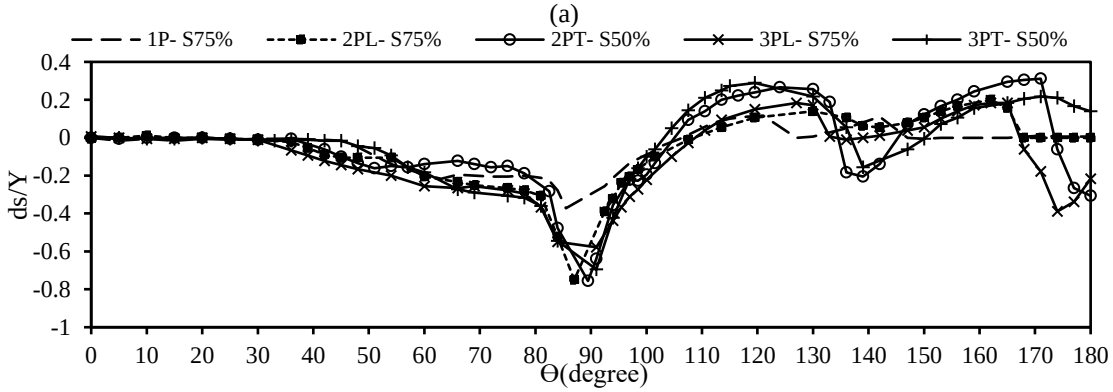
As shown in Fig. 14(a), the slope of scour at the inner bank (the mark) increases by using submerged vanes. The minimum slope of the inner bank, approximately 0.5, occurred in 3PT and 3PL experiments, and the maximum, approximately 0.73, occurred in 1P- S25%. The slope at the inner bank was approximately between 0.5 and 0.65 in most experiments. In other words, the inner bank underwent scour in an approximate horizontal angle of 26 to 33 degrees. The slope at the outer bank remained almost the same after changing the submergence ratio in 3PT and 3PL experiments using vanes. The slope at the outer bank was increased by reducing the submergence ratio in 2PT experiments using vanes. The minimum and the maximum scour hole slopes respectively happened in 2PL- S75% and 3PT. With transverse installation of the piers to

flow, slopes of the outer and inner banks increased in comparison with those of longitudinal installation of the piers to flow. The vanes in twin and triad groups of piers reduced the slope of the scour at the outer bank. According to Fig. 14(a), by using the two vanes in the piers, the scour slope at the inner bank was greater than that at the opposite bank. As Fig. 14(b) revealed by using the vanes in 2PL and 3PL experiments, the slope of the upstream hole decreased, while that in 2PT and 3PT experiments increased in comparison with the piers without using vanes. The maximum upstream slope among all the experiments occurred in 2PT- S25%, 2PT- S50% and 2PT- S75%. The slope downstream remained almost the same after changing the submergence ratio in 2PT experiments using vanes. In 1P experiments, the minimum slope downstream occurred for 75% submergence, and the maximum slope downstream in 3PT experiments occurred for 25% submergence. In Fig. 14(b), 1P- S75% experiment has the mildest slope upstream and downstream amongst all the experiments. In transverse and longitudinal twin and triad pier groups, the submerged vanes increased m_u and m_d slopes.

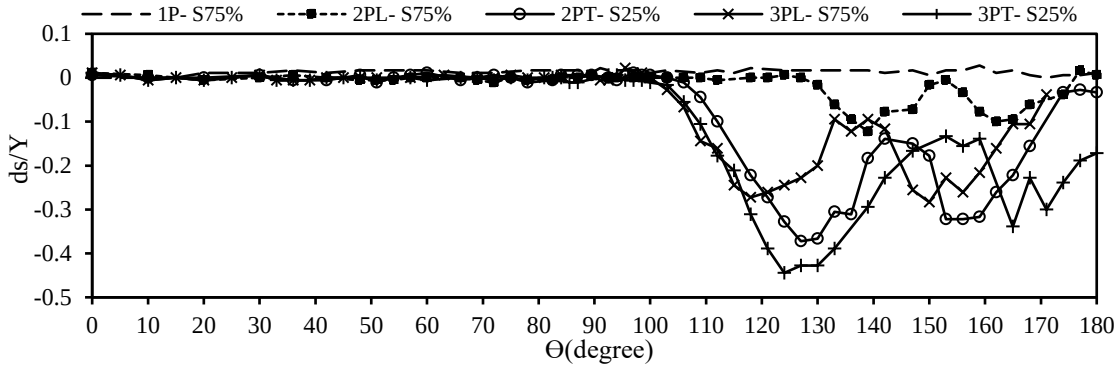
To evaluate the overall results of the lowest amount of bed scour in each group of piers, bed topography variations of the experiment in longitudinal and cross sections are shown in Figs. 15 and 16, and images of scouring around these experiments is depicted in Fig. 17 . Fig. 15 shows the smallest bed topography variation in each of the pier groups compared to other experiments in longitudinal sections. It can be seen in Fig. 15(a) that the smallest bed topography variations occurred at a space of 5% of B from the inner wall in each group of piers in tests without vanes. The lowest and highest sedimentary piles developed in these experiments occurred in respectively single pier and triad transverse pier groups.



(a)



(b)



(c)

Figure 15. The smallest bed topography variation at a distance equal to (a) 5, (b) 50, and (c) 95% of the channel width from the inner bank in each of the pier groups compared to other experiments in longitudinal sections.

Figure 15(b) indicates that in the longitudinal section of the central axis of the channel, the minimum scouring happened in experiments with piers accompanied by vanes. The smallest longitudinal changes also happened in the one pier test with 75% submerged vanes compared to other tests, which also included the lowest scour volume. It can also be observed in Fig. 15(c) that bed topography variations of the outer bank in the one pier test with 75% submerged vanes were almost negligible. Then, the least variation occurred in the longitudinal piers experiments with 75% submerged vanes and in the group of transverse piers experiments with 25% submerged vanes.

Figure 16 suggests the smallest variation in bed topography in each experiment in each of the pier groups at cross sections. Images of the lowest bed scour in these experiments are presented in Figure 18 as examples. According to Fig. 16(a), it is observed that at a space of 2.5D from the pier towards upstream, the minimum scour occurred in tests without vanes except in the group of triad longitudinal piers where placement of 75% submerged vanes declined scour depth. According to Fig. 16, the least variation occurred at the site of the pier and its downstream sections in the group of longitudinal piers and the single piers in experiments with 75% submerged vanes, while in the group of transverse piers, the optimum submergence percentage differed for each section. In Figs. 16 (b) and 16 (c), the scour width in the 3PT- S50% experiment was larger than that in the other experiments. According to Figs. 16 (b) and 17 (d), the deepest scour in this experiment happened around the pier placed close to the inner bank.

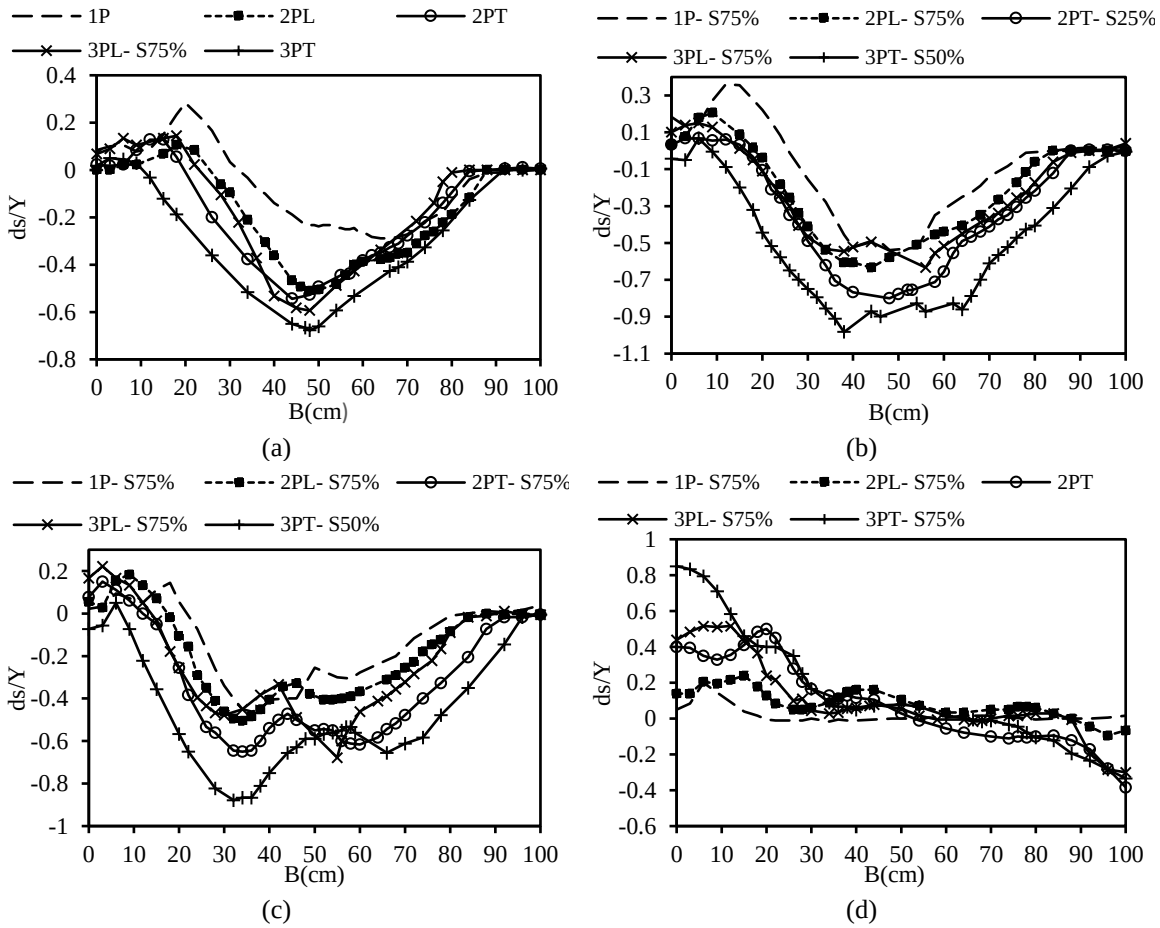
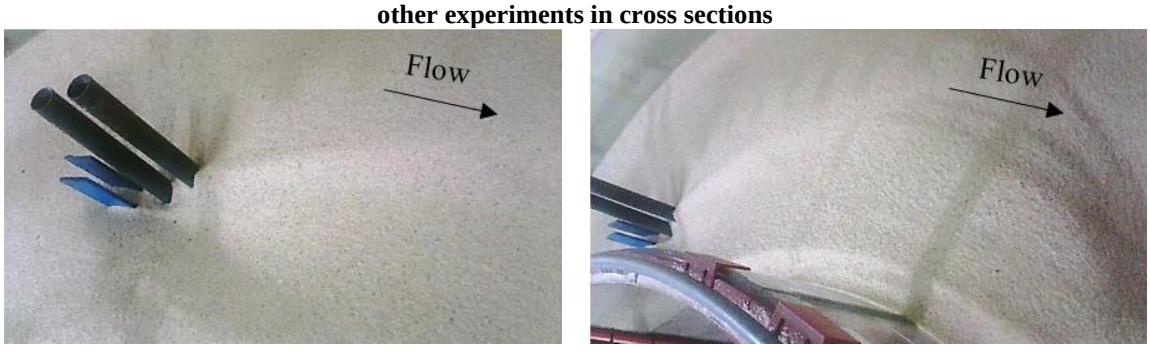


Figure 16. The smallest bed topography variation at a distance equal to (a) 2.5 times the pier diameter towards upstream from the bridge piers location, (b) the center of the piers, (c) 2 times the pier diameter towards downstream from the bridge piers location, and (d) 42 times the pier diameter towards downstream from the bridge piers location in each of the pier groups compared to other experiments in cross sections



(a)

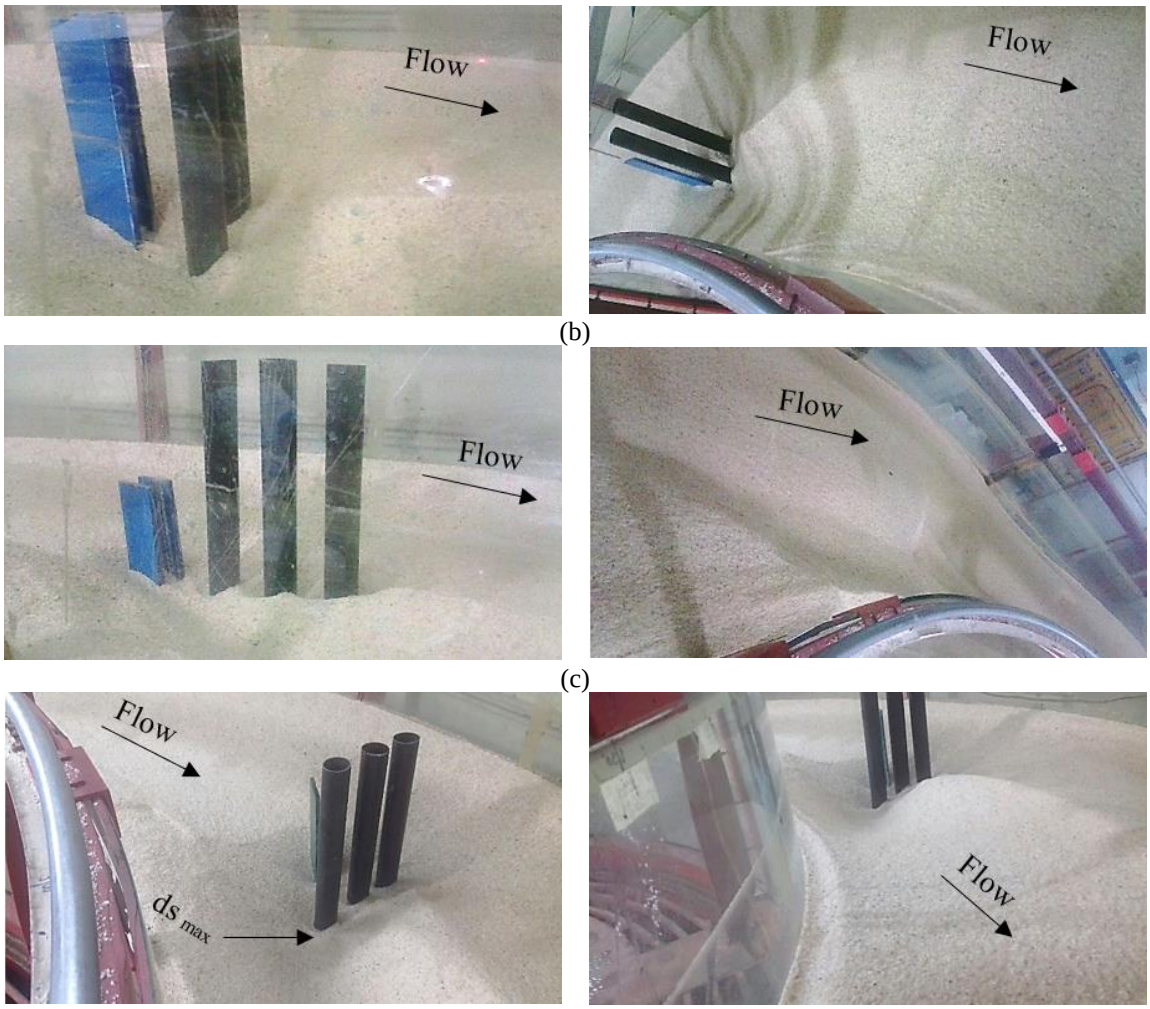


Figure 17. A sample of the smallest bed topography variation around the piers and along the downstream straight path in each of the pier groups compared to other experiments (a) 2PL- S75%, (b) 2PT- S25%, (c) 3PL- S75%, and (d) 3PT- S50%

4. Conclusion

The following results have been obtained from the effect of the use of submerged vanes with different submergence ratios on the bed topography around the pier groups.

In the one pier experiments with double vanes, the scour at the outer bank reduced by increasing the submergence ratio. In the one pier test accompanied by 75% vanes, the scour depths at the pier (the cross-sections at the angle of 90 degree) decreased by approximately 35% in comparison with the experiment of nonexistent submerged vanes.

In experiments of twin piers with vanes, reducing the submergence ratio increased the sedimentation height in proximity of the inner bank in comparison with the pier groups without using vanes, and it increased even more with placement of the piers as transverse to the water flow. The maximum height occurred in the transverse pier groups with vanes for every submergence ratio, and in the longitudinal pier groups with 25% submerged vanes, it was

observed with a height of approximately 0.7Y at a distance of around 35D from the center of the bend.

In longitudinal twin and triad pier groups, increasing the number of piers raised the scour at the outer bank in comparison to the test of absent vanes.

In transverse pier groups, the significant reduction of the deepest scour was observed to occur along mid-channel in the twin pier experiments with 75% submerged vanes, and in the triad pier experiment with 50% submerged vanes, by approximately 20 and 33% respectively.

After installation of the vanes, the slope of the scour hole at the inner bank grew sharper than that at the outer bank. The slope of the inner bank underwent scour with an approximate horizontal angle of 26-33 degrees.

In the single pier test with 75% submerged vanes, the upstream and downstream slopes decreased by around 50 and 43%, respectively, compared to the test without vanes. Vanes with 25% submergence ratio had the most significant effect on reducing the upstream slope by about 70% in the triad longitudinal piers compared to the piers without vanes.

References

1. Voisin A, Townsend RD, (2002). Model testing of submerged vanes in strongly curved narrow channel bends. Canadian journal of civil engineering, 29:37-49. DOI: 10.1139/L01-078
2. Tan SK, Yu G, Lim SY, Ong MC, (2005). Flow structure and sediment motion around submerged vanes in open channel. Journal of waterway, port, coastal, and ocean engineering, 131:132-136. DOI: 10.1061/~ASCE!0733-950X~2005!131:3~132!
3. Ghorbani B, Kells JA, (2008). Effect of submerged vanes on the scour occurring at a cylindrical pier. Journal of Hydraulic Research, 46:610-619. https://doi.org/10.3826/jhr.2008.3003
4. Bhuiyan F, Hey RD, Wormleaton PR, (2010). Bank-attached vanes for bank erosion control and restoration of river meanders. Journal of Hydraulic Engineering, 136:583-596. DOI: 10.1061/ASCEHY.1943-7900.0000217
5. Azizi R, Bejestan MS, Ghomeshi M, (2012). Scour depth at the edge of different submerged vanes shapes. Journal of Applied Sciences, 362-368. DOI: 10.3923/jas.2012.362.368
6. Barani GA, Shahrokhi Sardo M, (2013). Experimental Investigation of Submerged Vanes' Shape effect on river-bend stability. Journal of Hydraulic Structures, 1:37-43. https://jhs.scu.ac.ir/article_10073_7a8a7a653e4ee510cc5b8c12ead81158.pdf.
7. Azizi S, Farsadizadeh D, Arvanaghi H, Abbaspour A, (2016). Numerical Simulation of Flow Pattern around the Bridge Pier with Submerged Vanes. Journal of Hydraulic Structures, 2:46-61. DOI: 10.22055/jhs.2016.12856
8. Vaghefi M, Ghodsian M, Salimi S, (2016). Scour formation due to laterally inclined circular pier. Arabian Journal for Science and Engineering, 41:1311-1318. https://doi.org/10.1007/s13369-015-1920-6
9. Dey L, Barbhuiya AK, Biswas P, (2017). Experimental study on bank erosion and protection using submerged vane placed at an optimum angle in a 180 laboratory channel bend. Geomorphology, 283:32-40. DOI: 10.1016/j.geomorph.2017.01.022
10. Maatooq JS, Adhab BA, (2017). Effect of Distance of the Submerged Vanes from the Outer Bank on Sediment Movement within 180 Bend. American Journal of Engineering and Applied Sience, 10:679-684. DOI: 10.3844/ajeassp.2017.679.684

11. Shabanlou S, Azimi H, Ebtehaj I, Bonakdari H, (2018). Determining the scour dimensions around submerged vanes in a 180 bend with the gene expression programming technique. Journal of Marine Science and Application, 17:233-240. https://doi.org/10.1007/s11804-018-0025-5
12. Vaghefi M, Motlagh MJTN, Hashemi SS, Moradi S, (2018). Experimental study of bed topography variations due to placement of a triad series of vertical piers at different positions in a 180 bend. Arabian Journal of Geosciences, 11:1-13. https://doi.org/10.1007/s12517-018-3443-4
13. Biswas P, Barbhuiya AK, (2019). Effect of submerged vane on three dimensional flow dynamics and bed morphology in river bend. River research and applications, 35: 301-312. https://doi.org/10.1002/rra.3402
14. Zarei E, Vaghefi M, Hashemi SS, (2019). Bed topography variations in bend by simultaneous installation of submerged vanes and single bridge pier. Arabian Journal of Geosciences, 12:1-10. https://doi.org/10.1007/s12517-019-4342-z
15. Bejestan MS, Yabbarehpour E, Kashefipour SM, (2021). Enhancing transverse mixing by using triangular vane in the straight channel. Ain Shams Engineering Journal. 12:1385-1397. https://doi.org/10.1016/j.asej.2020.08.032
16. Safaripour N, Vaghefi M, Mahmoudi A, (2022). Experimental study of the effect of submergence ratio of double submerged vanes on topography alterations and temporal evaluation of the maximum scour in a 180-degree bend with a bridge pier group. International Journal of River Basin Management, 20:427-441. https://doi.org/10.1080/15715124.2020.1837144
17. Chooplou CA, Vaghefi M, Akbari M, (2023). Effect of repositioned submerged vanes on local scour variations around a pier in a bend: experimental investigation. International Journal of Environmental Science and Technology, 20:8627-8640. https://doi.org/10.1007/s13762-023-05031-3
18. Keshavarz A, Vaghefi M, Ahmadi G, (2024). Collars for Scour Reduction Around Different Shapes of Bridge Piers in a 180° Sharp Bend. International Journal of Civil Engineering, 1-19. https://doi.org/10.1007/s40999-024-00994-x
19. Vaghefi M, Zarei E, Ahmadi G, Behroozi AM, (2023). Experimental analysis of submerged vanes' configuration for mitigating local scour at piers in a sharp bend: Influence of quantity, length, and orientation. Ocean Engineering, 289:116267. https://doi.org/10.1016/j.oceaneng.2023.116267
20. Hamidi M, Sadeqlu M, Khalili AM, (2024). Investigating the design and arrangement of dual submerged vanes as mitigation countermeasure of bridge pier scour depth using a numerical approach. Ocean Engineering, 299:117270. https://doi.org/10.1016/j.oceaneng.2024.117270
21. Safaripour N, Vaghefi M, Mahmoudi A, (2024). An experimental comparison of 3D velocity components around single and twin piers installed in a sharp bend under the influence of upstream implemented vanes. Applied Water Science, 14:1-24. https://doi.org/10.1007/s13201-024-02177-4

22. Raudkivi AJ, Ettema R, (1983). Clear-water scour at cylindrical piers. Journal of Hydraulic Engineering, 109:338-350. https://doi.org/10.1061/(ASCE)0733-9429(1983)109:3(33
23. Chiew YM, Melville BW, (1987). Local scour around bridge piers. Journal of Hydraulic Research, 25: 15-26. https://doi.org/10.1080/00221688709499285

© 2024 by the authors. Licensee SCU, Ahvaz, Iran. This article is an open access article distributed under the terms and conditions of the Creative Commons Attribution 4.0 International (CC BY 4.0 license) (http://creativecommons.org/licenses/by/4.0/).

Journal of Hydraulic Structures

Volume 10 – Issue 3 – July 2024

Contents:

01 Investigating the effect of buried walls through rockfill detention structures on the longitudinal water surface profile

Jafar Chabokpour; Omar Minaei

18 Experimental study of contaminant mixing through the buried river junctions

Jafar Chabokpour

34 Feasibility study of fuzzy method in slope stability analysis of earth dams with respect to the uncertainty of geotechnical parameters

Amin Falamaki; Amir Hossein Shafiee; Mahdiye Esfandiyari

51 Application of machine learning methods on investigation the effect of interrupted deflector's height and downstream depth changes on energy dissipation at flip bucket spillways

Arash Adib; Danial Ebrahimzadeh; Mahmood S. Bejestan; Morteza Lotfirad; Masoud Oulapour

72 Hydraulic performance evaluation of head works using FLOW 3D

Mukesh Raj Kafle

90 The influence of the submergence ratio of submerged vanes on the slope of the hole around the pier groups in a sharp bend

Neda Safaripour; Mohammad vaghefi; Amin Mahmoudi

Shahid Chamran University of Ahvaz